Universität für Bodenkultur Wien
University of Natural Resources and Life Sciences, Vienna

Department für Biotechnologie
Department of Biotechnology

Head of Department:

Univ.Prof. Dipl.-Ing. Dr.rer.nat Reingard Grabherr

Raman Microspectroscopy and Biolayer Interferometry as novel tools to characterise cellular stages

Masterarbeit

zur Erlangung des akademischen Grades

Diplom- Ingenieur

an der Universität für Bodenkultur Wien

Verfasst von **Magdalena Lang**, BSc.

Betreuer: Assoc. Prof. Dr. Johannes Grillari

Mitbetreuer: Dipl. -Ing. Dr. Markus Schosserer

Eidesstattliche Erklärung

Ich erkläre ehrenwörtlich, dass ich die vorliegende Arbeit selbständig und ohne fremde Hilfe verfasst habe, andere als die angegebenen Quellen nicht verwendet habe und die den benutzten Quellen wörtlich oder inhaltlich entnommenen Stellen als solche kenntlich gemacht habe.

Fels am Wagram, _____ _____

Unterschrift

Danksagung

An erster Stelle möchte ich meinem betreuenden Professor Johannes Grillari danken, der es mir überhaupt ermöglicht hat Teil dieser tollen Arbeitsgruppe zu sein. Sein außerordentliches Fachwissen sowie Erfahrungen in der Wissenschaft sind unglaublich beeindruckend und motivierend. Es war eine äußerst lehrreiche und spannende Zeit, die ich nicht missen möchte.

Markus möchte ich ein riesengroßes Dankeschön für die wahnsinnig tolle Betreuung meiner Arbeit aussprechen!

Seine Freude an Forschung und Lehre sowie seine Motivation und Begeisterung für die Wissenschaft sind ansteckend. Seine Expertise und Kompetenz in so vielen Bereichen sind unglaublich. Er hat sich immer Zeit für Fragen oder etwaige Unklarheiten genommen und schafft auch unter Stress positiv und gut gelaunt zu sein. Beeindruckend fand ich die Ruhe und Strukturiertheit, mit der er einerseits an neue Projekte herangeht, andererseits mit auch nicht funktionierenden Experimenten oder unerwarteten Ergebnissen umgeht. Nach einem Gespräch mit Markus ist die vermeintliche Katastrophe nur mehr halb so schlimm. ☺

Bedanken möchte ich mich natürlich auch bei Jakob für die gemeinsame Zeit. Mit viel Fachwissen und guten Ratschlägen ist er mir zur Seite gestanden, und hat sich immer Zeit genommen um etwaige Unklarheiten aus dem Weg zu räumen.

Ein ganz spezielles Dankeschön gilt Lisa, die in allen Angelegenheiten für mich da war, auf deren Unterstützung und Hilfe ich vertrauen konnte und ohne die es sicher nicht so viel Spaß gemacht hätte. Danke für die schöne Zeit! ☺

Ich möchte auch ganz herzlich Vera, Elena, Regina, Teresa, Clemens, Fabian und Ingo Danke sagen, durch deren unglaubliche Hilfsbereitschaft in allen Bereichen ich mich willkommen und nie alleine oder verloren gefühlt habe.

Ein riesengroßes Dankeschön gilt natürlich auch meinen unglaublich tollen Eltern, die mir diese Ausbildung ermöglicht haben, den besten Schwestern Theresa und Pauline und meiner Liebe Thomas.

Ihr habt mich immer unterstützt, bei jeder Prüfung mitgefiebert und auch enormes Verständnis in all den Jahren gezeigt. Ich war und kann mir immer sicher sein, dass ihr hinter mir steht und für mich da seid.

Ihr seid die größten Stützen in meinem Leben und ich bin unglaublich froh und dankbar dafür. Ohne euch hätte ich es nie geschafft!

Summary

Ageing is an universal feature of all biological organisms and is somehow present in everybody's life. Due to the significant rise of human lifespan in the past years, ensuring a healthy and active long living society is increasingly important.

Senescence (lat. senescere = ageing) is defined as the phenomenon that cells stop dividing after reaching a certain population doubling, still being metabolically active.

In a young organism, cellular senescence prevents cancer at young age, but over life time it becomes a major contributor to ageing and paradoxically has negative influence on the development of diverse old-age diseases. This makes it all more important to guarantee identification and characterisation of these cells.

My master thesis is focused on the determination of senescent human dermal fibroblasts (HDF) using novel, non-invasive and label free methods. We confirmed senescence by currently known assays, which are disadvantageous as they are not entirely specific for senescence.

In order to discriminate between senescent and quiescent cells we established an assay using biolayer interferometry (BLI). We focused on setting up a measurement system for specific quantification of the small cytokine Interleukin-8 (IL-8; 8 kDa) in a non-invasive manner without any sample purification steps. Thereby, we discriminated quiescent from senescent samples by the difference in IL-8 secretion level in supernatants.

Another method, which is not just based on one specific target but provides information about the whole biological spectral fingerprint of a cell, is Raman Microspectroscopy.

By using this vibrational spectroscopic method, we got an inside into our samples on a molecular basis and detected differences between senescent and quiescent cells.

Additionally, we established a setup to detect cellular senescence via analysis of Raman spectra of supernatants based on differences in secretion using SERS (surface enhanced Raman spectroscopy).

In cooperation with the Medical University of Vienna we established a Raman setup for analysing several cell types treated with different anti-cancer drugs. We could successfully distinguish treated from non-treated cells and additionally tried to localise the treatment compound within the cell based on the unique Raman signature.

Kurzbeschreibung

Altern ist ein natürlicher Prozess der meisten Organismen und gegenwärtig im Leben eines jeden Menschen.
Durch die höhere Lebenserwartung der Menschen in den letzten Jahrzehnten, ist es immer wichtiger für eine gesunde und aktive Gesellschaft bis ins hohe Alter zu sorgen.
Seneszenz (lat. senescere = altern) beschreibt das Phänomen, dass Zellen nach einer bestimmten Anzahl an Zellteilungen nicht mehr wachsen, jedoch trotzdem metabolisch aktiv sind.
Es ist bekannt, dass uns diese im gesunden Zustand vor Krebs schützen, jedoch im Laufe des Lebens einen großen Beitrag zur Alterung leisten und, sich paradoxerweise auch bei der Entwicklung diverser Krankheiten negativ auswirken.
Umso wichtiges ist es, solche Zellen rasch und zuverlässig zu identifizieren und charakterisieren.
Ziel meiner Masterarbeit war es, Seneszenz in menschlichen Hautzellen, mittels Stress zu induzieren und diese mit nicht-invasiven Methoden rasch zu erkennen.
Wir bestätigten Seneszenz in Zellen mit bisher bekannten Methoden, welche jedoch nicht für eine spezifische Charakterisierung reichen.
Um solche gezielt von kontakt-inhibierten Zellen zu unterscheiden, nutzten wir Biolayer Interferometrie (BLI).
Wir konzentrierten uns darauf, einen Messaufbau zu etablieren, bei welchem wir garantieren können spezifisch das Zytokin Interleukin-8 (IL-8; 8 kDa) auf eine nicht invasive Weise und ohne aufwendige Probenvorbereitung zu messen.
Zweitens klassifizierten wir seneszente und kontakt-inhibierte Proben durch die Menge an IL-8 in Zellüberständen.
Eine weitere Methode, welche sich nicht auf ein spezielles Protein, jedoch auf über die gesamte spektrale Fingerprint Region Aufschluss gibt, ist Raman Mikrospektroskopie.
Durch diese Methode erlangten wir Informationen über unsere Proben auf molekularer Ebene und versuchten so, seneszente von kontakt-inhibierten Zellen zu unterscheiden.
Zusätzlich beschäftigten wir uns damit, eine Methode zu finden, bei welcher wir Überstände seneszenter Zellen mittels Raman Spektrum von Kontakt-inhibierten unterscheiden können (SERS = surface enhanced Raman spectroscopy).
Eine Kooperation mit der Medizinischen Universität Wien ermöglichte es uns, die Methode auch für eine andere wissenschaftliche Fragestellung zu nutzen. Verschiedene Zelltypen wurden mit Anti-Krebs Wirkstoffen behandelt. Wir konnten erfolgreich die behandelten von den unbehandelten biologischen Proben unterscheiden und versuchten weiterführend diese Substanzen in der Zelle aufgrund ihrer spezifischen Raman Signatur zu lokalisieren.

Table of content

1 | INTRODUCTION

1.1 Ageing and cellular senescence

The rise in life expectancy over the last decades led to an increased proportion of the elderly and reflects the significant medical-technological progress in terms of health care quality and the simplified access to medicine. However, this positive development implicates the higher incidence of age-related diseases, including cardiovascular illnesses, arthrosis or macular degeneration (López-Otín et al., 2013). These facts and the desire of a healthy and active aged society lead to the pursuit for a better understanding of the complex process of ageing and resulting diseases of it.
The majority of published studies focuses on effects on life span due to changes in nutrient-sensing pathways post dietary restriction, specific gene mutations or several other approaches in model organisms like the yeast *Saccharomyces cerevisiae*, the fruit fly *Drosophila melanogaster* or the nematode worm *Caenorhabditis elegans* (Kenyon, 2010).

It is already known that cellular senescence, defined as an irreversible cell cycle arrest, is one major contributor to age related diseases. In young organisms the senescence program is actually a defence mechanism to avoid malignant cell mutations, but an accumulation of senescent cells over life can have adverse effects on surrounding cells and environment. Also Kritsilis et al. (2018) and Toussaint et al. (2002) discussed the interesting contradictory phenomenon that those cells can inhibit tumour formation, but can also promote progression of neoplastic cells and tumours.
The reason thereof is that the efficiency of several programs and processes in our body, which are responsible for maintaining health at young age, decline with increased age and thus alter from being highly beneficial to a main cause of several detrimental and harmful effects (antagonistic pleiotropy) (Krtolica & Campisi, 2002).

Cellular senescence is an *in vivo* and *in vitro* appearing reaction to excessive stress, linked to cellular damage (Collado, Blasco, & Serrano, 2007; López-Otín et al., 2013). Several extrinsic and intrinsic factors during life can cause an accumulation of senescent cells, for example irradiation or chemotherapy (J. Coppé, P. Desprez, A. Krtolica, 2014) (Figure 1).

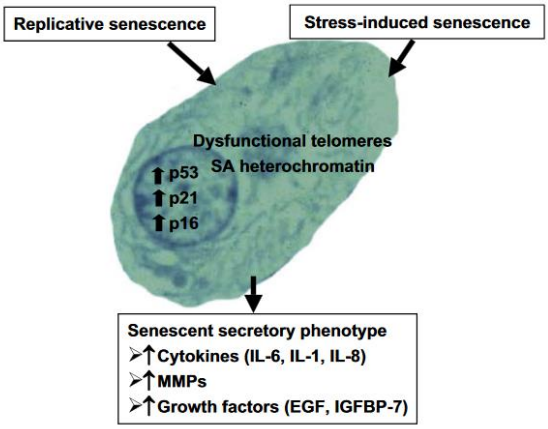

Figure 1 Illustration of the two categories of cellular senescence. Intrinsic factors, like telomere shortening cause replicative senescence while extrinsic signals lead to stress-induced senescence. The senescence associated secretory phenotype (SASP) is not only accompanied by telomere shortening and senescence associated heterochromatin, but is also characterised by increased cytokine levels and growth factors as well as metalloproteinases (MMP) (Loeser, 2009).

Cellular senescence was initially mentioned by Hayflick and Moorhead (1961) who observed an irreversible growth arrest state in human fibroblasts after a certain cultivation time. The finite number of doublings is caused by the continuous shortening of telomeres after each replication. As those are responsible for DNA stability and integrity, senescence prevents from potential malfunction or maldevelopments (Loeser, 2009).

Now it is known that cellular senescence is not only a consequence of telomere shortening (replicative senescence) but several different mechanisms, which operate as primary drivers like various kind of stress factors (stress-induced premature senescence; SIPS), oncogene-induced senescence (OIS), mitochondrial dysfunction or DNA damage (Kritsilis et al., 2018). So, briefly, cellular senescence is activated in response of various stresses.

Toussaint (2002) defined SIPS as the *'sustained effects of subcytotoxic stress on proliferative cell types, including irreversible growth arrest of (a majority of) the cell population'* (Toussaint et al., 2002). Scientists have concentrated on finding several characteristics for senescent cells in order to better understand the process of ageing on a molecular and biochemical level.

1.2 Markers of senescence

Typical senescent features were observed and published in different studies, above all the altered senescence associated secretory phenotype (SASP). After undergoing some metabolic changes, cells alter morphology and protein expression profiles. They also show modified secretion compared to normal proliferating or contact-inhibited cells, still being metabolically active (J. Coppé, P. Desprez, A. Krtolica, 2014).

The spindle shaped structure of a proliferating cell changes to an enlarged and flattened cell shape (Nishio, Inoue, Qiao, Kondo, & Mimura, 2001; Saretzki, 2009). Additionally, the metabolic changes lead to the expression of senescence associated β-galactosidase. This results in a higher amount of lysosomal mass and can be used as a biomarker (Rodier & Campisi, 2011). Lysosome biogenesis and apoptotic resistance are also indicators of senescence (Campisi & D'Adda Di Fagagna, 2007).

Furthermore, senescent cells activate tumour suppressor pRB (retinoblastoma protein), leading to characteristic structural changes of heterochromatin (senescence associated heterochromatin foci = SAHF). This results in a suppression of proliferation, but cannot be observed in all cell types (Rodier & Campisi, 2011).

Observations in aged tissues from mice and humans confirm also the correlation between increased tumour suppressor levels of $p16^{INK4a}$ under stress conditions and reduced proliferation (Liu et al., 2009). Significantly increased or reduced levels of several cytokines and growth factors are currently used as biomarkers for identification of senescent cells (Loeser, 2009).

Due to $p16^{INK4a}$ and p53-p21-RB regulation, senescent cells stay growth-arrested in G1-and G2/M-phase (Campisi & D'Adda Di Fagagna, 2007).

Furthermore, the pathways p53 and/or p16/RB play a major role as a reaction to DNA damage (Saretzki, 2009). Occurring DNA double-strand breaks are a typical feature of senescence and can be detected via λ-H2AX staining (Saretzki, 2009).Interestingly, a change in the p53 tumour suppressor gene, which mostly occurs when humans are affected by cancer, also seems to mediate cellular senescence. p53 inhibits cell proliferation in damaged cells and initiates apoptosis or senescence in order to avoid malignant transformations. However, *in vivo* studies confirm that an altered p53 function CDK (cyclin-dependent kinases) inhibitors like $p21^{Cip/Waf,}$ p^{ink4a} ,$p14^{Arf}$ are major contributors to ageing (Papazoglu & Mills, 2007).

Most cells, which undergo permanent DNA damage response (DDR), comprise DNA fragments consisting of chromatin modifications (DNA-SCARS = 'DNA segments with chromatin alterations reinforcing senescence').

However, senescence is not necessarily connected with DDR signalling (Rodier & Campisi, 2011). Hallmarks of cellular senescence are illustrated in Figure 2.

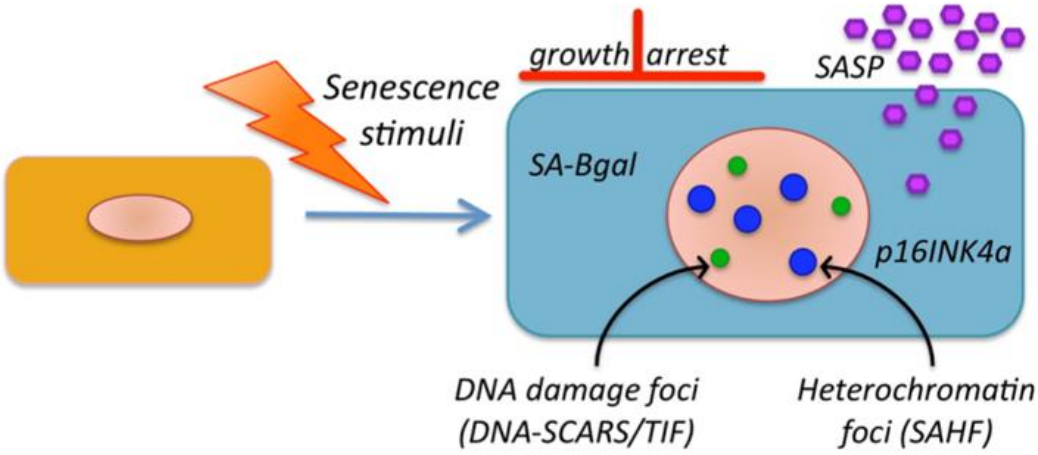

Figure 2 Illustration of the hallmarks of cellular senescence (Rodier & Campisi, 2011)

As an example, Loeser (2009) summarizes several observations regarding senescence features in chondrocytes mainly in aged tissue. As patients, who suffer from osteoarthritis (OA), show increased levels of previously named characteristics, it is suggested that senescent chondrocytes promote OA.
It is assumed that the loss of homeostasis is caused by increased levels of reactive oxygen species (ROS), which cause changes in the anabolic and catabolic activities and thus lead to severe negative effects.

To sum up, all these currently known and used markers have their drawbacks, as they are not specific for senescence state and not all cells exhibit every possible senescence marker. Additionally, some assays can just be performed *in vitro* and give inconclusive results (Liendl, Grillari, & Schosserer, 2019; Rodier & Campisi, 2011; Saretzki, 2009).

1.3 Induction of senescence in human dermal fibroblasts (HDF)

In the course of this work, primarily HDFs were used. These cells are described as the *'non-vascular, non-epithelial and non-inflammatory cells of the connective tissue'* (Kalluri & Zeisberg, 2006) and are enclosed in the extracellular matrix (ECM) of the connective tissue (Kalluri & Zeisberg, 2006).
The typical spindle shaped morphology is represented in Figure 3. Fibroblasts are heterogeneous and can be isolated from several parts of the human body depending on the scientific question. Expression of vimentin and fibroblast-specific protein 1 (FSP1) can be used as markers for fibroblasts (Fernandes, Russo, & Braga, 2014).
Additionally, HDFs are easy to culture and relatively simply available (biopsies). They play an essential role in terms of wound healing and scar-formation (Fernandes et al., 2014).
Importantly, fibroblasts are the '*best-studied cellular system of senescence'* (Roninson, 2003) and therefore highly suitable for our scientific questions.

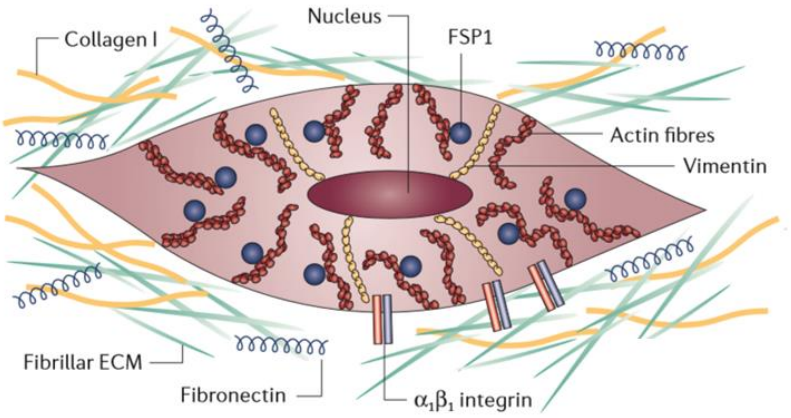

Figure 3 Illustration of a typical spindle-shaped fibroblast surrounded by ECM consisting of collagen I and fibronectin (Kalluri & Zeisberg, 2006).

Based on literature (Kozhukharova et al., 2018) we induced pre-mature senescence by treating the cells with doxorubicin according to a previously in-house developed protocol.

This anticancer drug belongs to the group of anthracyclines and is known for triggering oxidative stress. Using low concentrations, pre-mature senescence can be induced without causing apoptosis (Maejima, Adachi, Ito, Hirao, & Isobe, 2008).

Doxorubicin, commonly used for the treatment of malignant tumours, intercalates into DNA through initiation of DNA damage via topoisomerase II. It breaks double stranded DNA and subsequently inhibits biosynthesis. This results in a permanent cell cycle arrest and leads to apoptosis or senescence in a dose-dependent way (Gewirtz, 1999; Kozhukharova et al., 2018).

Roninson and co-authors (2002) confirmed the successful induction of senescence using doxorubicin and the resulting altered phenotype.

1.4 Biolayer Interferometry (BLI) to confirm senescence

Due to new advanced technologies, the possibilities for a fast quantification of therapeutic drugs or important biochemical interactions have increased in the last years.
The field of therapeutic and biomedical applications using new methods is expanding. Therefore, characterisation and specific knowledge about molecules and their behaviour are necessary.
Traditional technologies like enzyme linked immunosorbent assays (ELISA), gel electrophoresis and high performance liquid chromatography (HPLC) are time consuming due to many steps and long incubation times, comprise exhausting labour work and are not applicable for gaining high throughputs.
Thus, surface based methods like surface plasmon resonance (SPR) and BLI have been attracting more and more attention (Estep et al., 2013; Petersen, 2017).

SPR has an important role in drug development and enables multiplexing of several analytes in a short time (Abdiche, Lindquist, Pinkerton, Pons, & Rajpal, 2011). Although it is highly efficient and enables high throughput analysis, a large sample volume is necessary for appropriate outcomes (Estep et al., 2013). SPR machine and microfluidic device maintenance are also quite cost- and time-intensive (Petersen, 2017). Occurring mass-transport limitations and artefacts caused by surface heterogeneity can be overcome by using BLI. Previous studies confirm correlation of results between BLI and surface plasmon resonance (SPR) (Wartchow et al., 2011).
Referring to our objective, Yang and co-authors (2005) already reported the potential of detecting picomolar levels of IL-8 in human saliva using SPR. They established a convenient assay for analysis of saliva.
However, we tried a similar approach but using BLI as method of choice.

1.4.1 Fundamentals of BLI

BLI is based on the principle of measuring alterations in the interference pattern (Δλ) of white light between the optical reference layer and the layer, having the target of interest immobilised (Figure 4).
A spectrometer records all interferences across the whole spectrum of white light.
If proteins bind onto the biosensor, a resulting shift, due to changes in the interference pattern, is observed. All measurements can be monitored in real-time, the spectral shift is directly benchmarked by the change in thickness (nm) (Do et al., 2008; Gao, Zheng, & Wu, 2017).

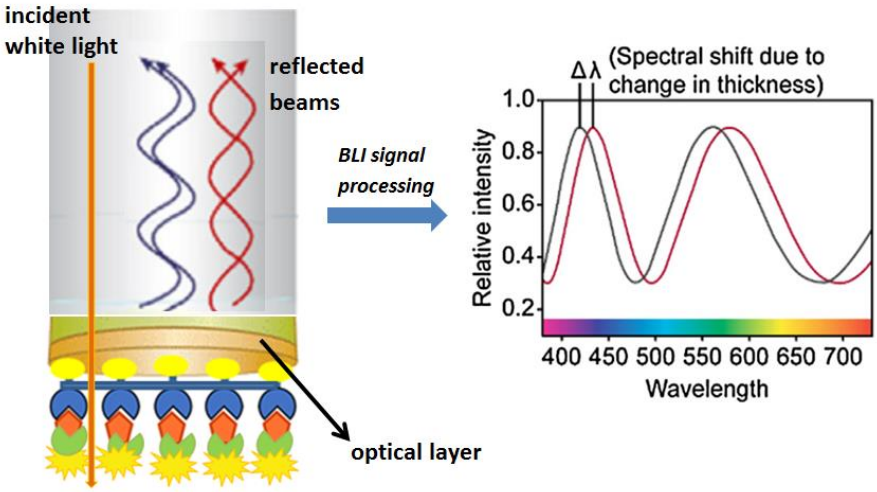

Figure 4 BLI scheme showing physical principle, adapted from Gao et al.(2017).

BLI has proven to be a successful tool for a broad range of applications like protein-protein or DNA-protein interactions (Sultana & Lee, 2015), capturing and quantifying specific biomarkers (Markwalter, Jang, Burton, Domingo, & Wright, 2017), antibody affinity measurements (Mader & Kunert, 2010), quantification of virus-like particles (Carvalho et al., 2017), protein-inhibitor kinetic confirmation (Arciniega & Torres-larios, 2019), protein-liposome interactions (Wallner, Lhota, Jeschek, Mader, & Vorauer-Uhl, 2013), fragment screening (Wartchow et al., 2011) as well as liposome interaction studies (Wallner, Lhota, Schosserer, & Vorauer-Uhl, 2017).
Also, compatibility of antibodies for an ELISA can be tested (Markwalter et al., 2017) and recent publications show outcomes regarding receptor binding complexes and their behaviour due to association (k_a) and dissociation (k_d) constants of cytokines using BLI (Bloch et al., 2018).
As biosensor-based measurements have the advantage of being time-saving, sensitive and robust, establishing an assay for a specific identification of senescent cells seems very promising.
While previously described assays for detection of senescent cells have several drawbacks, the approach of detecting IL-8 using antibodies is sensitive and overcomes labour-intensive purification or labelling procedure. Additionally, this technology avoids fluorescence or radioactive labelling.

Here, I describe BLI as a novel, non-invasive tool for quantification of IL-8 levels in HDF supernatants using Octet®. IL-8 is a human chemokine, which consists of 72 amino acids and has a molecular weight of about 8 kDa (Lin et al., 2004). Present only in low amounts in unstimulated cells, it can be

upregulated up to 100-fold when induced by tumour necrosis factor (TNF) or Interleukin-1 (Hoffmann, Dittrich-breiholz, Holtmann, & Kracht, 2002).
IL-8 is one of the typical SASP factors, playing a key role in inflammation (Scott et al., 2009). We aimed for distinguishing different cellular stages based on IL-8 levels in supernatants analysed with BLI.

1.5 Considerations of using Raman Microspectroscopy as novel marker for senescence

The potential of using Raman Microspetroscopy for chemical analysis has been known for several years.
However, using this method for biomedical research becomes more and more of interest and therefore increasingly important. Due to its capability of gaining insights into molecular structures and constituents of biological material, Raman Microspectroscopy has evolved to a powerful tool for diagnostics and indication of biochemical changes in cells or even tissues (Hanlon et al., 2000).
It enables variable methodologies for analysing samples in a label-free and non-invasive manner.
Very low sample volumes (micrograms to nanograms), time efficiency and easy sample preparation are advantages over previously used analytical methods.
Additionally it has to be mentioned that with other techniques like immunofluorescence (IF), a qualitative analysis is possible, but obtaining information regarding chemical composition is unfeasible (Mariani, Maccoux, Mattha, Diem, & Hengstler, 2010).
Also, drawbacks of IF like finding compatible antibodies or specific markers can be easily overcome and yet it is possible to gain information about biochemical composition and structural features on molecular level (Krafft, Knetschke, Siegner, Funk, & Salzer, 2003; Movasaghi, Rehman, & Rehman, 2007).
Some scientists see even great potential that this technique may revolutionize ‘omics’ analysis, such as genomics, transcriptomics, proteomics or metabolomics (Kopec, Imiela, & Abramczyk, 2019).
Combining several spectroscopic methods, like SERS and fluorescence microscopy, become quite popular and gained increase importance in the last years. Multimodal Imaging (MMI) techniques are highly interesting in the medical field in terms of cancer identification and cancer therapy (Henry, Sharma, Cardinal, Kurouski, & Van Duyne, 2016).
Another vibrational method, which is label-free and often used, is infrared (IR) spectroscopy.
Although it is also possible to identify organic compounds and molecules based on specific frequencies, Raman spectroscopy is less affected by differences in water content.
This property is especially advantageous in tissue diagnostics as here the protein content changes in dried tissue (Köhler, Machill, Salzer, & Krafft, 2009).

However, already in 1996 scientists reported the use of Raman Microscopy in cancer diagnosis, as they could successfully differentiate between malignant and normal cervical tissue. They stated that the high potential of this method has to be further investigated (Bohorfoush A.G., 1996). Progresses

regarding spectral acquisition and measurement sensitivity in the past years were of high importance. Nowadays, it is possible to acquire high quality spectra of cells and chromosomes (Krafft et al., 2003). There are several studies focusing on using Raman microscopy to answer biological issues like identification of cell death stages (Brauchle, Thude, Brucker, & Schenke-Layland, 2014), glycosylation patterns in breast cancer (Kopec et al., 2019), analysis of serum (González-Solís et al., 2014), localisation of cell compounds like nucleus, organelles and membrane (Krafft et al., 2003), cancer gene detection (Vo-Dinh, Allain, & Stokes, 2002), cortical bone alterations during life (Akkus, Polyakova-Akkus, Adar, & Schaffler, 2003) and many more. Also in tissue diagnosis, Raman mapping is a field of increased importance and progress. Already in 2003 scientists published that it is possible to gain information of axillary lymph nodes which contain breast cancer by using Raman (Smith et al., 2003).

Key compounds of high interest are proteins, lipids and carbohydrates (Kopec et al., 2019).

An overview of possible biological applications of Raman Microscopy is visualized in Figure 5.

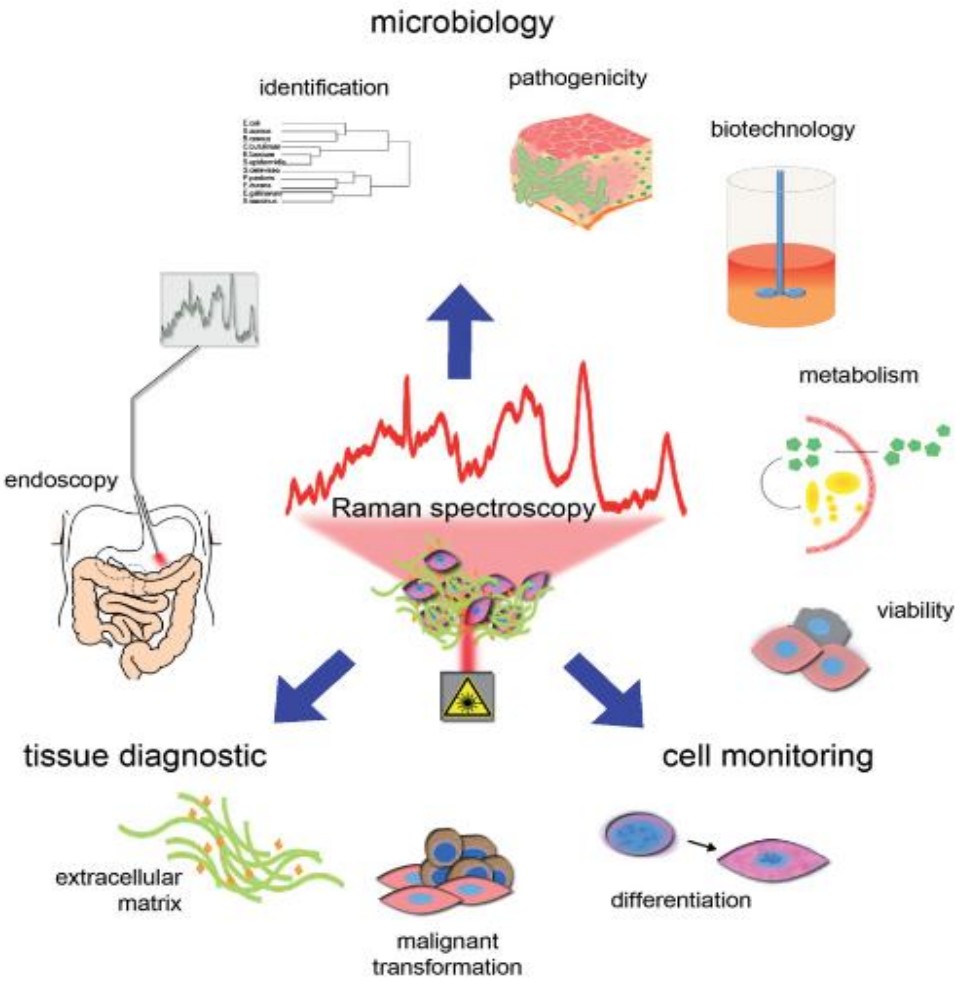

Figure 5 Illustration of the diverse field of Raman Microscopy applications in the biomedical field (Stock, 2013).

Although there is this broad range of applications, there are not yet many publications using Raman Microscopy for identification of cellular senescence.

Mariani and co-workers (2010) published that expression and secretion of tumour-inducing as well as tumour-repressing proteins of senescent cells lead to a different Raman signature compared to normal proliferating cells. Findings after measurement and evaluation confirm differences regarding lipid isomers and nuclear alterations in senescent cells.

Replicative senescence of mesenchymal stem cells (MSC) was investigated by Bai and co-workers (2015). They found that the ratios between different peaks alter, when cells reach the senescent state. Although several regions like 934 cm^{-1}, 980 cm^{-1} and 1097 cm^{-1} are increased in replicative senescent cells, this change was not found to be significant.

At 1157 cm^{-1} and 1521 cm^{-1}, a decrease in the relative intensities of senescent cells was observed, but was not sufficient to be used as a marker.

1.5.1 Fundamentals of Raman Microspectroscopy

The physical principle behind this spectroscopic technique was firstly mentioned by C.V. Raman (RAMAN & KRISHNAN, 1928) and is schematically illustrated in Figure 6.

When light (mainly from an excitation laser light source, which can range from UV to near-infrared (IR)) collides on a surface or substance it will mainly be scattered or absorbed having the same frequency.

Just a small part leads to vibration of molecules, meaning only every 10^6–10^8 photons are subjected to inelastic scattering. Changes in frequency are proportional to the light energy and are the same as the frequency of the transitional molecules. This interaction is called Raman, or inelastic scattering (Hanlon et al., 2000; Liendl et al., 2019; Mariani et al., 2010).

Now, this scattered light can be recorded via a spectrometer (Raman shift vs. scattered intensity). Importantly, a Raman shift is defined as the inverse of wavenumbers (cm^{-1}). The molecular vibrations are unique for each molecule and specific for distinct chemical bonds, functional groups or confirmations. This results in specific Raman shifts causing distinct peaks or even regions.

Important examples referring to our scientific questions are regions from 1220-300 cm^{-1} belonging to C-N and N-H bonding, or 1600-1800 cm^{-1} indicating C=O and C=C stretching, which correspond to lipids and proteins.

For instance, if a sample contains DNA, a distinct peak at 481 cm^{-1} will be apparent in the Raman spectrum.

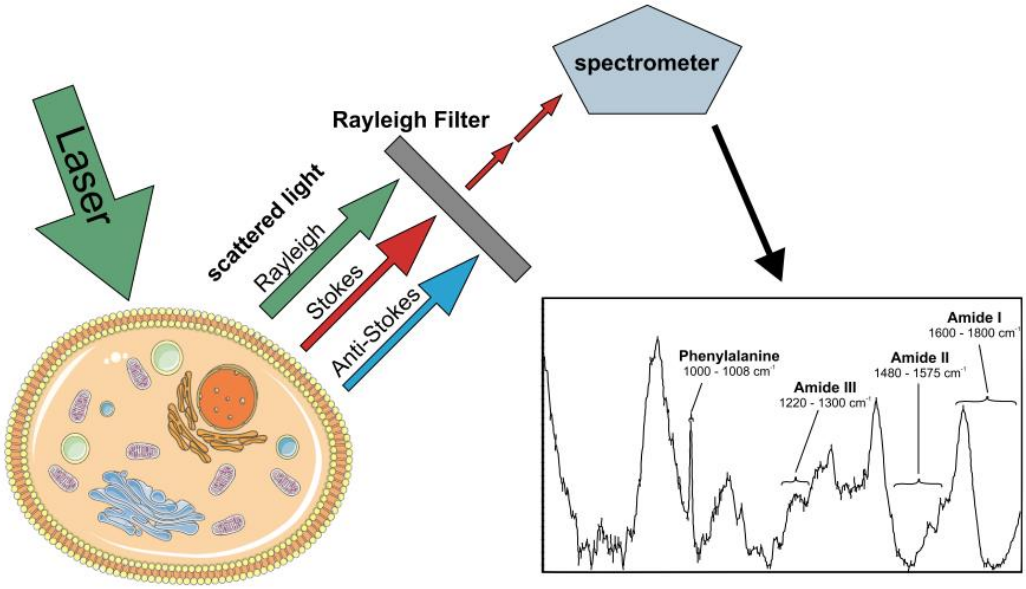

Figure 6 Schematic principle of Raman Microspectroscopy (Liendl et al., 2019).

1.6 Surface enhanced Raman spectroscopy

As most of the Raman peaks are quite narrow, a high resolution of Raman spectra is necessary. Due to the weak Raman scattering intensity, the sensitivity is decreased and thus limits the applications of this technique (Huang et al., 2016).

To overcome this challenge, surface enhanced Raman spectroscopy (SERS) is a great opportunity relying on the amplification of Raman scattering (Figure 7). In particular, the increase in signal up to several orders of magnitude (up to 10^6-fold enhancement) is reached due to the addition of gold or silver surfaces. This phenomenon was already published in 1974 (Fleischmann, 1974; Stiles et al. 2008).

SERS is based on the chemical (CE) and the electromagnetic enhancement (EM). Reciprocal effects of light-metal as well as light-molecule are the main cause for the increase in signal. Energy (from the laser light source) encounters on a metal surface and leads to oscillation. Energy of incident light correlates with the anyway occurring oscillation frequency and results in surface plasmon resonance (SPR). Laser excitation wavelengths of 633 nm as well as 785 nm give good results and enhance signal substantial.

Nanoscale constructs made of Ag, Au or Cu enable a localisation of SPR (LSPR) (Zong et al., 2018) . Also, shape, size, electron mass and density seem to play major roles. Although silver particles lead to a higher signal increase, gold has the advantage of being inert and is therefore very beneficial for *in vitro* as well as *in vivo* analysis.

However, incident light is concentrated on the nanoparticles resulting in a huge amplification (2 up to 5 dimensions) of the original signal (Jamieson et al., 2017; Zong et al., 2018).

Interestingly, this effect is just observed in presence of concentrated nanoparticles (aggregates), while single nanoparticles just marginally increase the signal (Bonifacio et al., 2014).

Besides nanoparticles, which require a rough surface, also ‘tips’ from microscopes (atomic force or scanning tunnelling microscope) can significantly enhance the signal although just locally (Pettinger, Ren, Picardi, Schuster, & Ertl, 2004).

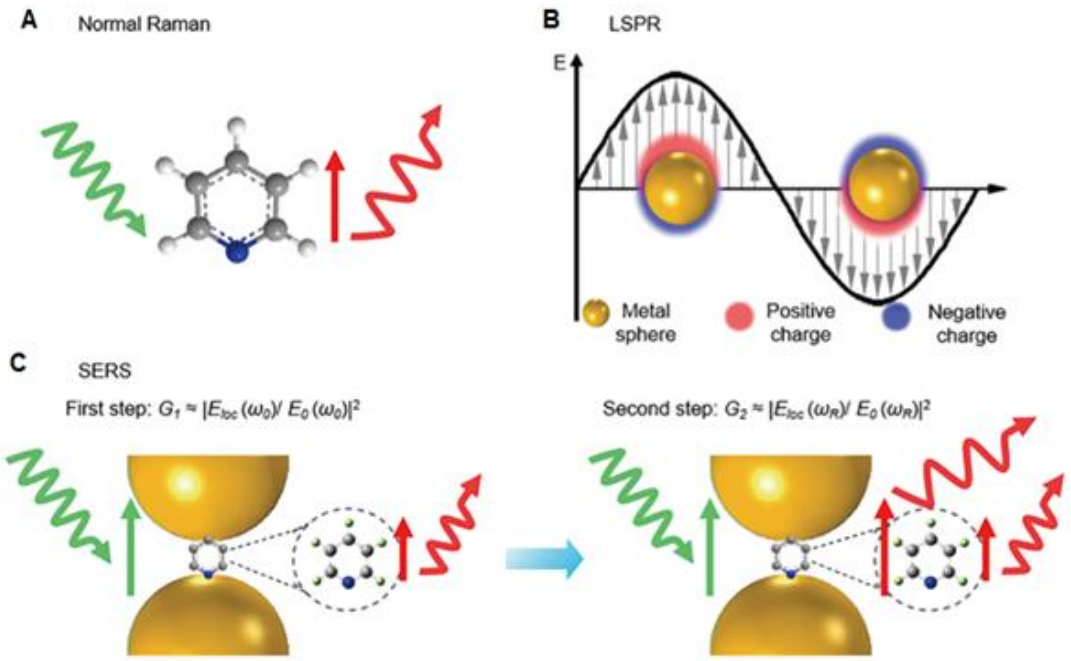

Figure 7 Schematic illustration of (A) Raman Microspectroscopy (B) localized surface plasmon resonance (SPR) and (C) surface enhanced Raman spectroscopy (SERS) (Zong et al., 2018).

SERS has a wide range of applications and is already used in different settings. There are several publications, which analysed blood plasma and serum samples using this method, for example. Also, quantification approaches like measurement of creatine concentration in human serum by using labelled isotopes of creatine as an internal standard are reported (Stosch, Schiel, Gu, & Raman, 2005). Another publication tried to distinguish different cancer types (liver, colonic, gastric, nasopharyngeal, esophageal) in blood samples. Their overall aim was to establish a diagnostic model in order to enable a fast identification of carcinomas via patients' blood samples. Although the discrimination between the samples was challenging and needed further investigation, it could be shown that the potential of using SERS for a fast screening is quite promising (Li et al., 2014).
Qian et al. (2008) performed an investigation for the *in vivo* detection of cancer cells and tumors by the use of antibody targeting.
All these outcomes indicate the high potential of SERS and encourage to further investigations and expansions of published experiments.
In the course of my thesis, we focused on measuring supernatants from quiescent and senescent cells by addition of nanoparticles. By mixing dried 40 nm colloidal gold particles with our supernatants, the intensity could be significantly enhanced. To ensure sensitivity and high quality spectra of supernatants, SERS provided a powerful opportunity.

2 | AIMS

2.1 Confirmation of senescence of HDF164

The main part of my master thesis was establishing a method for a fast identification of senescent cells.

Therefore, the first step was to confirm senescence of doxorubicin treated HDFs using several currently well-established biochemical assays like SA-β-Gal, incorporation of BrdU and quantification of certain mRNA targets.

2.2 Classification of senescent and quiescent supernatants based on IL-8 secretion levels

It is already known that senescent cells secrete IL-8 in a higher amount than quiescent ones. Therefore we were interested in establishing a label free biosensor-based assay utilizing this phenomenon.

We tested different settings in order to enable a specific binding of the 8 kDa protein. After finding an appropriate measurement set-up which guaranteed specific binding, different HDF supernatants were analysed and the cellular stages were distinguished based on IL-8 concentration in supernatants.

2.3 Discrimination of cellular states based on specific Raman signatures of cells and supernatants

It was recently published that it is possible to discriminate proliferating from senescent cells based on their specific Raman signatures (Eberhardt, Matthäus, et al., 2017). Our first aim was to reproduce and confirm this result. In addition, we further aimed to distinguish cellular stages by Raman analysis of cell supernatants using SERS.

In collaboration with the Medical University of Vienna we used Raman Microscopy for a different scientific question. The key objective was distinguishing cells and supernatants treated with several anti-cancer compounds from untreated samples. Furthermore, we tried to localise a compound within a cell due to Raman spectra differences caused by structural changes.

3 | EXPERIMENTAL PROCEDURES

All performed experiments are documented in lab books numbers 65/2018 or 119/2018 and were conducted according to good laboratory practice.
Cell culture work was performed in a laminar flow hood under sterile working conditions. All used working materials, which have to be sterilized, were autoclaved at 121°C for at least 20 minutes.

3.1 Cells

3.1.1 HDFs

For characterisation of senescent HDFs, isolated from skin tissue post liposuction, cells were cultivated in a 1:1 mixture of Dulbecco's Modified Eagle's Medium (DMEM) and Ham's F-12 nutrient mixture (F4815, Biochrome). The medium was supplemented with 4 mM L-Glutamine (G7513, Sigma Aldrich) and 10% fetal calf serum (FCS) (F7524, Sigma Aldrich).

3.1.2 Henrietta Lacks (HeLa) cells

HeLa cells were cultivated in RPMI 1640 medium (Biochrome) which was supplemented with 4 mM L-Glutamine (G7513, Sigma Aldrich) and 10% FCS (F7524, Sigma Aldrich).

3.2 Cultivation of cells

The cells were cultivated in roux flasks of various sizes, namely 25 cm^2 (T25), 75 cm^2 (T75) and 175 cm^2 (T175) or in multi-well plates and incubated at 37°C and 7% CO_2 and about 85% relative humidity.

The media, stored at 4°C, was pre-warmed to room temperature before usage in order to guarantee best conditions for cell growth. When 90% confluence was reached, cells were passaged. Based on cell type and doubling rate, cells were sub-cultivated twice a week in a split ratio of 1:2 or 1:3 for HDFs and 1:20 for HeLa cells. After discarding the supernatant using disposable pipettes, cells were washed two times with Dulbecco’s phosphate buffered saline (PBS) (L1820, Biochrom). PBS has similar ion concentrations and pH value (pH = 7.4) as the human body and is important for removal of FCS residuals.

For detachment, cells were incubated with a mixture containing 0.1% trypsin (27250-018, Gibco) and 0.02% EDTA (E6511, Sigma Aldrich) in PBS for about 4 minutes at 37°C. After microscopic confirmation of cell detachment, cells were re-suspended with fresh media and transferred in new culture flasks. All used culture formats and the corresponding amounts of liquids are listed in Table 1.

Table 1 Used vessels formats for cell cultivation

Culture vessel	Medium for cultivation [mL]	PBS [mL]	Trypsin [mL]
T175/ flask 175 cm^2	35	15	1.5
T75/ flask 75 cm^2	15	10	1
T25/ flask 25 cm^2	5	5	0.5
6-well plate/ 9.4 cm^2	2	2	0.2
µ-Slide 4-well chamber/ 2.2 cm^2	0.5	0.5	-

For characterisation of senescent cells, HDF164 were thawed at a population doubling (PD) level of 14.5. The parental cell bank was at PD 3.5. The adherent cells were isolated from an abdominoplasty and were derived from “Evercyte” (Cat# CPT-008-0164; Lot# 2013-0132).

3.2.1 Cell count and viability

For determination of the cell count as well as the viability, Vi-CELL™ XR Cell Counter (Beckman Coulter) was used. The underlying principle of this cell counter is explained by the dye trypan blue, for which undamaged cell membranes are impermeable in contrast to dead cells. For counting, cells were harvested as previously described and an aliquot of 1 mL of cell suspension was used for the automatic cell counter device.

3.2.2 Induction of senescence

For induction of pre-senescence, HDFs were treated with doxorubicin according to an in-house implemented protocol.

When cells reached a certain donor dependent number of PDs between 13 and 24, they were seeded at a cell density of 3500 cells/ cm^2 and underwent doxorubicin treatment, further specified in Table 2. PD was calculated according to the formula:

$$\mathrm{PD}^{\mathrm{n}} = \mathrm{PD}^{\mathrm{n-1}} + \left[\frac{\ln\left(\frac{\text{cell number}^{\mathrm{n-1}}}{\mathrm{cm}^2}\right)}{\ln\left(\frac{\text{cell number}^{\mathrm{n}}}{\mathrm{cm}^2}\right)} / \ln(2) \right]$$

The corresponding concentration of doxorubicin was freshly prepared by pre-diluting a stock of 5 mM doxorubicin (Sigma) 1:100 in cultivation medium to 50 µM. After at least two weeks of recovery post treatment, cells were ready for analysis. Microscopic images for observation of morphologic changes were taken twice a week.

Table 2 Protocol of doxorubicin treatment to induce premature senescence

Time	Treatment
Day 0	Seeding in appropriate flasks or plates
Day 1	Doxorubicin treatment (100 -200 nM)
Day 5	Doxorubicin treatment (100- 200 nM)
Day 12	Media change (1st week recovery)
Day 19	Media change (2nd week recovery)
Day 26	Analysis (3rd -5th week)

3.3 Characterisation of senescent HDF164

3.3.1 Senescence associated β-Galactosidase assay (SA-β-Gal)

One way to determine senescence of cells is based on the activity of the biomarker β-Galactosidase. Cells in a 6-well plates at different stages (proliferating, quiescent and senescent) were washed and fixated for 10 minutes with 2% Formaldehyde/0.2% Glutaraldehyde (Sigma Aldrich) in PBS. Subsequent to several PBS washing steps, cells were rinsed with staining buffer (pH = 6.0) and incubated overnight at 37°C with a mix of potassium ferricyanide, potassium ferrocyanide, $MgCl_2$, X-Gal and staining buffer. Coating the cells with 70% Glycerol prolongs storage at 4°C.

3.3.2 Fluorescence-activated cell sorting (FACS) analyses

3.3.2.1 Apoptosis assay

In order to determine the viability of cells, an apoptosis assay based on cell membrane permeability was performed.

We used propidium iodide (PI) (P1607, Sigma-Aldrich), which is an indicator for early and late apoptotic cells as it passes damaged cell membranes due to less membrane integrity (Rieger, Nelson, Konowalchuk, & Barreda, 2011). In addition, cells were stained with Pacific Blue™ conjugated Annexin V (640918, Biolegend). Annexin V is expressed in living organisms and can interact with phosphatidylserine of cell membranes, which flips to the outside in case of apoptosis (Lizarbe, Barrasa, Olmo, Gavilanes, & Turnay, 2013).

HDF164 were washed and harvested. Flasks were rinsed with 10% FCS in PBS. The aspirated supernatants and all washing solutions were combined with the cell suspension in order to avoid cell loss. After a centrifugation step of 10 min (200 g), the supernatant was gently discarded. The resulting pellet was washed two times with Annexin V and centrifuged (10 min, 170 g). Cells were re-suspended in 100 µL of an Annexin/PI mix containing Annexin binding buffer, Annexin Pacific Blue and PI. As controls, one flask was treated with PI only and another one with Annexin V only. As a positive reference, one flask was treated for 24 h with 300 nM Staurosporin (S6942-200UL, Sigma) to induce apoptosis.

All samples were incubated at room temperature for 15 min. After adding 200 µL of Annexin binding buffer, the samples were wrapped into foil and kept on ice until FACS analysis.

3.3.2.2 Bromodeoxyuridine (BrdU) staining

BrdU was used to determine cell proliferation as it is incorporated into replicated DNA during regular cell cycle and detected via anti-BrdU antibody.
Cells were incubated for 24 h in medium containing 10 µM BrdU. Buffers and reagents, needed for the assay, had already been prepared by a lab member and were ready to use.
After harvesting and centrifugation (10 min, 170 g), the supernatant was discarded. By dropwise adding of ice-cold 70% Ethanol (while vortexing), cells were fixated and incubated for 15 min at 4°C, followed by centrifugation (5 min, 400 g). 1 mL of 2 M HCl/ 1% Triton X-100 (X100-5ML, Sigma Aldrich) were added and cells were gently re-suspended. 30 min incubation at room temperature ensures complete denaturation of DNA. For neutralisation, 1 mL of 0.1 M Na-Borat (pH 8.5) (S9640-25G, Sigma Aldrich) were added after centrifugation (5 min, 400 g). After that, cells were centrifuged (5 min, 200 g) and incubated for another 30 min at room temperature after re-suspension in 300 µL TBS (0.5 % Tween20, 1% BSA in PBS) + 6 µL Anti-BrdU (347580, BD Biosciences). Subsequent to washing using 5 mL TBS, 200 µL TBS + anti-mouse FITC antibody (F8264-1ML, Sigma Aldrich) were added and incubated for 30 min at room temperature. Before transferring the samples into a fresh FACS tube, cell pellets were washed using PBS, centrifuged (5 min, 400 g) and re-suspended in 200 µL PBS + 2.5 µg/mL PI (P1607, Sigma Aldrich). For appropriate gating of flow cytometry results, controls were prepared by treating samples only with BrdU, PI or FITC.

3.3.3 RNA quantification

3.3.3.1 Isolation of RNA using TRIzol® (Invitrogen)

For characterisation and identification, mRNA levels were quantified and RNA was separated from other cellular compounds as well as RNAses.
The isolation was done in technical triplicates for each cell condition (proliferating, quiescent, senescent).
Supernatant was discarded, followed by two washing steps with PBS. Then, cells were harvested, transferred into nuclease free tubes (72.692 Sarstedt) and collected via centrifugation at 600 g for 10 minutes at 4°C. Cells were washed again two times by re-suspending with 1mL PBS. As we had less than 1x 10^6 cells, the pellet was gently re-suspended in 500µL TRIzol® (Invitrogen). After 5 min of incubation at room temperature, the samples were transferred into RNAse-free tubes and stored at -80°C.

3.3.3.2 Purification of RNA

All the following working steps were performed under a special hood. The whole workspace was cleaned using special NaseZAP® wipes (AM9780Life Technologies).

-80°C stored samples were fully thawed on ice before addition of 100 µL Chloroform (C2432 Sigma Aldrich). After inverting, the samples were shortly vortexed, incubated at room temperature for 3 min and centrifuged (15 min; 12000 g) at 4°C. This centrifugation step initiates a phase separation. In the lower organic phase, proteins accumulate; RNA is solved in the upper aqueous phase. 200 µL of the aqueous phase were gently transferred into a new nuclease-free tube. To induce precipitation of RNA, 250 µL Isopropanol (20922.394 VWR Chemicals Prolab) and for visualisation of the cell pellet 1 µL GlycoBlue (AM9516 Life Technologies) were added. Samples were vortexed, incubated for 10 min at room temperature and centrifuged (10 min, 12000 g) at 4°C. The pellet was washed using 500 µL of 75% Ethanol and another centrifugation step (5 min, 7500 g) at 4°C was performed. The supernatant was discarded and the pellet dried at room temperature. The remaining pellet was re-suspended in 20 µL NFW and incubated for 10 min at 57°C on the heating block.

RNA concentrations and purification of the samples were determined via NanoDrop™Spectrophotometer (Thermo Scientific). Absorbance was measured at 260 nm. 260/280 ratio demonstrates the purity of the sample from protein contaminations. A value of about 2.0 is characteristic for purified RNA. The absorbance ratio of 260/230 should be in the range of 2.0-2.2 and is another indicator for the degree of purity from phenolic compounds.

3.3.3.3 Complementary DNA synthesis

Based on the RNA template, reverse transcriptase (RT) and complementary primers were used to synthesize cDNA. cDNA functioned as template for the following polymerase chain reaction (PCR). Within reverse transcriptase polymerase chain reaction (RT-PCR), RNA levels were quantified.

All reagents needed for the experiment were slowly thawed and stored on ice. As 500 ng of RNA were used as template, every sample was diluted with NFW to a total volume of 10 µL.

The master mix for one reaction is listed in Table 3.

Table 3 Mastermix for high capacity cDNA reverse transcriptase synthesis

Reagent	Volume needed for one reaction (µL)
10x RT buffer	2
25x dNTP mix (100 mM)	0.8
10x random primers	2
Rnase inhibitor	1
Multiscribe reverse transcriptase	1
NFW	3.2
Template (500 ng RNA)	10
Total	20

To become aware of potential contaminations, one reaction mix without any template was included as control (no template control = NTC). The cDNA synthesis was performed in a thermocycler according to the manufacturer's instructions. A detailed program for cDNA synthesis is listed in Table 4.

Table 4 Thermocycler program for cDNA synthesis

Step	Time [min]	Degree [°C]
1	10	25
2	120	37
3	5	85
4	25	∞

3.3.3.4 Quantitative PCR (qPCR)

qPCR as an accurate and rapid method for achievement of highly reproducible results and was used for quantification of expression levels which are supposed to show differences depending on the cellular state (Nygard, Jørgensen, Cirera, & Fredholm, 2007).
All the results were normalized to three commonly used housekeeping genes (GAPDH, ACTB, B2M).

3.3.3.4.1 Preparation of standards

Although several standards were organised in-house and ready to use, some had to be prepared freshly.
One 2 µL aliquot of cDNA sample was used as template for PCR amplification. GoTAQ® DNA Polymerase kit (M300 Promega) and in-house designed primers were used. The reaction was performed in a thermocycler according to the manufacturer's instructions. All components for the GoTAQ® pPCR reaction mix are represented in Table 5.

Table 6 gives detailed information about the thermocycler PCR program.

Table 5 PCR master mix for GoTAQ® Polymerase

Reagent	**Volume needed for one reaction (µL)**
dNTPs	1.0
Primer sense	1.0
Primer antisense	1.0
Reaction buffer	10.0
GoTAQ	0.25
Water	34.75
Template	2.0
Total	50.0

Table 6 PCR amplification using GoTAQ® Polymerase

Temperature (°C)	Time	Repetition
95	5 min	
95	30 s	50
54	30 s	
72	1 min	
72	5 min	
16	∞	

After PCR amplification, the PCR product was verified according to its size and therefore separated by agarose gel electrophoresis. 3 µL of Midori Green DNA stain (MG02-MP Biocat) were added to 50 µL of total sample volume. This mixture was loaded onto a 2% agarose gel in 1x TAE buffer (Tris-acetate-EDTA) containing 3 µL of Midori Green DNA stain. The voltage was set to 130 V for 45 min. The resulting band was excised under UV light and transferred into a 1.5 mL tube. DNA was purified using FavorPrep™Gel Purification Minikit (FAGCK001 FavorgenBiotech Corp.). The protocol was followed according to the manufacturer's instructions.

Briefly, 750 µL FADF buffer were added and, after vortexing, placed on the heating block at 55°C until the gel was fully dissolved. 800 µL of the sample were transferred onto a column and centrifuged at 11000 g for 30 s. After discarding the flow through and a washing step using 70% ethanol, the sample was eluted with 40 µL NFW by centrifugation (30 s, 18000 g).

The dsDNA content and purification level were determined via NanoDrop™One spectrophotometer (Thermo Scientific). By using the below mentioned formula (Staroscik, 2004), the number of copies of the template was calculated. Based on this result, a correct dilution of 10^9 copies μL^{-1} was prepared and used as qPCR standard.

$$\text{number of copies} = \frac{(\text{amount} * 6.022\text{x}10^{23})}{(\text{length} * 1\text{x}10^9 * 650)}$$

3.3.3.4.2 Quantitative PCR (qPCR)

All reagents needed to perform this experiment were fully thawed and pipetted on ice using the pre-cooled loading block, which has space for 96 x 0.2 mL tubes. For mRNA analysis, 5x HOT FIREPol™ EvaGreen™ qPCR Mix Plus (ROX) (08-24-00020 Solis Biodyne) was used.

EvaGreen™ binds on single and double-stranded DNA and is widely used for detection and quantification of dsDNA (McDermott et al., 2013). Better stability, DNA binding affinity as well as other physiochemical properties justify its prevalence compared to SYBR Green (Mao, Leung, & Xin, 2007).

Each sample was analysed in technical quadruplicates. Six concentrations built the standard curves ranging from 10^3-10^9 copies μL^{-1} and were measured in duplicates. Ensuring the quality and validity of our results, controls using NFW instead of cDNA template and using a cDNA sample without any template (NTC) (as previously described) were measured in duplicates. Every target was analyzed in a separate run of Rotor-Gene® 6000 (Qiagen) thermocycler using the rotor-disc for 72 samples. Detailed information regarding the reagents, volumes and thermocycler program needed to perform a qPCR are listed in Table 7 and Table 8. The annealing temperature is depending on the different primers used.

Table 7 qPCR reaction mix

Reagent	**Volume needed for one reaction (µL)**
Reaction buffer (5x HOT FIREPol™ EvaGreen™ qPCR Mix Plus)	2
Primer Sense	0.25
Primer Antisense	0.25
NFW	6
cDNA Template	1
Total	10

Reliable control genes, so called housekeepers, were used to normalize mRNA level results.
GAPDH (Glycerinaldehyd-3-phosphat-dehydrogenase), ß-Actin (ACTB) and B2M (β2-microglobulin) fulfil characteristics for housekeeping genes like high stability, reproducibility and minimal variability in expression (Ametrano, 2016).

Table 8 EvaGreen™ qPCR cycle profile

Step	**Temperature (°C)**	**Time (s)**	**Cycles**
1 Activation	95	600	1
2 Denaturation	95	15	45
3 Primer annealing	*	30	
4 Extension	72	15	
5 Melting curve	100	0	1

*primer dependent

3.3.4 Protein analysis

One 250 µL aliquot of already prepared 2 x TNE buffer was mixed with 250 µL NFW, 20 µL of phosphatase inhibitor (PhosSTOP 4906837001 Roche) and 25 µL of protease inhibitor (4693132001 Roche).
HDF164 of different stages were harvested and centrifuged at 4°C for 10 min at 600 g after determining cell concentration. Then, the pellet was washed with PBS, re-suspended in 80 µL 1 x TNE

buffer and incubated on ice for 15 min. The samples were vigorously vortexed and centrifuged at 6000 g for 10 min. Supernatant was transferred into a QIAshredder spin column (79656 Qiagen) and centrifuged for 2 min at full speed two times. 70 µL of samples were mixed with 20 µL of 4x loading dye and incubated for 10 min at 95°C. Protein lysates were stored at -20°C.

3.3.5 Luminex® Multiplex Assay

Due to its high sensitivity, this immunoassay based technique was chosen to be an appropriate method for measuring several cytokines in HDF164 supernatants. 24 h before sampling, the media was changed to FCS free DMEM Ham's media. Cells were harvested and the concentration was determined. After centrifugation for 15 min at 600 g, 400 µL of supernatant was transferred into fresh Sarstedt tubes. The samples were analysed by the Medical University of Vienna.

3.4 BLI

BLI is a novel and non-invasive method. Without enzymatic, fluorescent, or radioactive labelling, quantification as well as kinetic constants can be obtained. Also, binding profiles and protein interactions can be monitored in real-time (Wartchow et al., 2011).

3.4.1 Sample preparation

Cells (HDF76, HDF85, HDF161, HDF164) were treated with doxorubicin and supernatants of contact-inhibited, proliferating and senescent cells were aspirated and transferred into fresh Sarstedt tubes. Without labelling or additional purification, samples were measured immediately.

3.4.2 Antibody labelling

IL-8 monoclonal antibody (M801, Thermo Fisher Scientific) was labelled using LYNX Rapid HRP Antibody Conjugation Kit® (LNK002P, Abcam) according to the manufacturer's instructions. Briefly, 100 µL of antibody were gently re-suspended in 10 µL modifier reagent. The mixture was slowly pipetted onto LYNX lyophilized mix and also re-suspended. After an overnight incubation at room temperature, 10 µL of quencher reagent were added. The HRP labelled antibody was ready to use after another incubation of 30 min.

3.4.3 Instrumentation

All measurements were performed using Octet Red96e (ForteBio, Menlo Park, CA, USA) in black 96-well plates (Nunc F96 MicroWellTM Plates, Thermo Fisher Scientific, Langenselbold, Germany) to keep the scattering light as low as possible.
Measurements were performed automatically after set-up of all working parameters. Before performing an assay on Octet, various factors like buffer and solution preparation as well as adjustment of all instrument parameters have to be considered to guarantee reliable outcomes. Shaking speed, temperature and measuring times of all required steps were set up. We selected a constant shaking at

1000 rpm for equilibration, loading and association and 25°C as an appropriate temperature for all measurements. Every loading step was carried out for 900 s. Washing steps, which were performed after each solution change, were set to 60 s. The DAB association step was performed for 600 s. Samples were measured in duplicates and various concentrations of recombinant IL-8 protein ranging from 25 up to 1250 pg mL^{-1}, as required for the standard curve, were measured in triplicates. The overall working volume was 200 µL.

3.4.4 Processing and analysis of data

All recorded data were analysed using Octet Software (Version 6.4, ForteBio). Raw data were imported, the standard curve was generated using the R equilibrium algorithm and fitted with the linear regression model.
Average signal responses of different replicates of the same sample were calculated.

3.5 Raman Microspectroscopy

Raman Microspectroscopy is a non–invasive, label free technology and requires just little sample preparation.
Experiments were mainly performed with HDFs of different donors.
In addition, samples provided by the Medical University of Vienna were measured. A variety of conditions and experimental set-ups was tested.

3.5.1 Preparation of cells

For the experimental part, cells from different donors (HDF76, HDF161, HDF164) were seeded at a cell density of 3500 cells/cm^2 in a µ-Slide 4-well chamber with glass bottom. In one of the seeded wells, senescence was induced with doxorubicin. In the other wells, cells were incubated at 37°C until they reached contact-inhibition. The volume was 500 µL per well and media was changed twice a week as usual.

For fixation of the cells, supernatant was removed, transferred to Sarstedt tubes and stored at -80°C for further analysis. Cells were washed two times with PBS. 2% Formaldehyde in PBS was added onto the cells and incubated for 5 min at room temperature. After removal of the fixation solution, cells were covered with fresh PBS and were ready for measurement.

For improving signal-to-noise ratio and avoiding glass background signal, CaF_2 slides provide a promising alternative. For this approach, 50 µL of cell suspension were directly pipetted onto CaF_2 slides of different sizes (10 mm Ø x 0.35 mm (Crystan, CAFP22-0.5) and 10 mm Ø x 0.50 mm (Crystan, CAFP10-0.35). To avoid flushing of cells from the slide, cells were incubated for 3h at 37°C until they were settled before filling up the well with fresh media. Before Raman measurement, cells were fixed using 2% formaldehyde.

Advantageously, the slides can be re-used after appropriate cleaning. Therefore, they were washed according to published guidelines of Gstraunthaler Gerhard (2013). After 12 h of soaking in 7X®

detergens (VWR, ICNA097667093), the slides were rinsed with H_2O and submerged for another 12 h in a solution containing 26% ethanol and 2% glacial acetic acid (Merck, 100066).

Another approach was using round protected gold mirrors ((Ø1/2" / Ø12.7 mm, (Thorlabs, PF05-03-M01-10). The preparation procedure was the same as for the CaF_2 slides.

3.5.2 Uptake of nanoparticles into HeLa cells for cell imaging

3.5.2.1 Nanoparticles

As Gratton et al. (2008) published that cellular uptake can be visualized by Raman Microspectroscopy, we performed an experiment based on the uptake of nanoparticles into HeLa cells. Cells were seeded in a µ-Slide 4-well chamber with glass bottom. 24h after seeding 15 µg mL^{-1} of 150 nm colloidal gold particles were added and incubated overnight at 4°C. The particle mixture was discarded, followed by washing and fixation.

3.5.3 Preparation of supernatants

As Raman Microscopy has the big advantage of being non-invasive, our goal was to distinguish the different cellular stages just by recording spectra of the supernatants.

Cells from four different HDF donors (HDF76, HDF85, HDF161, HDF164) were treated with doxorubicin to induce senescence. Supernatants of contact-inhibited cells were measured and compared to those from the senescent cells.

3.5.3.1 Surface enhanced Raman Microspectroscopy

As reviewed by Butler et al. (2016), adding metallic nanoparticles to liquid samples leads to an enhancement in signal up to a factor of 10^{14}. This is achieved by several different approaches like drying supernatants and nanoparticles before measurement or analysing just freshly mixed components. In addition, an increase in signal is reached by just drying the supernatant and freshly adding nanoparticles (or vice versa). According to literature, we tested all these combinations of supernatants and 40 nm colloidal silver (2.6×10^9 particles mL^{-1}; BBI Solutions, cat. no. EM. SC40), 40 nm colloidal gold particles (9.00×10^{10} particles mL^{-1}; BBI Solutions, cat. no. EM. GC40) and 150 nm colloidal gold particles (1.66×10^9 particles mL^{-1}; BBI Solutions, cat.no.EM.GC150)

The supernatant and the nanoparticle suspension were mixed in a 1:1 ratio ending up with a total volume of 30 µL. The experiment was performed in µ-Slide 8-well chambers with glass bottom.

To be totally sure that the drying process was complete, samples were dried overnight in the laminar. Shortly before Raman analysis, fresh particles or samples were added.

After trying all combinations and possibilities, the best Raman signal based on the signal/noise ratio, intensity and resolution was achieved when using 15 µL of dried 40 nm colloidal gold particles and 15 µL freshly added cell supernatant. Therefore, all supernatants were analysed according to this procedure.

Supernatants from RPTEC (human renal proximal tubule cells) and skin equivalent (SE), as well as samples from distinct cell lines of the Medical University of Vienna were provided and also analysed via the Raman instrument.

3.5.4 Instrumentation, Calibration and quality control

All spectra were recorded at room temperature using an inverted XploRA^{TM} Raman microscope (Horiba), linked to a computer providing the software LabSpec 6.

The Raman microscope consisted of a 100 mW 532 nm laser and a 90 mW 785 nm diode laser. The device was equipped with four different gratings 600 gr mm^{-1}, 1200 gr mm^{-1}, 1800 gr mm^{-1} and 2400 gr mm^{-1} as well as with two different fast scanning modules (SWIFT and DuoScan) and a motorized stage with an Okolab UNO PLUS incubation system.

To achieve high resolution, the 100 x oil objective (CFI Plan APO 100x/1.4 Oil, working distance (WD) =0.13 mm (ZK-100XIM-ÖL-TiU)) was used. A 1600 x 200 pixel CCD detector operates cooled and the filter sets to attenuate the laser intensity vary from 100% to 0.1%.

To minimize background signal, all samples were measured using ibidi µ-Slides with glass bottom.

Reproducibility and comparability between different instruments demand an auto-calibration of the used laser and grating combinations using a silicon standard (Horiba, SPR-CO, SN: 141112-01). One auto-calibration, which was performed at the beginning of each measuring day, is shown exemplary in Figure 8.

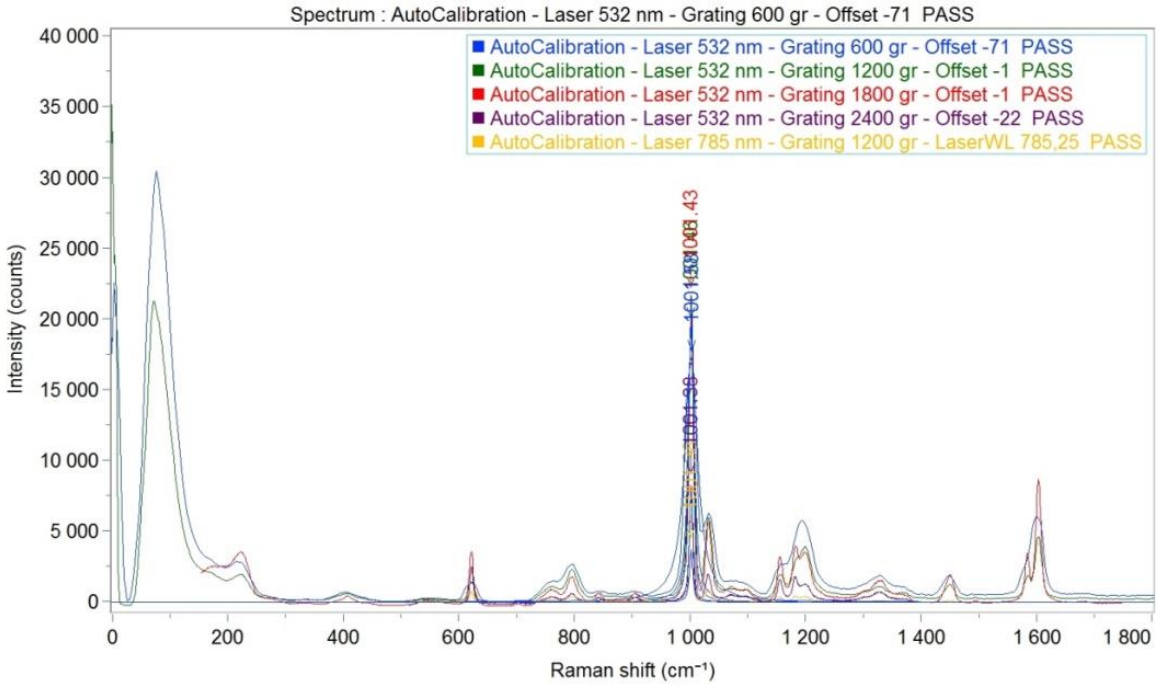

Figure 8 Auto-Calibration of all laser settings and gratings

3.5.5 Spectral acquisition

First, the Raman microscope and computer software LabSpec 6 were switched on. Before data acquisition, a picture of the determined measuring area was taken.
High signal intensities for cell measurements were achieved due to exciting the samples with a laser excitation wavelength of 532 nm, 100 mW laser power and 1800 g mm^{-1} grating.
As samples were cultivated in DMEM Ham's medium including phenol red, fluorescence interfered with the Raman signal. Therefore, the laser was set to 785 nm and the grating to 1200 g mm^{-1} when measuring supernatants.
All chosen parameters for analysis of cells and supernatants by the Raman Microscope are represented in Table 9.

Table 9 Set-up of Raman instrument for measurement of cells and supernatants

Parameter	Cells	Supernatant
Laser	532 nm	785 nm
Grating	1800 g mm^{-1}	1200 g mm^{-1}
Laser spot size	15 µm	3 µm
Slit	100 µm	100 µm
Acquisition time	5 s	10 s
Accumulation	2[a]	2[a]
Duo scan	ON	ON
Hole	300 µm	500 µm
Filter	100%	100%
Spectral region	400-1800 cm^{-1}	400-1800 cm^{-1}

[a] in order to allow automated removal of cosmic rays

3.5.5.1 Raman Imaging

Not only single measurements were recorded, also 2D as well as 3D images can be acquired, meaning that single Raman spectra were sequentially obtained point by point. The distance between each measuring point was defined by a certain map step size. All collected single spectra were finally summarized to one image and an overlay with the previously taken bright field microscopic image is possible. This was done using the software LabSpec 6.

For localisation, choosing the correct mapping area was fundamental. We precisely focused on one specific cell and adjusted the location using the coarse focus adjustment knob and the fine focus adjustment knob. The cell nucleus and partial cytoplasm were imaged within one specimen.
Depending on the size of the chosen area, acquisition of one map took about 3 h. For all measurements we used 100 x oil objective. The conditions for Raman imaging were the same as for single measurements. The step size was set to 0.5 µm.

3.5.6 Data processing and analysis

Acquired Raman spectra were analysed as recommended in published literature (Butler et al., 2016). After data acquisition, all captured spectra were imported into the software Unscrambler X® (CAMO). Raman images were processed in LabSpec 6 (HORIBA). Both software tools have powerful features for analysing and processing spectroscopic data. Unscrambler X® was proved to be useful for evaluating measurements of cells and supernatants due to its potential for multivariate data analysis. Raw spectra are usually plotted by depicting Raman shift in cm^{-1} (x-axis) versus Raman intensity (y-axis).
PCA data were re-plotted using the free software PAST3, represented loadings were illustrated using GraphPad Prism 8.

3.5.6.1 Cells

10-15 single measurements of different nuclei per sample were measured. All spectra were uploaded into the Unscrambler® software and pre-processed. For compensation of Raman shifts due to fluorescence and for enabling comparison of different spectra, a baseline correction was applied. De-trending function subtracts the mean from all data points and thereby removes a systematic shift from the measurements, which can occur due to a sensor drift. This pre-processing makes a direct comparison between the single spectra possible.

As a spectrum contains lots of different variables and is exposed to influence factors, scientific statements and comparisons are rather difficult. Principal component analysis (PCA) reduces the number of different variables to the essential ones which show the greatest differences and highest influence. This mathematical procedure converted the data to a certain number of uncorrelated variables, which are called Principal Components (PC). The different PCs describe the variability of the data and enable a clustering and identification of similarities and significant differences.

When applying this feature, all the samples were categorized according to the known cellular state. PCA led to four separate calculations, which were demonstrated in different plots.

The scores plot indicates the distribution of the data. Samples which have a similar spectrum and show little significant differences will cluster together, while differential spectra will be grouped separately. This plot visualizes the deviation from the mean of total sample amount.

The correlation between two principal components is shown in a separate loading plot. This graph is useful to identify which Raman shift regions account for the biggest difference between the two components. Influence plot demonstrates outliers of the total data. A threshold can be set individually. Another plot shows how much of the total variability can be explained by one component and is stated in %. The higher the value of one component the better the level of separating power. PC-1 explains the highest variability within this data set. Referring to our scientific question the scores and the loadings plot are of major importance.

For cell mapping, classical least squares (CLS) fitting was applied in order to get information about the location of the component within the cell.

3.5.6.2 Supernatants

For two replicates per sample and condition, 10-20 measurements were performed. All the measurements of the supernatant of one cell type were imported in Unscrambler®. Pre-processing and smoothing of raw data was performed by applying a Savitzky-Golay filter. After first-order differentiation, the data lost their typical spectrum-like appearance. Unit vector normalisation reduces variability caused by measurements and thus technical reasons. A PCA was also performed regarding data analysis of supernatants. Resulting Scores plot and loadings were analysed and interpreted.

4 | RESULTS

Senescence as a cellular response can be determined by a variety of different methods and assays. Our findings regarding the characterisation of senescent cells, differences in biological fingerprint regions of Raman spectra in comparison with contact-inhibited cells as well as IL-8 secretion levels in different cellular stages will be outlined in the following.

4.1 Global characterisation of senescence by currently applied assays

For characterisation we treated HDF164 cells with 100 nM doxorubicin at PD 19 according to a developed procedure. By performing several assays with proliferating, senescent and quiescent samples we (1) confirmed that the cells are really in senescent state and (2) compared their behaviour to the other cells stages.

Firstly, typical morphological changes can be observed in Figure 9. While proliferating fibroblasts show typical spindle like structures, senescent cells have a flattened enlarged shape. The completely dense structure of contact-inhibited cells is shown in Figure 9B.

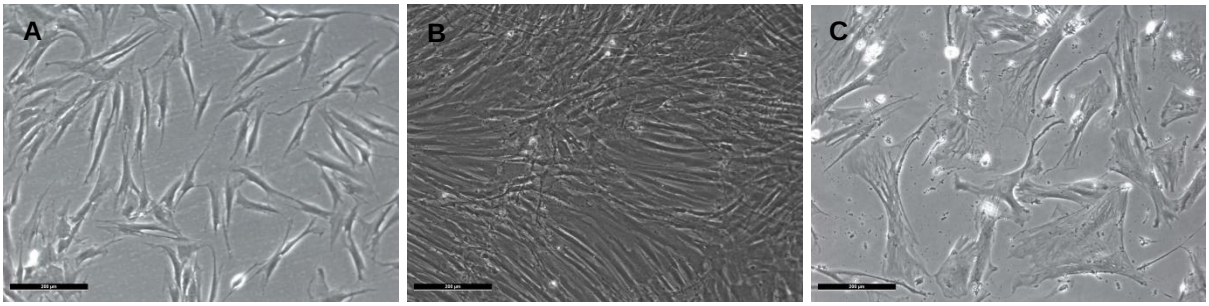

Figure 9 Morphology of (A) proliferating HDF164 (PD 26), (B) quiescent cells and (C) senescent staged cells; scale bar: 200 µm

4.1.1 Senescence associated β -Galactosidase (SA-β-Gal) assay

The SA-β-Gal assay as one marker for senescence (conducted in the third week of recovery after doxorubicin treatment) shows clear differences in microscopic images taken with an integrated modulation contrast (IMC) objective (Figure 10). After fine-tuning of all adjustable parameters, ten pictures per well and condition were taken and the resulting blue stained cells indicate senescence due to an increased enzyme activity.

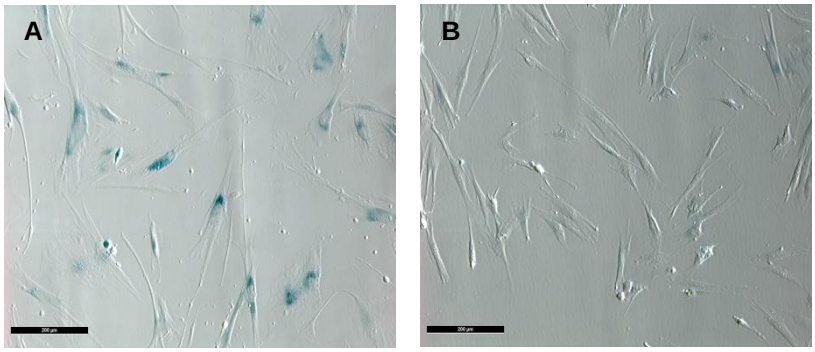

Figure 10 Comparison of microscopic images after ß-Gal staining at pH 6 at a scale bar of 200 µm. (A) Senescent cells are stained blue (B) proliferating cells show almost no β -Gal activity

Evaluation of the images confirms microscopic observations (Figure 11) as more than 95 % of treated cells were identified as β-Gal positive.

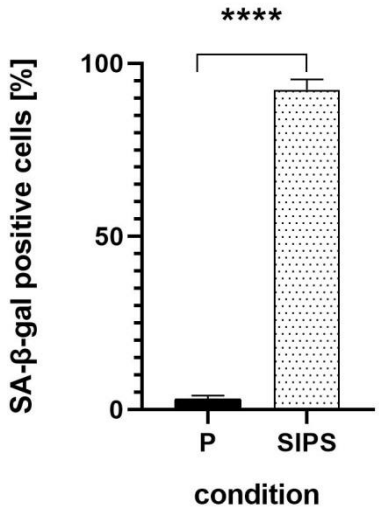

Figure 11 ß-Gal assay confirms senescence of doxorubicin treated cells. All 60 images (30 per condition) were randomized and blinded before counting. From the average percentages, standard deviations of the technical replicates were calculated and a paired Student's t-test setting p<0.05 was performed.

4.1.2 Verification of senescence using flow cytometry

4.1.2.1 Apoptosis assay

After doxorubicin treatment of our cells, we made sure that our fractions are actually senescent and not apoptotic.

To determine early and late apoptotic fractions, we performed an assay based on flow cytometry, which states the percentages of apoptotic cells using Annexin V and PI. Results after FACS analysis are illustrated in

Figure 12. While viable cells (Annexin V^-/PI^-) remain unstained, early apoptotic cells (Annexin V^+/PI^-) and late apoptotic cells (Annexin V^+/PI^+) dye due to a reduced membrane stability.

We determined a significant increase of apoptotic cells in the senescent fraction. However, samples of proliferating and quiescent cells do not show many apoptotic cells.

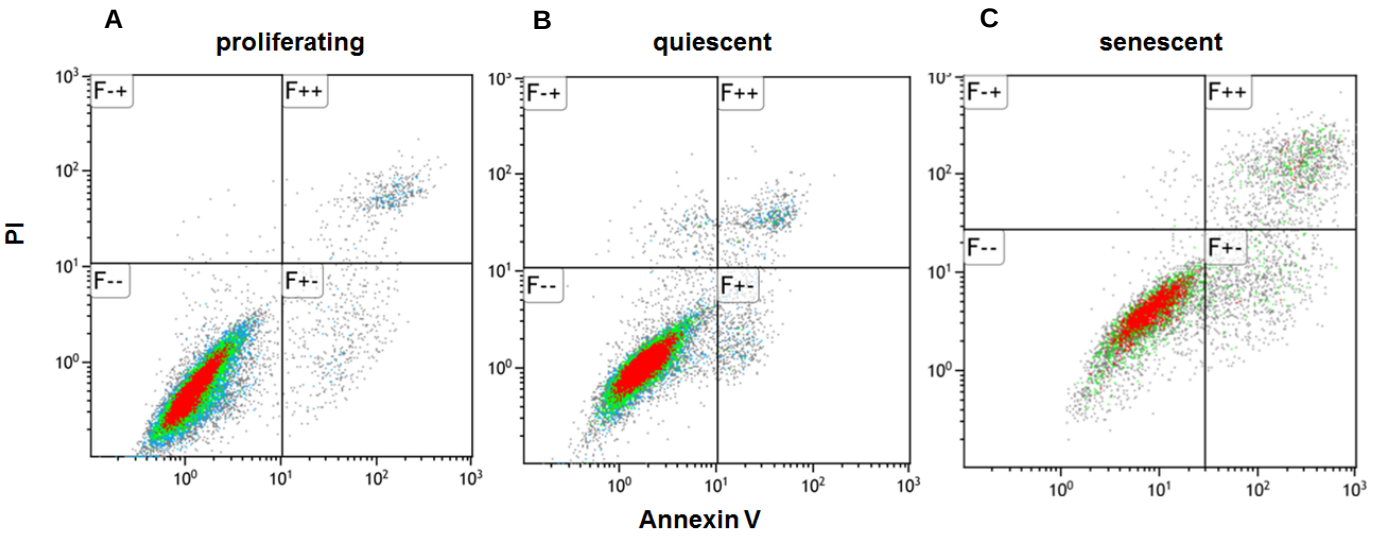

Figure 12 Flow cytometry results of apoptosis assay of proliferating (A), quiescent (B) and senescent (C) HDF164 (Annexin V$^-$/PI$^-$: viable cells; Annexin V$^+$/PI$^-$: early apoptotic cells; Annexin V$^+$/PI$^+$: late apoptotic cells)

The populations of FACS analysis are stated in Table 10. Fractions of proliferating and quiescent cells show viabilities of more than 90%, while the senescent sample contains almost 10.5% apoptotic cells. This result corresponds to our microscopic observations.

Table 10 Representation of results of the apoptosis assay.

	Gated cells [%]		
	viable	**early apoptotic**	**late apoptotic**
proliferating	94.86	2.23	2.25
quiescent	92.23	2.71	2.68
senescent	27.03	4.46	5.96

4.1.2.2 BrdU staining

For identification of proliferative cells and for cell cycle analysis we performed a BrdU-assay. Two senescent fractions did not reach the set event number of 5000.

However, the result in Figure 13 shows BrdU positive cells. As shown by PI staining, contact-inhibited cells are growth arrested in G0/G1 phase and the senescent sample is mainly growth arrested in G2 phase. Both samples result in a negative BrdU signal.

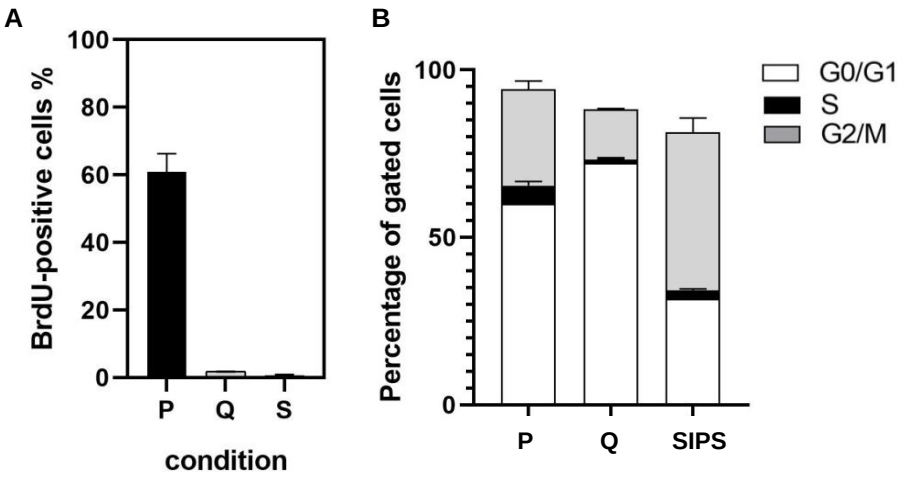

Figure 13 (A) Overview of the BrdU positive cells in all three cell fractions. (B) Cell cycle analyses of HDF164 populations. The experiment was performed in technical triplicates. Data are represented as mean ± SD. The determined event number of 5000 was not reached in two fractions of senescent cells.

4.1.3 Reverse transcription–quantitative PCR (RT-qPCR) for the detection of known senescence biomarkers

Next, we checked if mRNA levels of chosen biomarkers reflect the different cellular states. Cellular senescence promotes secretion of several signal factors like interleukins, proteases or insoluble factors to increase significantly pro-inflammatory cytokines. Therefore RT-qPCRs of selected targets which are supposed to show overexpression in the senescent fraction were performed (T., C., W.J., & D.S., 2010).

Normalization to three different housekeeping genes show almost the same result (Figure 14), indicating that the gained results are valid and reliable.

Interleukin-1, interleukin-8, p21, CCL-2 mRNA levels are increased in doxorubicin treated cells, as expected. Interestingly, interleukin-6 and fibrillarin mRNA was at a higher concentration in quiescent cells. RT-qPCR of CCL-2 and NML show a high variation, especially in the senescent samples.

NSUN5 mRNA expression levels are almost the same in quiescent and senescent cells.

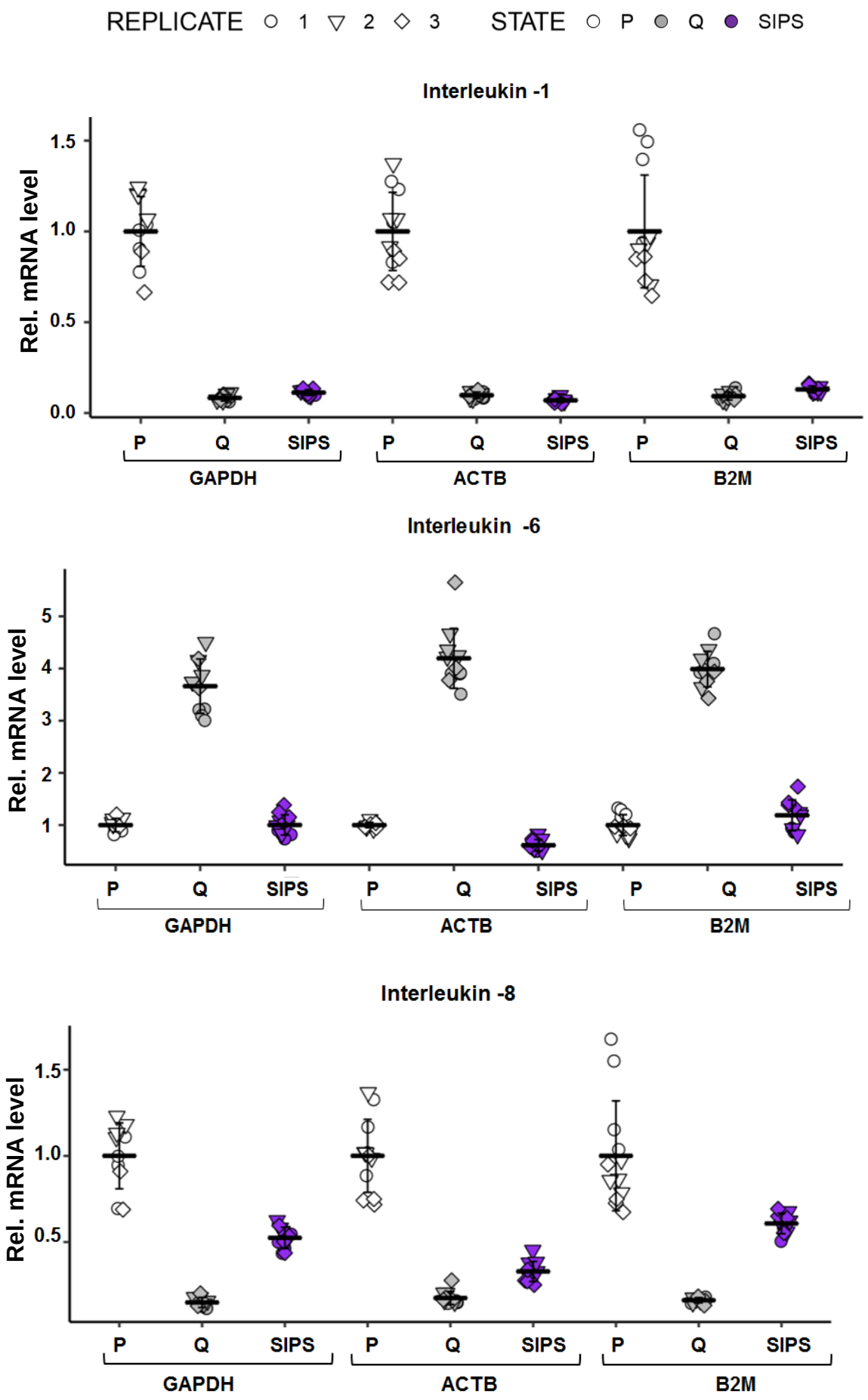
REPLICATE 1 2 3
STATE P Q SIPS
Interleukin -1
Rel. mRNA level
1.5
1.0
0.5
0.0
P Q SIPS P Q SIPS P Q SIPS
GAPDH ACTB B2M
Interleukin -6
Rel. mRNA level
5
4
3
2
1
P Q SIPS P Q SIPS P Q SIPS
GAPDH ACTB B2M
Interleukin -8
Rel. mRNA level
1.5
1.0
0.5
P Q SIPS P Q SIPS P Q SIPS
GAPDH ACTB B2M

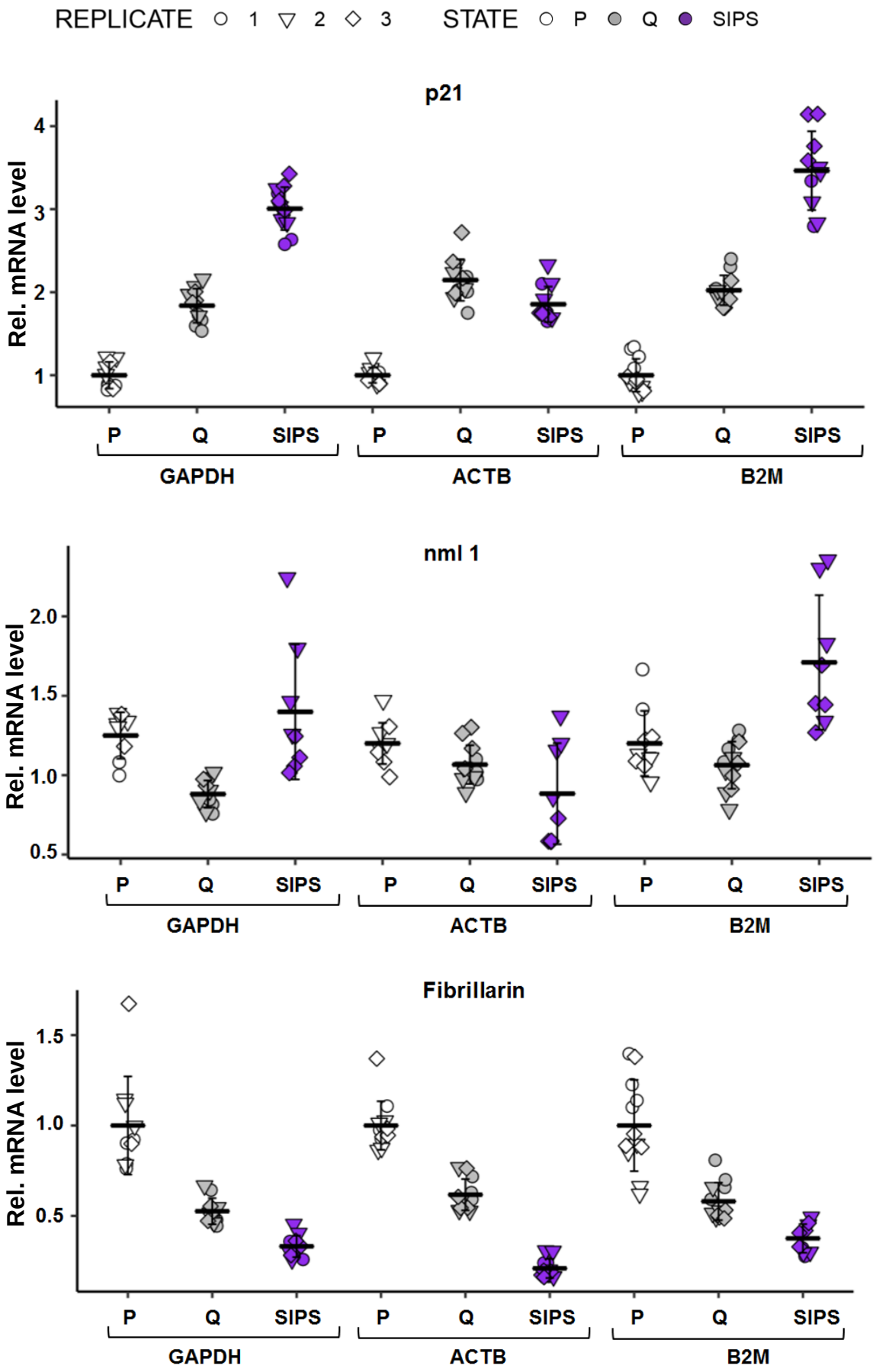
REPLICATE 1 2 3
STATE P Q SIPS
p21
nml 1
Fibrillarin
Rel. mRNA level
P Q SIPS P Q SIPS P Q SIPS
GAPDH ACTB B2M

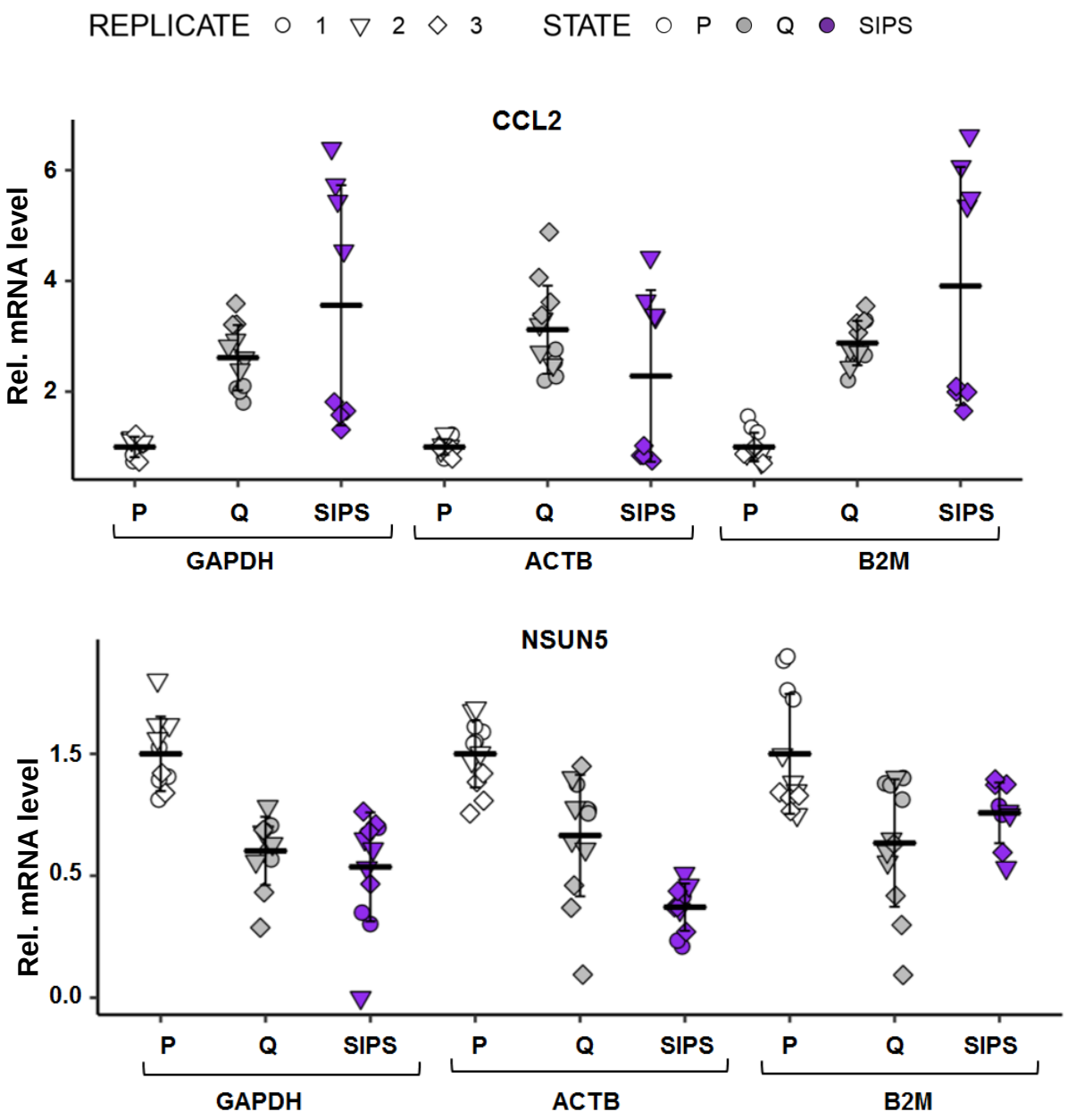

Figure 14 qPCR results of certain target genes showing expression levels in proliferating, quiescent and senescent HDF164. The experiment was performed in biological triplicates using HDF164. RT-qPCR machine as well as pipetting variations were monitored by measuring each sample in technical quadruplets. Results were normalized to the three different housekeeping genes GAPDH, ACTB and B2M.

4.1.4 Luminex® Multiplex Assay

Finally, a multiplex assay was performed by the Medical University of Vienna. The advantages of this high-throughput technology lie in its speed, efficiency and high reproducibility (Khalifian, Raimondi, & Brandacher, 2015).

IL-8 concentrations are illustrated in Figure 15. The resulting concentrations were normalized to the cell number to obtain the secretion of one cell. Results indicate a slightly higher IL-8 secretion of senescent compared to quiescent cells.

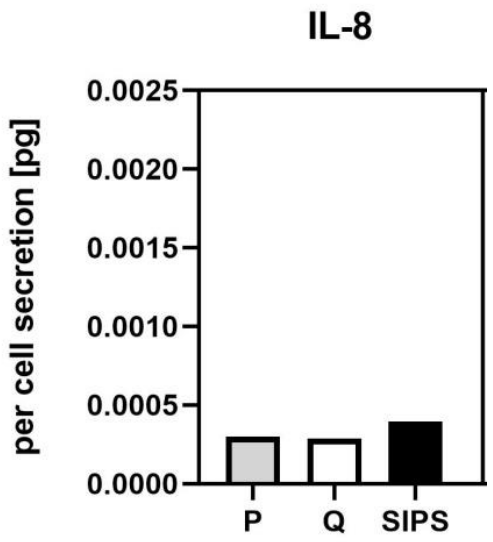

Figure 15 Results of Luminex® Multiplex measurement of HDF164 supernatants

All these experiments verified that cells treated with doxorubicin show senescence-associated characteristics. This was proofed and confirmed by a combination of different assays.

4.2 BLI results

Based on the collected preliminary results of the performed qPCR and Luminex, a higher expression of IL-8 was observed in the senescent fraction. For this reason we aimed to develop an assay for measuring IL-8 concentrations in supernatants of different HDF donors and in different cellular states.
A variety of conditions and settings were tested for establishing an appropriate quantitative assay.

4.2.1 Assay development

Since we had no previous experience, a variety of different experimental set-ups was tested and evaluated. We strived for the determination of the best measuring conditions and development of a proper assay.
In order to quantify our samples in a realistic matrix, we set up a standard curve in DMEM Ham's media using recombinant human IL-8 protein (Sino Biological, 10098-HNCH2).
Due to its high affinity, streptavidin-biotin systems became often used model systems for studying protein-ligand interactions (Chivers, Koner, Lowe, & Howarth, 2011). We decided using streptavidin (SA) biosensor tips (ForteBio) for establishing a robust and sensitive assay in order to reduce potential non-specific bindings.

Before usage, biosensors were activated according to the manufacturer's instructions using a kinetic buffer (K-buffer) followed by an equilibration for another 120 s.
SA- biosensors were loaded with 10 µg mL^{-1} of biotin-labelled IL-8 monoclonal antibody (M802B, Thermo Fisher Scientific). Before the first loading step, sensors were blocked using 1% bovine serum

albumin (BSA) in order to avoid non-specific binding. Tips with bound target were dipped into our sample solution and afterwards loaded with an IL-8 monoclonal antibody (M801, Thermo Fisher Scientific), which we previously labelled with HRP, having a concentration of 25 µg mL^{-1}. 3,3′-diaminobenzidin (DAB), solved in 21 mL PBS, functions as chromogenic substrate for HRP to gain signal enhancement by forming a brown coloured agent, which is insoluble in water.
Basically, we tried setting up a sandwich enzyme-linked immunosorbent assay (ELISA) on our SA - biosensors to receive maximum signal and enable quantification in ng mL^{-1} range. All important steps of the assay are illustrated in Figure 16.

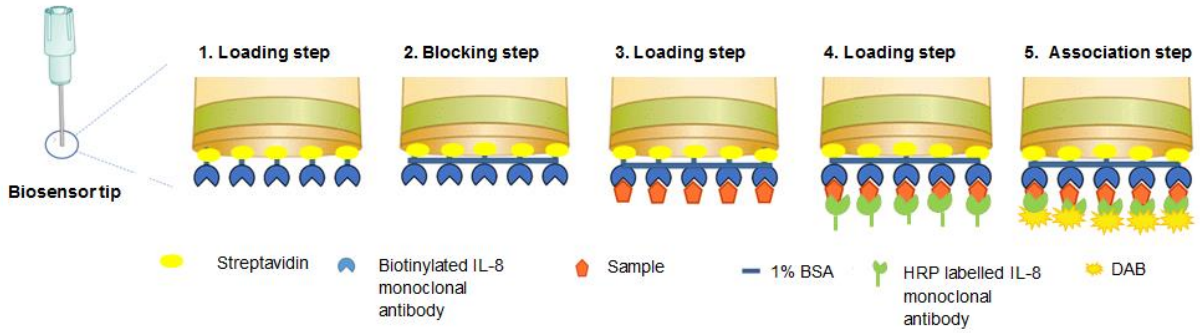

Figure 16 Schematic illustration of representative steps of the developed octet assay for quantification of IL-8 adapted from Carvalho et al. (2018). Initial equilibration and washing steps are not shown. Loading of biotin labelled antibody on streptavidin tips (1) is followed by blocking (2). Sensors are dipped into sample supernatant (3) and using a HRP-labelled antibody (4) and DAB (5) as substrate lead to strong binding in the ng mL^{-1} range.

Ideally, all dilutions and measuring steps should be performed in DMEM Ham's media as this is the matrix of our sample. Therefore, we decided diluting our first antibody in DMEM Ham's media. As we had a change in the matrix due to blocking in BSA, the second antibody was also diluted in 1% BSA. Importantly all reagents can be used several times.
To confirm stability and ensure the resulting binding rates are not caused due to non-specific interactions, the assay was additionally performed omitting first antibody, target protein or second antibody.
In order to exclude artefacts and verify concentration- dependent binding rates, a serial dilution of one sample was performed.

4.2.2 Preliminary trials

Preliminary to the final set-up described above, a couple of other antibodies and measurement series were intended but did not prove to be successful. When performing the established assay without using the second antibody or omitting the DAB step, quantification was not possible in our samples due to the low IL-8 concentration. Using biocytin instead of BSA as blocking reagent did not avoid unspecific binding.
IL-8 antibody (C-11) (sc-376750, Santa Cruz (Szabo Scandic)), IL-8 antibody (B-2) (sc-8427, Santa Cruz (Szabo Scandic)), anti-human IL-8 (554716, BD Pharmingen), Biotin Monoclonal Antibody

(Z021), HRP (033720, Thermo Fisher Scientific) were tried in different settings and concentrations but turned out to be not compatible.

4.2.3 Final assay procedure

Figure 17 describes the final quantification procedure. Measurements were performed in parallel and recorded online in kinetic modus. The last step illustrates the association step, which was used for quantification.

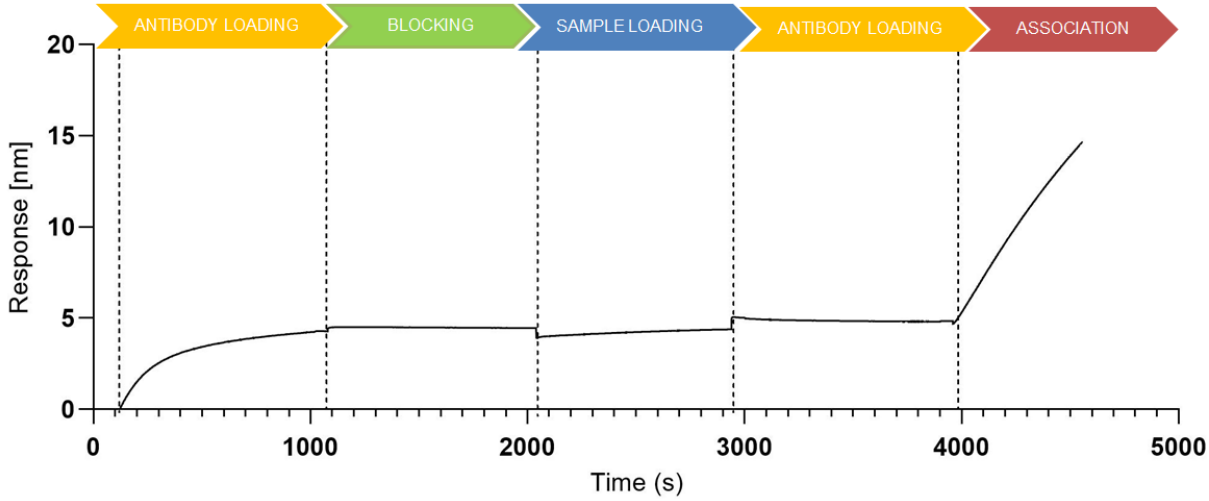

Figure 17 Representation of one single BLI measurement on streptavidin coated biosensor tips: (1) Recording a baseline using K-buffer followed by a loading step with 10 µg of biotinylated IL-8 antibody per mL K-buffer (2). Step (3) describes blocking with 1% milk powder in PBS-T. Following, the sensors were dipped in sample solution (4). Step (5) depicts sensor loading with 25 µg of HRP labelled IL-8 antibody per mL milk powder (1%) in PBS-T. Final, association is recorded using DAB leading to an increased signal (6). After each loading, a washing step (60 s) is performed.

Resulting standard curve in

Figure 18 shows high reproducibility of single measurements. It nicely illustrates the relationship between the concentration of recombinant IL-8 protein and the recorded binding response in a range of 25 up to 1250 pg mL^{-1}.

However, the detection limit of this set-up is 10 pg mL^{-1}. Binding rates were fitted using a linear regression model.

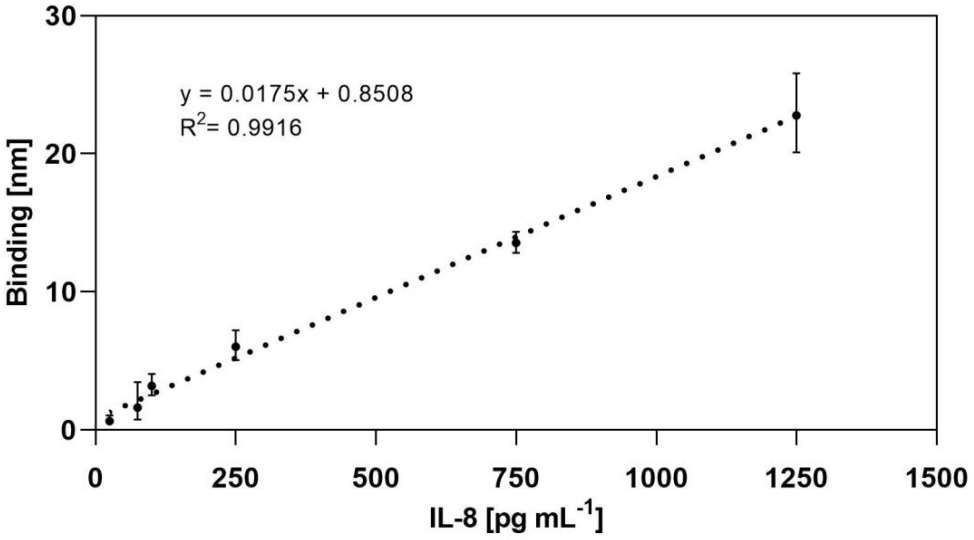

Figure 18 Standard curve of Octet measurement after fitting with a linear algorithm; concentration range varies from 25 up to 1250 pg mL^{-1}. Measurements were performed in triplicates.

Based on the calculated calibration curve, supernatants of all donors were measured and quantified using the same set-up and conditions.

As we missed to determine the cell concentration of each sample, the cell number of HDF164 was used for all donors (Table 11). It is known from several prior experiments that the cell count of the different donors is within the same range.

Table 11 Cell concentration of HDF164 of different states

Cell stage	Cell number per mL
Proliferating (P)	0.23 x10^6
Quiescent (Q)	0.34 x10^6
Senescent (S)	0.018 x10^6

Figure 19 illustrates the outcome of BLI measurements. Senescent supernatants show higher concentrations than quiescent ones in all donors. However, HDF161 demonstrates the highest difference.

Due to low signals in donor HDF164, a valid quantification was not possible.

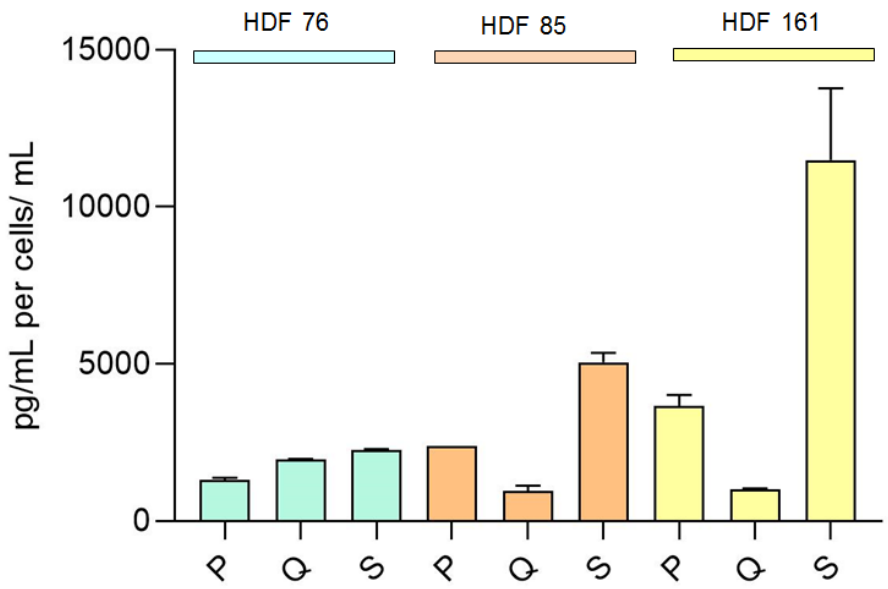

Figure 19 HDF samples measured via BLI. Based on the binding rates the concentrations per mL were calculated (P = proliferating; Q = quiescent; S = senescent).The error bars represent the standard deviation.

To exclude measuring artefacts, a dilution series was performed. By diluting one sample 1:2, 1:4 and 1:6 the dependency of binding rate and concentration was checked. All measurements were fitted using a linear correlation visualized in Figure 20.

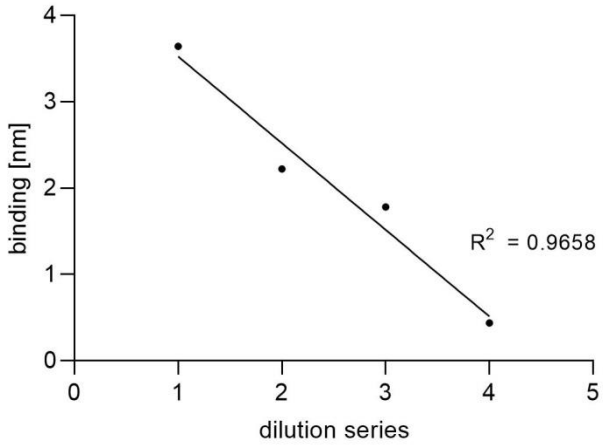

Figure 20 Linear correlation of one sample vs. binding rate: (1) undiluted, (2) 1:2, (3) 1:4, (4)1:6 dilutions and corresponding binding rates

4.3 Senescence alters Raman spectral fingerprints

As reported recently by Eberhardt et al. (2017), HDFs show different biological fingerprints in their Raman spectra depending on their cellular state. Based on this outcome, we aimed to confirm these results using different HDF donors in order to characterise cells and supernatants regarding their Raman spectra. As human fibroblasts mainly occur in quiescent stage and are growth arrested, distinguishing contact-inhibited from senescent cells in a non-invasive manner was our major scope.

4.3.1 Biochemical changes in HDFs

4.3.1.1 Single cell measurements

Based on scientific publications, we tried using CaF_2 and gold slides instead of ibidi® µ-Slides to avoid glass background for cell measurements. However, due to the insufficient objective working distance of our Raman microscope and the thickness of the CaF_2 slides, adjustment of the focal plane was not possible and all samples were measured in ibidi® µ-Slides with glass bottom.
Evaluation of single peaks of Raman measurements and intensities is demanding as the complex mixture of biochemical substances lead to an overlap of different spectra. Alternatively, multivariate analysis proved to be a powerful tool for evaluation of spectroscopic data.

We collected 15 spectra of quiescent and senescent cells of three different HDF donors in the fingerprint region from 400 – 1800 cm^{-1} and performed a multivariate PC analysis.
Each dot symbol in the scores plots (Figure 21 A, C, E) represents one measured cell nucleus.
Quiescent and senescent cells show different intracellular compositions resulting in specific Raman signatures. The scores plot enables a comparison between the spectra and reflects discrimination power based on the cellular state.

HDF76 (top panels) were treated with 200 nM Doxorubicin in PD 20. Although PC-1 explains 95% of the variability not all cell measurements were assigned correctly. However, a clear clustering based on the different measured cell stages cannot be observed.
PC-1 (explained variability: 87%) and PC-2 (explained variability: 6%) of HDF161 (induced senescence at PD 16) show clear variation of Raman spectral pattern between quiescent and senescent cells. Especially senescent nuclei measurements show high clustering.
The plot of PC-1 (explained variability: 82%) against PC-3 (explained variability: 2%) of quiescent and senescent HDF164 (PD 22) reveals also clear groupings although all measurements are mainly arranged to the right of the panel. This indicates that especially PC-3 has high discrimination power.

To get an overview on which Raman shifts cause the main spectral changes, we selected the relevant PCs of each donor for comparison and interpretation.
All the results of the loading plots were compared with literature in order to assign the differences in Raman peaks to the corresponding chemical bonds. Evaluation was done based on the peak assignment following Liendl, Grillari, & Schosserer (2019).
In all four HDF donors, almost the same spectral deviations occurred.

In our present study, Raman spectra from quiescent and senescent cells from all donors show different Raman patterns in the shifts corresponding to nucleic acids (NA) like RNA or DNA at 600-900 cm^{-1} (NA ring breathing modes) as well as to proteins and lipids.

Shifts in 1313 -1339 cm^{-1} refer to stretching of CH_2 and CH_3 groups and are a characteristic feature of lipids and glycoproteins.

Raman signatures specific for proteins including amide III, amide II and amide I regions arise from 1220–1300 cm^{-1}, 1480–1580 cm^{-1} and 1600–1800 cm^{-1} and seem to have a huge impact in terms of spectra classification.

Aromatic amino acids assign to 453 cm^{-1} (ring torsion of phenylalanine), 760-762 cm^{-1} (ring breathing tryptophan (proteins)) and 1174 cm^{-1} (C-H bending of tyrosine and phenylalanine) have significant structural features in senescent and quiescent samples.

At around 900 cm^{-1}, all loading plots show a clear peak, which could correspond to C-C stretching of proline and glucose or NA components.

Interestingly, the appearing alterations between 1652 and 1666 cm^{-1} are specific for unsaturated lipids (-*cis* and -*trans* isomers).

Table 12 shows an overview of the main bands having highest influence for discrimination of PCs, Figure 21 represents outcomes of HDF measurements.

Table 12 Raman shifts observed in HDF spectra having the most impact for discrimination between quiescent and senescent cells

Wavenumber/ cm^{-1}	Tentative peak assignment according to Liendl, Grillari, & Schosserer (2019)
453	Ring torsion of phenyl
481	DNA
505	C-OH_3 Methoxy group
618	C-C twisting (proteins)
760, 762	Ring breating tryptophan (proteins)
788	Ring breathing modes (nucleic acids)
600 – 900	NA ring breathing modes (proteins, lipids)
1119	C-C stretch
1128	C-N, C-O
1130	C-C
1131	Fatty acids
1156/7	C-C, C-N stretching (proteins)
1168	Tyrosine
1180 – 1185	Cytosine, guanine, adenine
1220 – 1300	Amide III region: C-N stretching, N-H bonding
1313	CH_3CH_2 twisting (lipids)
1327	CH_3CH_2 wagging (nucleic acids)
1339	CH_3CH_2 twisting (lipids), C-C stretch (phenyl)
1480 – 1580	Amide II region: C-N stretching, N-H bending, ring breathing modes (nucleic acids)
1652	C=C stretch (lipids)
1666	C=C stretch (proteins)
1600 – 1800	Amide I region: C=O stretching, C=C stretching (proteins, lipids)

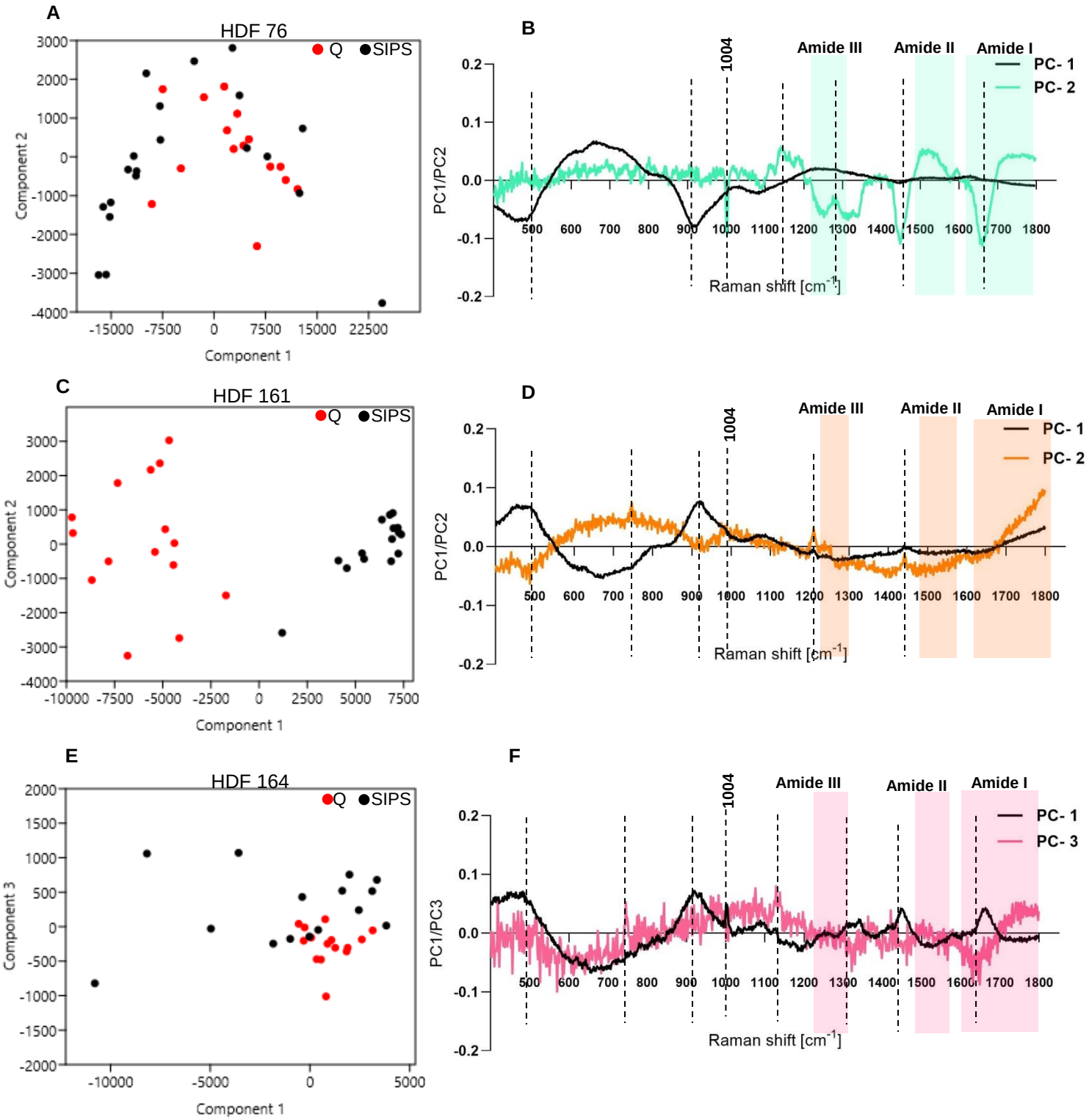

Figure 21 Principal Component Analysis of HDF cells of different donors. PCA scores plot comparing Raman spectra of quiescent and senescent cells (A, C, E) and corresponding PCA loadings exhibiting the spectral differences (B, D, F). Quiescent samples are represented in red, black dots indicate the senescent state. Loading plots of the two most discriminant components, along with the Q/SIPS separation are depicted in the scores plot.

To sum up, distinguishing spectra recorded from quiescent and senescent HDF analysed via PCA was a success. Spectral differences of cells caused by different chemical bonds were recognized and grouped.

4.3.1.2 Nanoparticle uptake in HeLa cells

The behaviour of nanoparticles in presence of cells changes referring to several characteristics like surface behaviour or shape. However, the effect and toxicity of nanoparticles on biological tissue are still not clear (Alkilany & Murphy, 2010). We tested, if it is possible to indicate an uptake in HeLa cells via Raman Microscope.

The addition of 150 nm gold particles to HeLa cells for uptake studies did not work successfully. Although the brightfield image (Figure 22) looks promising as it shows accumulation of nanoparticles around the nucleus, no significant enhancement of the Raman signal was observed. However, it is not possible to assess whether these particles are taken up or just present on the cell surface in a different focal plane.

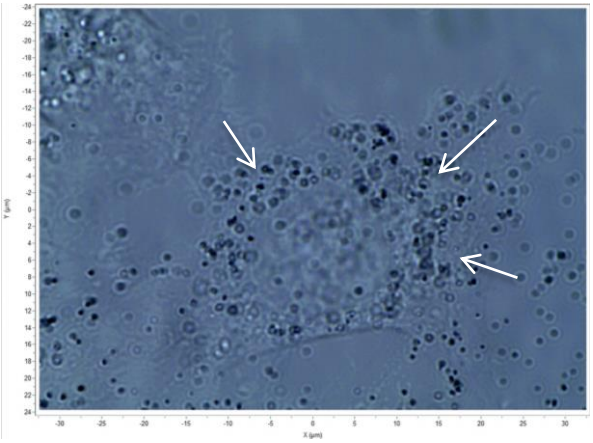

Figure 22 Uptake experiment. HeLa cells were treated with nanoparticles. 150 nm colloidal gold particles are mainly concentrated around the nucleus

4.3.2 Classification of senescence in supernatants

Next, we wanted to investigate if Raman Microspectroscopy is also suitable and promising for distinguishing supernatants from quiescent and senescent cells due to the differences in secretion.

Using SERS (described in methods section), we significantly enhanced the signal leading to spectra of high intensity and low background noise. Thereby enhanced spectra are shown in Figure 23.

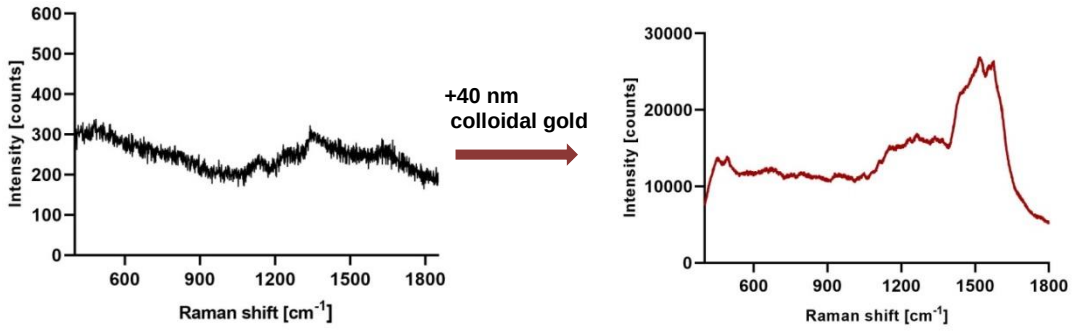

Figure 23 Signal enhancement using 40 nm gold particles. Acquired spectrum (400- 1800 cm^{-1}) of HDF supernatant shows signal increase of up to 1000 fold

PCA was performed for every donor after 30 measurements per condition. Outcomes are shown in Figure 24.

Supernatants of HDF76 show partial clustering. However, discrimination power of PC-1 (explained variability: 5%) and PC-2 (explained variability: 4%) are quite low.
The scatter plot of the PCA of HDF85 supernatants represents the clustering of quiescent and senescent samples. Although PC-2 and PC-3 account for just 9% in total (explained variability (PC-2): 5%; explained variability (PC-3): 4%) the scatter plot shows at least a tendency to cluster according to the different cellular stage.
The scatter plot of PC-4 (explained variability: 12%) and PC-5 (explained variability: 5%) of quiescent and senescent HDF161 supernatants shows unsuccessful grouping. The resulting cluster indicates no correlation referring to doxorubicin treated versus contact-inhibited samples.

The same outcome is shown in the scores plot of HDF164 supernatants. Samples are highly distributed and show no clustering according to the cellular state.

For a better understanding of the scatter plots, we had a look at the loadings to evaluate which spectral regions seem to be important for separation of the spectra.
Peaks related to NA show relevance in all donors and are depicted at 788 cm^{-1} (ring breathing modes). The bands at 481 cm^{-1} and 1327 cm^{-1} (CH_3CH_2 wagging) are also assigned to nucleic acids. Differences belonging to nucleosides (cytosine, guanine, adenine) are found from 1180 to 1185 cm^{-1}. Stretching and bonding of C-N or N-H indicate amide regions, ranging from 1220-1300 cm^{-1} (amide III), 1480-1580 cm^{-1} (amide II).
Bands at 1600-1800 cm^{-1} (amide I) are associated to protein and lipid structures (C=O and C=C stretching).
A shift of the Raman band at around 1100 cm^{-1} can be detected in all four donors and correspond to fatty acids.
An overview of all Raman regions relevant for discrimination between senescent and quiescent supernatants is shown in Table 13.

Table 13 Overview of main Raman shifts in quiescent and senescent supernatants and corresponding peak assignment

Wavenumber/ cm^{-1}	Tentative peak assignment according to Liendl, Grillari, & Schosserer (2019)
453	Ring torsion of phenyl
481	DNA
505	C-OH_3 Methoxy group
618	C-C twisting (proteins)
760, 762	Ring breating tryptophan (proteins)
1119	C-C stretch
1128	C-N, C-O
1130	C-C
1131	Fatty acids
1168	Tyrosine
1174	C-H bend (tyrosine, phenylalanine)
1180 – 1185	Cytosine, guanine, adenine
1220 – 1300	Amide III region: C-N stretching, N-H bonding
1313	CH_3CH_2 twisting (lipids)
1327	CH_3CH_2 wagging (nucleic acids)
1480 – 1580	Amide II region: C-N stretching, N-H bending, ring breathing modes (nucleic acids)
1600 – 1800	Amide I region: C=O stretching, C=C stretching (proteins, lipids)

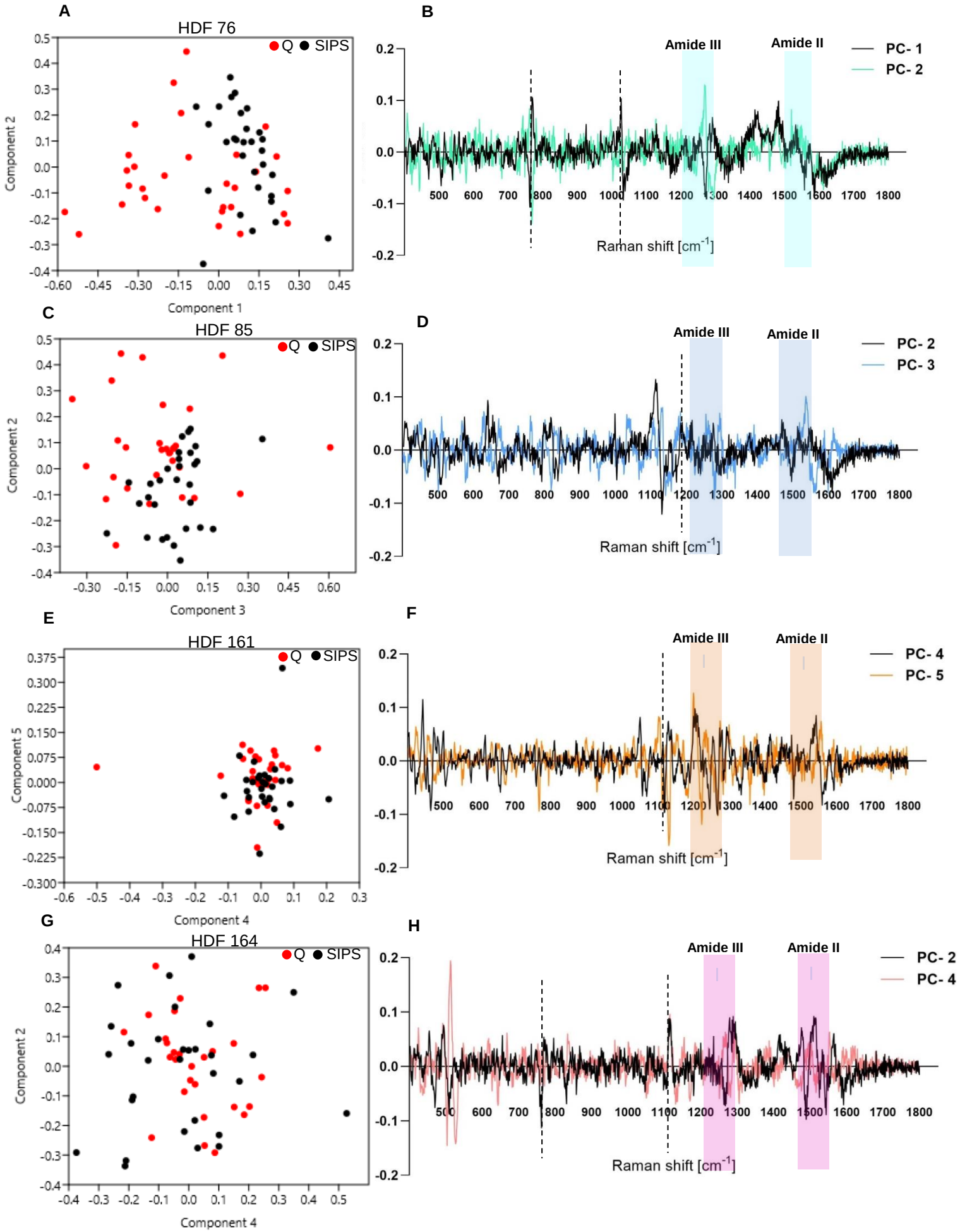

Figure 24 Resulting PCA after acquiring SERS spectra of HDF supernatants mixed with 40nm Au particles excited at 785 nm and the corresponding loading plots

To further evaluate the robustness of this model in other cell types, Raman spectra of supernatants from primary renal proximal tubule epithelial cells (RPTEC) were recorded and analysed. Measurements were again performed from 400-1800 cm^{-1} and before applying PCA, spectra were pre-processed by baseline correction and de-trending.

The result of the clustering is plotted in Figure 25. Although principal components show quite low correlation (explained variability (PC-3): 3%; explained variability (PC-4): 3%), the scatter plot nicely shows the clustering of quiescent and senescent supernatants.

Plotting loadings of PCs against the wavelength indicates correlations between PC-3 and PC-4. As previously discussed, amide I, II and III regions seem to have an impact on the distinction between senescent and quiescent. However, in this case no significant difference is observed in the amide I region.

The sharp peak at 1040 cm^{-1} could be assigned to CH_3CH_2 twisting (lipids) and C-C stretching (phenyl), which is also a typical signature for glycoproteins.

However, 930 to 1230 cm^{-1} is a known region for peaks resulting from proteins, lipids, glycogen, glucose and nucleic acids (Eberhardt, Matthäus, et al., 2017). The regions at 760-762 cm^{-1} as well as 545 cm^{-1} and 1174 cm^{-1} correspond to tryptophan. Major differences are observed in the amide III region from 1220-1300 cm^{-1}.

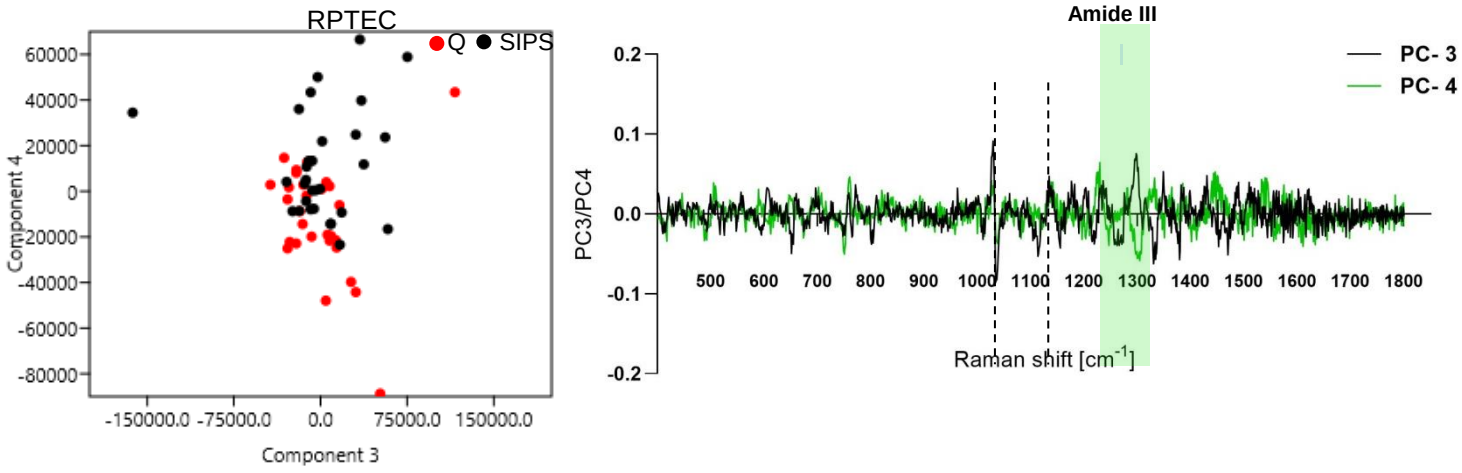

Figure 25 PCA of RPTEC supernatants with the corresponding loading plot showing main spectral differences

Additionally, we performed Raman measurements with skin equivalents produced by Regina Weinmüllner/ Adnan Becirovic.

Designing a 3D skin equivalent with keratinocytes and fibroblasts *in vitro,* and reconstructing aged and young tissue facilitates the understanding of important signalling processes and differentiation (Diekmann et al., 2016). However, inducing differentiation of the epidermis takes some time.

We measured supernatants from skin equivalents after 3 and 8 days of cultivation in differentiation media. The main aims here were discriminating on the one hand proliferating (young) from senescent (aged) samples and on the other hand, we wanted to find out if clustering according to the differentiation progress (time points 3 and 8) is possible.

PCA in Figure 26 nicely shows a successful clustering of senescent (black) and proliferating supernatants (orange) (explained variability (PC-1): 9%; explained variability (PC-2): 5%).

To check a time-dependent discrimination, a PCA according day 3 and day 8 was performed (explained variability (PC-3): 3%; explained variability (PC-4): 2%).

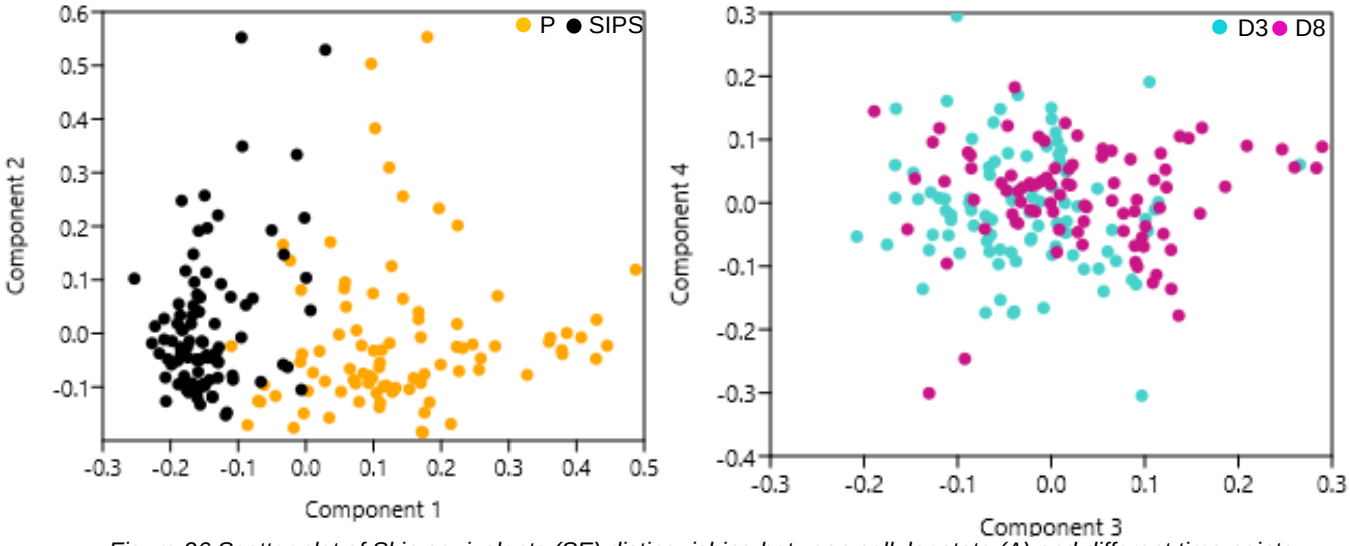

Figure 26 Scatter plot of Skin equivalents (SE) distinguishing between cellular state (A) and different time points of treatment (B)

After establishment of a set-up to receive and analyse usable Raman results we went one step further and tried to use Raman signatures to answer further scientific questions.

4.4 Implementation of Raman Microspectroscopy for answering further scientific questions

Due to a cooperation with the Medical University of Vienna, we tested other cell types addressing different scientific questions. One major aim was an identification of cancer samples compared to healthy, resistant or anti-cancer treated cells. This approach would enable a quick result, if and how a patient reacts to the cancer therapy.
Therefore we compared Raman spectra from cells treated with a specific compound with spectra from untreated cells followed by PCA.
Sample preparation was performed by the Medical University of Vienna.

4.4.1 Cells

In all scatter plots different samples are indicated abbreviated with 'T' for treated cells, 'C' for non-treated control cells and 'R' for resistant samples.

4.4.1.1 SW480 treated with Coti-2, Triapin and DpC

Adherent human colon adenocarcinoma cells (SW480) were treated with several substances like Triapin (3-aminopyridine-2-carboxaldehyde thiosemicarbazone), Coti-2 and DpC.
All those compounds belong to the group of α-N-Heterocyclic thiosemicarbazones (TSCs) and are known as promising anti-cancer compounds (Hager et al., 2018).
Ten cells per condition were measured using the 532 nm laser, 1800 gr mm^{-1} grating and 100 x oil objective.
Measurement and pre-processing were performed in the same way as for HDF. The scatter plot resulting from PC analysis is illustrated in Figure 27. High correlation of PC-1 (explained variability: 86 %) and PC-2 (explained variability: 7%) results in clear separation of the four different groups. DpC treated cells (green) show high distribution, while Triapin treated and control cells are clearly grouped. Component I apparently separates DpC treated samples from the others, component II divides Coti-2 cells from Triapin and control cells.

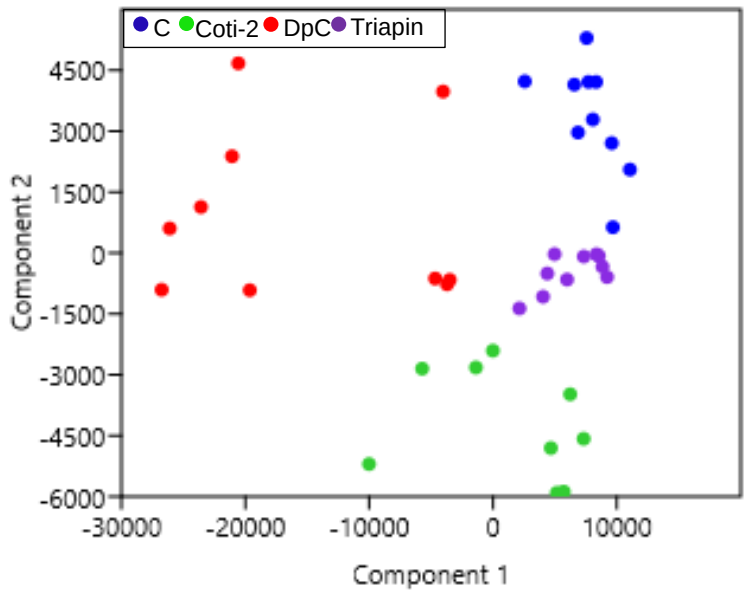

Figure 27 PCA of SW80 cells treated with Triapin, Coti-2 and DpC

Next, we analysed human pancreas adenocarcinoma cells (Capan), which were treated with another ruthenium-based anticancer compound KP1339 (Heffeter et al., 2013). Furthermore, KP1339 resistant Capan cells were measured and compared. Again, our goal was to distinguish between treated, non-treated (control) and resistant cells via Raman signatures and following PCA.

The result in Figure 28 nicely illustrates that PC-1 (explained variability: 9%) and PC-2 (explained variability: 8%) can clearly separate KP1339 treated Capan cells from the control as well as resistant cells.

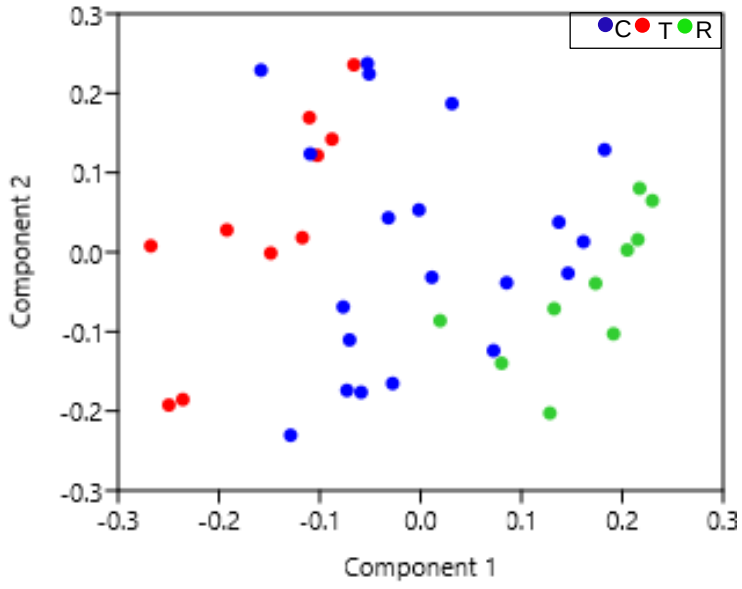

Figure 28 Scatter plot of Capan cells which were treated with KP1339 and compared to control samples and resistant cells (C= control; T=treated; R = resistant).

4.4.1.2 SW480 treated with CHS42

Next, we aimed distinguishing between control and SW480 cells that were treated with the anti-cancer activity compound thiosemicarbazone (Me2NNMe2).

10 spectra per condition were collected, and pre-processed by applying a baseline correction and de-trending (Figure 29).

PC analysis (explained variability (PC-1): 53%; explained variability (PC-2): 20%) shows a clear distinction between treated and non-treated cells. By linear discriminant analysis (LDA), we checked the capability of the classification, showing an accuracy of 100% (Figure 30).

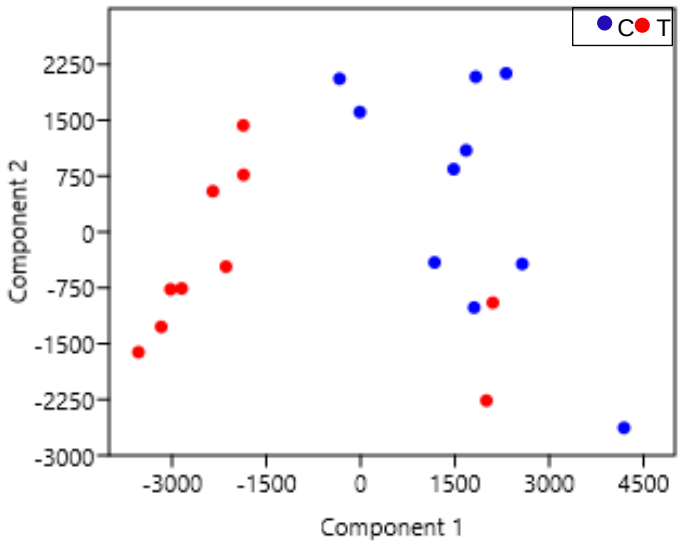

Figure 29 PCA of recorded Raman spectra classifies between SW480 cell treated with CHS42 compound and control

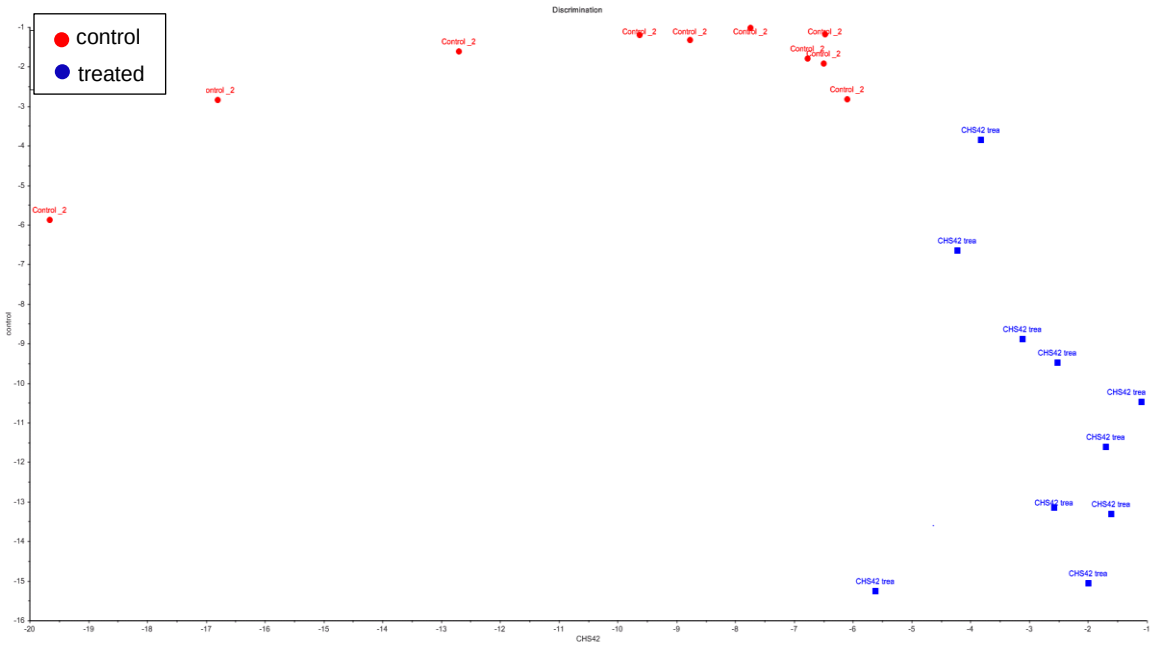

Figure 30 Linear discriminant analysis (LDA) of CHS42 treated cells and control (accuracy of the model: 100%; categories:2; method: linear model; projected: 4 components)

4.4.1.3 HCT116 treated with KP1339

Human colon carcinoma derived cells (HCT116) were also treated with KP1339. Additionally, a KP1339 resistant cell line was created and also compared to the non-resistant control.

The result of HCT116 cells is represented in Figure 31. Best separation is achieved by PC-1 (explained variability: 92%) and PC-3 (explained variability: 2%).

A successful grouping of control and treated samples is reached although a high distribution of data can be observed. Resistant samples are highly distributed and are found in both groups.

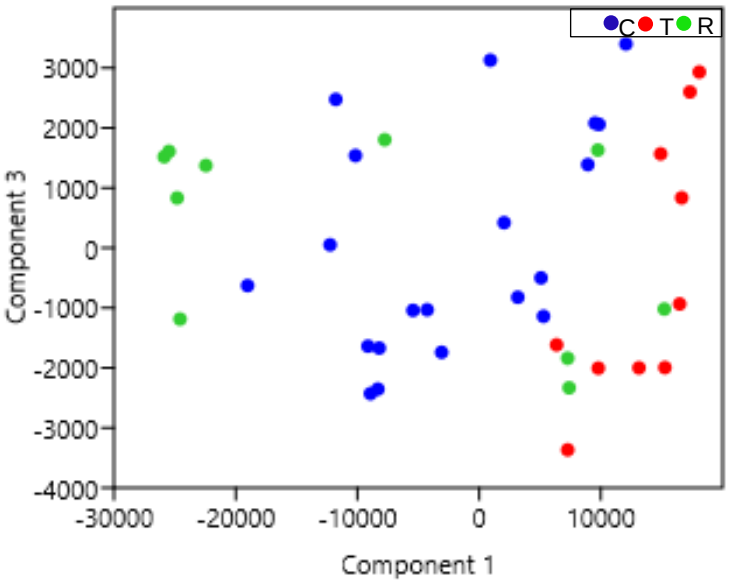

Figure 31 Scatter plot of KP1339 resistant HCT116 cells, cells treated with KP1339, and control

4.4.2 Supernatants

Of all evaluated cell samples provided by the Medical University of Vienna, also corresponding supernatants were measured according to the same procedure as described in section 3.5.3.

4.4.2.1 SW480 treated with Coti-2, Triapin and DpC

PCA was applied to discriminate between supernatants from treated cells and untreated ones (Figure 32). The resulting scatter plot indicates that Coti-2 can be easily separated from the control and Triapin treated samples. Still, clear grouping of all four types is not obtained. The correlations of PC-1 (explained variability: 18%) and PC-3 (explained variability: 5%) are quite low.

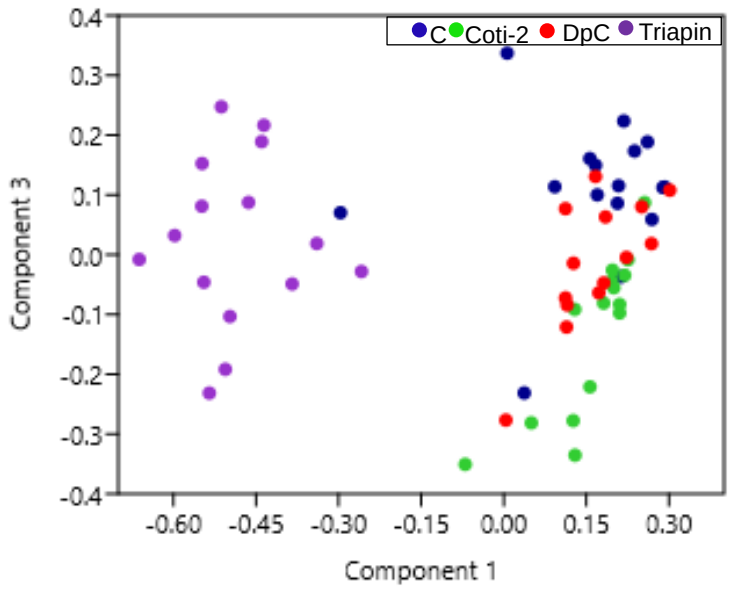

Figure 32 Scatter plot of measured supernatants of control SW480 cells, Coti-2, Triapin and DpC treated

4.4.2.2 Capan treated with KP1339

The result of measured Capan supernatants show a successful grouping of KP1339 treated samples and the control. Especially untreated supernatants cluster nicely, while treated ones show a higher distribution.

Classification of the Raman spectra is shown in Figure 33. Although PC-1 (explained variability: 10%) and PC-3 (explained variability: 6%) describe just 16 % of the variance, a clear discrimination is achieved.

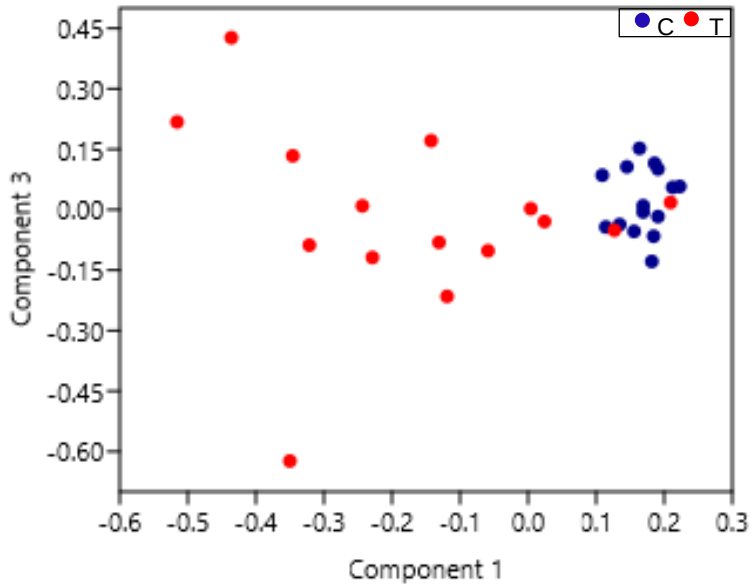

Figure 33 Scatter plot of measured supernatants of Capan control cells and KP1339 treated samples

Additionally, KP1339 resistant Capan cells were analysed and a clustering via PCA provided information about the separation power of this model. Apart from two outliers, supernatants from Capan wildtype and Capan resistant cells can be clearly classified by PC-1 (explained variability: 15%) and PC-2 (explained variability 7%) (Figure 34).

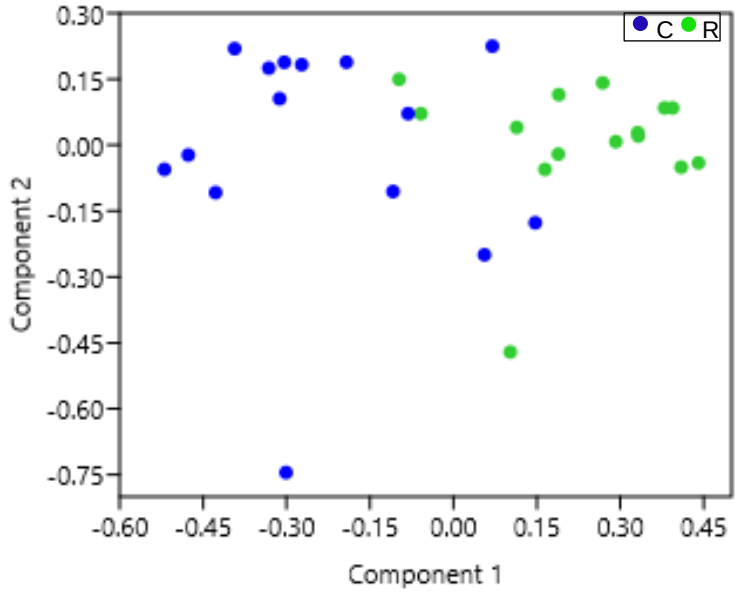

Figure 34 Scatter plot of supernatants of KP1339 resistant Capan cells vs. wildtype

An overall PCA of the two experiments demonstrates that the variability between two independent measurements is higher than discrimination between different cell treatments. Although both experiments show promising results when analysed separately, after mixing the outcomes PC-1 (explained variability: 12%) and PC-2 (explained variability: 5%) are not able to cluster correctly (Figure 35).

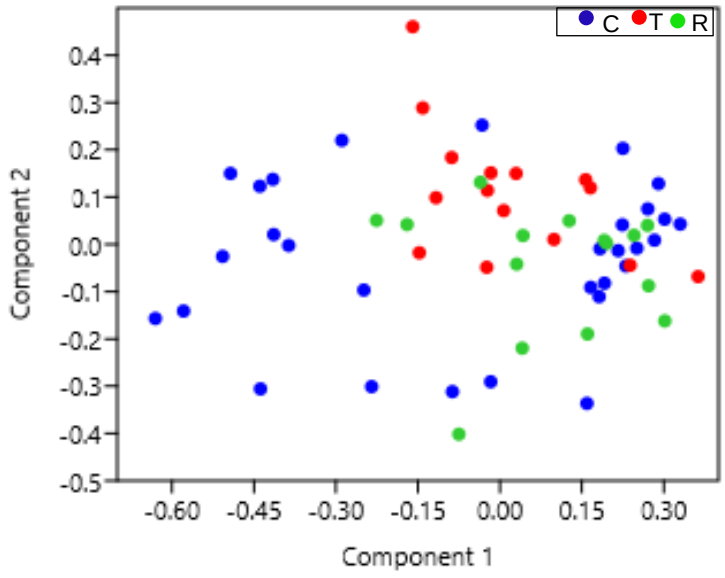

Figure 35 Scatter plot of supernatants of Capan control, Capan resistant and KP1339 treated samples

4.4.2.3 HCT116 treated with KP1339

Correlations of PC-1 (explained variability: 16%) and PC-2 (explained variability: 6%) of HCT116 supernatants are shown in Figure 36. This figure nicely illustrates the clear grouping of HCT116 treated samples and untreated ones.

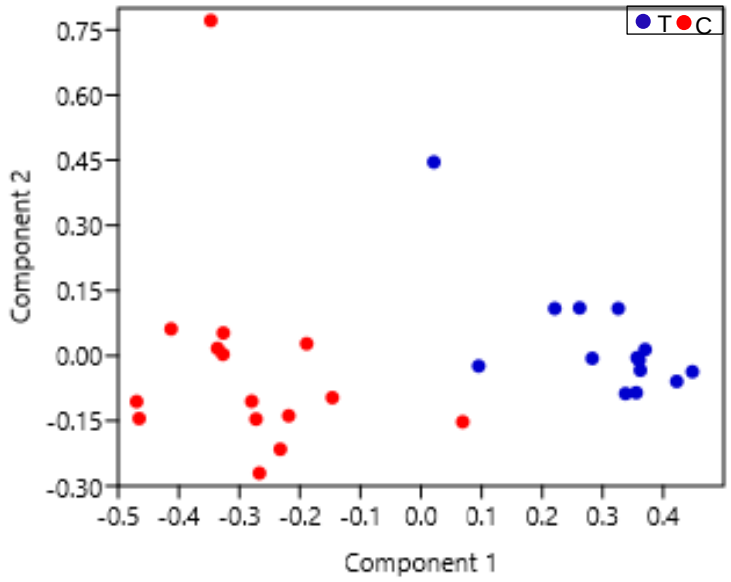

Figure 36 Scatter plot of HCT116 supernatants (KP1339 treated and control)

When looking at Figure 37, representing correlation of PC-1 (explained variability: 16%) and PC-2 (explained variability: 6%) of HCT116 resistant and wildtype supernatants, no successful separation of the two different samples is possible. Data are highly distributed and no discrimination between the Raman spectra of the samples can be observed.

Nevertheless, by combining both results in one scatter plot we observe a clustering of control samples. In addition, supernatants of KP1339 treated cells can be separated from resistant ones (Figure 38).

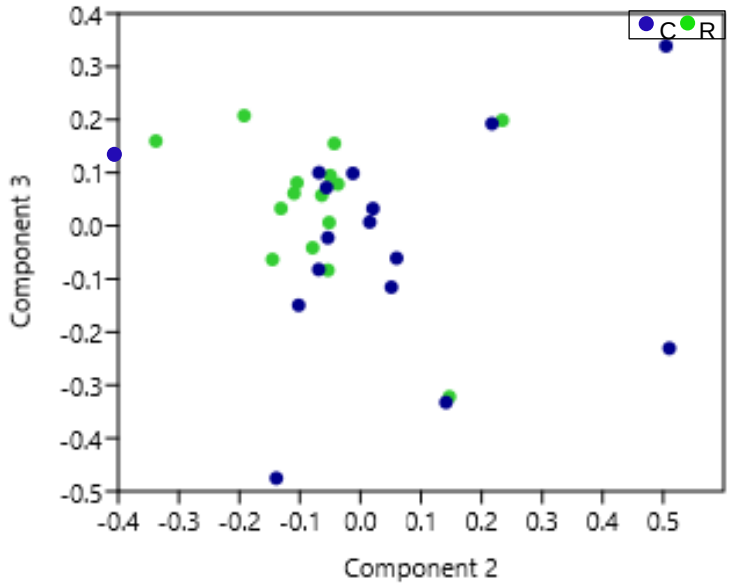

Figure 37 Scatter plot of HCT116 supernatants of resistant and control samples

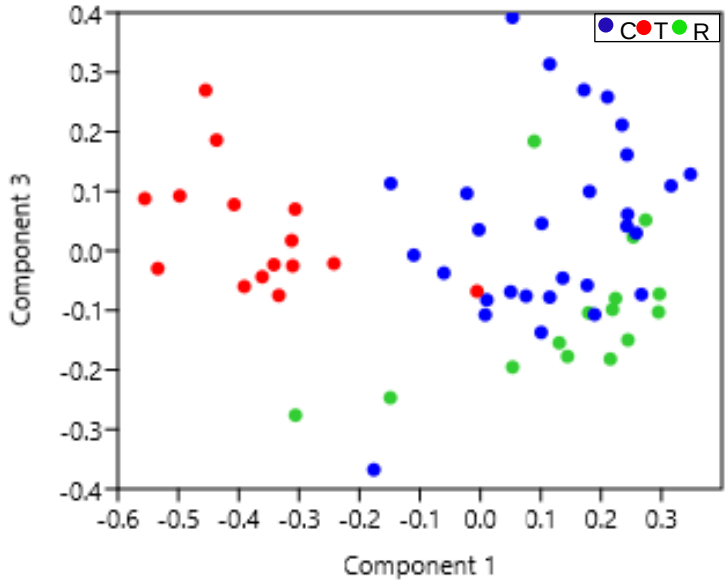

Figure 38 Scatter plot of HCT116 samples (control, KP1339 treated and HCT116 resistant)

4.4.3 Cell imaging

By the use of Raman mapping we are able to gain spectra of a whole area. Figure 39 shows a SW480 cell, which was treated with the compound Me2NNMe2 (CHS42).

Morphological changes due to the treatment resulted in occurrence of cytoplasmic vesicles. Via Raman Microscopy, we tried to gain insight into the structure of those vesicles compared to the rest of the cell. Additionally, we aimed to localise the compound in the cell. Firstly, a spectra of the raw compound CHS42 was acquired and afterwards fitted to the mapped area of the cell (Hager et al., 2018).

After pre-processing and PC analysis, the resulting loadings clearly distinguish three different regions based on the molecular structure, belonging to the background (PC-1: black), the nucleus (PC-2: green), and the vesicular structures (PC-3: red).

For further investigation of the compound localisation, we applied CLS-fitting, in order to get information about the location of the component within the cell. Based on the raw spectrum of the drug and its specific Raman signature, the compound seems to be located in the vesicles (Figure 39).

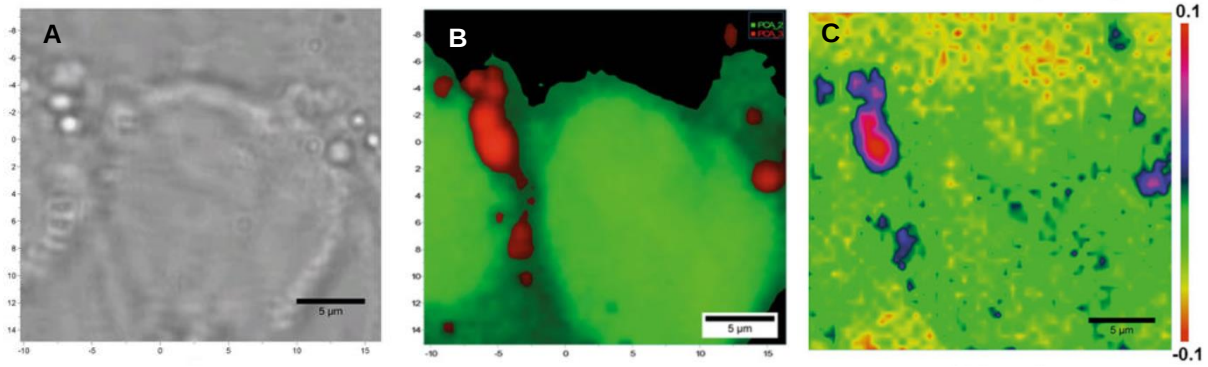

Figure 39 (A) Bright field image of the mapped area of 10 µM treated SW480 cell (B) False-colour image after PC analysis of the mapped discriminating nucleus (green), background (black) and vesicles (red) (C) CLS-fitting of the mapped area

All in all, Raman results are very promising and have substantial benefits regarding fast identification of cell stages and verifying certain treatments.

5 | DISCUSSION AND CONCLUDING REMARKS

In this part I will focus on analysis and interpretation of my experiments in context with already published literature.

Primarily, I will review if BLI and Raman Microspectroscopy are appropriate methodologies to identify senescence based on HDF cell and supernatant measurements.

5.1 Verification of senescent fibroblasts

Firstly, we successfully verified that the doxorubicin treated HDF164 are in pre-senescent state.

The performed senescence associated β-Galactosidase assay worked out fine as more than 95% out of the treated cells were clarified as β-Gal positive due to the blue coloured precipitate. This is caused by an increase in lysosomal β-Galactosidase activity at pH 6 (Severino, Allen, Balin, Balin, & Cristofalo, 2000).

Next, we analysed samples via BrdU- incorporation assay, which is also an indicator of senescence. The doxorubicin treated fraction clearly shows G2 growth arrest, which corresponds to literature (Campisi & D'Adda Di Fagagna, 2007).

However, flow cytometry results indicate a high amount of apoptotic cells. This result is consistent with our microscopic observations and concludes that the doxorubicin concentration was too high or the cells were already too stressed (as the apoptosis assay was performed in the 5^{th} week of recovery after doxorubicin treatment). When looking at the qPCR results, we observed increased mRNA levels of IL-8, IL-1, nml1, CCL-2 and p21 in comparison with the quiescent fractions. These positive results clearly confirm the altered behaviour of doxorubicin treated cells, indicating that those became senescent. Lastly, a Luminex® multiplex assay confirmed the higher secretion of IL-8 in the supernatant of treated cells in comparison with quiescent ones.

To sum up, all the performed biochemical assays, based on different biological processes strengthen the fact that (1) treating HDF cells with 100 nM doxorubicin (as described in the methods section) leads to a switch from proliferating to senescent state and (2) the characterised cells, which are the fundament for the rest of our experiments are indeed senescent based on current published scientific literature.

Furthermore, we justified the treatment with doxorubicin (following the same procedure) of all different cells we performed experiments with, in order to investigate a method enabling a faster and specific identification of cellular senescent HDFs.

5.2 Establishment of a biosensor based set up for specific measurement of IL-8

When cells become senescent, they secrete more IL-8 (Scott et al., 2009) compared to quiescent cells. Taking advantage of this alteration in senescent cells unlike contact inhibited ones, we aimed to discriminate them based on a specific measurement of IL-8.
We successfully established an IL-8 quantification method using BLI. The strategy relies on an assy design similar to sandwich ELISA including acquiring binding kinetics in a time efficient manner and under material-saving parameters (appropriate antibody dilutions, measurement time). Additionally, we wanted to create a robust assay, which guarantees specific binding of our target.

The approach and all tested assay parameters can be further used for screening IL-8 in all kind of microfluids but could also be adapted for other biomarkers.
For binding IL-8 in a sandwich form, two antibodies having different epitopes had to be found. Due to small size of IL-8 this was quite challenging and demanded testing of various antibodies in different settings. In order to gain high binding rates, we used the HRP chromogenic substrate DAB (like in ELISA kits).
Normally, for kinetic measurements a four-parameter fit or five-parameter dose response curve fits best (Carvalho et al., 2017, 2018; Wallner et al., 2013; Yang et al., 2005). However, in this case a linear regression model fits at least equally well, which is quite uncharacteristic and needs to be further proven.
The resulting bindings of supernatant measurements and the following normalisation to the average cell numbers depending on the state show increased IL-8 levels in all measured donors.
This result (1) confirms senescence of our doxorubicin treated cells and (2) clearly states that the method per se as well as the established assay is suitable for our research question.
Though, all samples were just measured in technical duplicates. Measurements must definitely be repeated using different biological replicates in order to confirm the gained results.
One possibility for evaluation and confirming of resulting concentrations is analysing the same samples with a conventional sandwich ELISA assay.

To our knowledge, this is the first BLI based assay for a specific measurement of picomolar IL-8 levels. Conclusively, beside further proof of recorded outcomes this assay can be extended to different cell types.
After performance of further prospective studies, a faster measurement of different protein concentrations will be possible in near future.

5.3 Characterisation of senescence based on Raman signatures

Recorded preliminary data of different HDF donors emphasize the suitability and power of Raman microspectroscopy to discriminate between senescent and quiescent samples.
Proper pre-processing of the recorded Raman spectra and evaluation via multivariate statistics resulted in clear and illustrative outcomes. All Raman spectra were recorded from 400 to 1800 cm^{-1} as this is the region of the biological fingerprint.
Senescent differences, expressed in Raman shifts, were assigned to the main cell compartments like proteins, lipids and nucleic acids (Eberhardt et al., 2017).

5.3.1 HDF cells

In our experiments, PCA of HDF161 shows a clear distinction of senescent and quiescent cells, while in HDF76 and HDF164 at least strong tendencies regarding correct classifications can be observed.
However, further biological replicates have to be recorded to ensure the gained outcome.
When having a look at the loading plots which indicate the major differences, senescence seems to change the Raman signature over the whole fingerprint region, like nucleic-acid related peaks, which arose from 600- 900 cm^{-1} and are dominant in all cell donors as well as 481 cm^{-1} which is specific assigned to DNA.
The clear peak ~900 cm^{-1} could be due to ring breathing in tyrosine and proline (protein) (855 cm^{-1}) or just be a contamination of formaldehyde which was used to fix the cells (907 cm^{-1}).
Distinct peaks between 1652 cm^{-1} and 1666 cm^{-1}, specific for unsaturated lipids (*-cis* and *-trans* isomers) exactly correspond to Marianis publication (2010), who reported that the prevalent *–cis* confirmation in senescent cells is due to the decreased stability of the nuclear envelope.
Shifts in 1313 -1339 cm^{-1} belong to the stretching of CH_2 and CH_3 groups and are characteristic features of lipids and glycoproteins.
Peaks from 1652 to 1666 cm^{-1} corresponding to changes in proteins and lipids of senescent cells is also consistent to literature (Eberhardt, Beleites, et al., 2017; Liendl et al., 2019; Mariani et al., 2010).

Generally spoken, percentages of the single PC in the loadings plot vary from 3% up to almost 90%. As cells are complex biological systems, we expect high variability between each cell. Thus, the focus is not so much on the % of the variabilities, but on the discrimination power of the PCs.

Overall, we confirmed that our doxorubicin treated cells can be separated from quiescent ones due to the differences in Raman signature. Briefly, the nucleic acid content as well as protein and lipid signatures significantly alter when cells became senescent.
All those gained results are also consistent with previous results like change in mRNA levels as well as cell cycle growth arrest.

5.3.2 HDF supernatants

We managed to record high quality spectra of supernatants from HDFs due to the addition of 40 nm gold particles. Measurements of supernatants with 40 nm silver as well as 150 nm gold particles also showed an increase in signal but not to the same extent.
Due to fluorescence of phenol red, which was contained in the cultivation media, and the greater enhancement, samples were analysed using the 785 nm excitation laser.
Results were promising but definitely not as much as the cell measurements. PCAs show just low classification power in all measured donors. Thus, the loadings are not as conclusive as for the cells.
Nevertheless, also in supernatants especially the amide II/III regions, corresponding to a change in protein level, seem to have significant impact. A distinct peak at 1148 cm^{-1}, corresponding to C-H binding, is present in all donors except HDF76. A change in protein levels can be observed, as for example in the phenylalanine peak (1004 cm^{-1}). C-C stretch differences are assigned to lipids at 1119 cm^{-1} Raman shift.

PCA of RPTEC supernatants shows at least a slight separation of quiescent and senescent samples, mainly due to Raman shift differences in the amide III regions. However, when repeating this experiment, the PCA of acquired Raman spectra did not show any separation of groups (data not shown). One possible reason could be the high amount of apoptotic cells in the first experiment, meaning that in the demonstrated PCA we probably differentiate apoptotic from quiescent cell supernatants.

Measurements of supernatants from skin equivalents show clear differences between senescent and proliferating samples. The results also indicate alterations in secretion level between day 3 and day 8 after treatment with differentiation medium.

By using SERS, it was possible to significantly enhance the intensities of recorded spectra. Another idea for gaining an even higher resolution is a filter-based approach. Studies already demonstrated the higher intensity compared to colloidal particles of measurement. Trace elements can be detected by preparing a SERS active substrate (silver nanoparticles) using a filter membrane (Yu, Wei W. White, 2012).
Loading gold nanoparticles on a filter paper is also reported by Zheng and co-authors (2012). Their approach was to observe a biochemical reaction in real-time by inducing catalysis, enabling a record of a time-dependent SERS spectrum.
However, our performed preliminary experiments with filter paper did not show any signal enhancement (data not shown), but many factors could be further optimized and this might then also represent a promising strategy to analyse Raman signatures of cell supernatants.

Additionally, a quantitative analysis is rather difficult as the intensity of the Raman signal correlates with the amount of a certain molecule in the supernatants (Eberhardt, Beleites, et al., 2017). Although the same volume was taken for all the measurements (15 µL) under the same conditions, transition

into senescence can cause differences between the treated cells. This is mentioned in detail by Eberhardt and co-workers (2017). One possibility to gain quantitative information of single molecules would be for example a following mass spectrometry (MS) analysis (Köhler et al., 2009).
A further approach would be to consider the ratio of two distinct peaks in order to gain a more predictive result.

To sum up, Raman Microspectroscopy is a method of high potential for monitoring differences based on molecular level. It was confirmed by several studies that cancerous or apoptotic cells can be clearly distinguished from proliferating or quiescent ones due to their specific Raman signature (Brauchle et al., 2014; Li et al., 2002). In course of my master thesis, we confirmed that Raman signatures from senescent cells differ from quiescent ones, especially in their protein, nuclear and lipid structure (Bai et al., 2015; Eberhardt, Beleites, et al., 2017). Even differences in the secretion levels could be obtained with this method by recording Raman spectra of supernatants via SERS. Although optimisation and further measurements are necessary, preliminary data are highly promising. An intended goal with this technique is to detect even different fibroblast subpopulations.

Furthermore, we built up a training-set of all measured supernatants to enable a determination of the cellular state of unknown samples (test-set) using PCA-LDA (data not shown). This approach was not successful, as our recorded data were not sufficient to set-up a valid classification model. However, a future approach would be the establishment of an accurate model using more data for the training set to allow a valid classification of ‘unknown’ samples.

5.3.3 Implementation of Raman Microspectroscopy for answering further scientific questions

5.3.3.1 Cells

Using the established same Raman set-up, we measured SW480, HCT116 and Capan cells, which were treated with several different compounds and successfully discriminated them from the untreated ones.
Interestingly, also for these samples we observed a better classification in cells than in supernatants (similar to HDFs). All three treatments of SW480 cells can be distinguished from each other. The same holds true for the Capan and HCT116 cells. As we analysed just one biological replicate of all different cells, we cannot exclude that these measurements were subject to day or well variabilities.

These outcomes clearly strengthen (1) that Raman Microspectroscopy is a suitable method for this scientific problem and (2) the robustness of our chosen set-up, (3) the high sensitivity of this method.

Additionally, via another multivariate statistic tool, namely the linear discriminant analysis (LDA), we tested the separability and the classification power of our data. 100% accuracy was achieved.
The next step would be the recording of spectra from ‘unknown’ samples and further testing, if the LDA model can classify the cell states based on these previous results.

By mapping one CHS2 treated SW480 cell, we confirmed the different composition of cell compartments. The nucleus and surrounding vesicles as well as the background could be clearly separated from each other via PCA. Finding the component CHS42 via CLS-fitting within the cell poses a huge chance regarding future diagnostic applications, although the result has to be interpreted with great care and should be further proofed and reproduced.

5.3.3.2 Supernatants

From the same samples mentioned above, supernatants were classified based on Raman signature.
When looking at the different treated SW480 cells, it is clearly demonstrated that cell measurements worked better than analysis of supernatants. Of the different treatments of SW480 cells, only the Coti-2 treated ones are clearly grouped. However, we also observed a high day-to-day variability of Capan samples.
After a separate analysis of supernatants of resistant and treated cells, a successful clustering of the untreated ones is observed. When performing an overall PCA, no clear distinction is achieved. This indicates that in this case the technical variability is higher than the biological one. The same phenomenon is monitored for the HCT116 samples.

To conclude, senescent cells can be identified due to spectral differences based on their unique Raman signature. Measurements of supernatants show at that time no clear distinction, but are very promising.
Further studies should confirm, whether these results are reproducible and demonstrate the same important regions in the loading plots to be responsible for the differences. Upcoming cell type variabilities as well as the fact that all these experiments are *in vitro* should be considered. Additional evaluation of all gained outcomes using multivariate statistics is recommended.
Finally, by using this label-free method, it is possible to gain biological information on a molecular basis in a fast manner. Therefore, we think that Raman Microspectroscopy is a suitable and promising method for our scientific issue.

This project was supported by Grillari Labs, EQ-BOKU VIBT GmbH and the BOKU Core Facility Biomolecular & Cellular Analysis.

6 | MATERIAL

Reagent/Resource	Source
Disposables	
Pipette, Cellstar®, serological (2 mL, 5 mL, 10 mL, 25 mL, 50 mL)	Greiner Bio-one, Kremsmünster
Pipette tips (1000 µL, 200 µL)	Greiner Bio-one, Kremsmünster
Pipette tips (10 µL)Starlab,	Hamburg (D)
Roux flasks (25 cm^2, 75 cm^2 and 175 cm^2)	Greiner Bio-one, Kremsmünster
6-well plates	Nunclon Delta SurfaceThermo Scientific, Waltham (USA
Nunc F96 MicroWellTM Plates	Thermo Fisher Scientific, Langenselbold, (D)
IBIDI µ-Slide (8 well and 4 well plate)	IBIDI Martinsried (D)
Micro tubes, (1.5 mL, 2.0 mL), steril	Sarsted, Nürnbrecht (D)
CryoTube vials	Thermo Scientific, Waltham (USA)
Centrifuge tubes, Cellstar® (15 mL, 50 mL)	Greiner Bio-one, Kremsmünster
PCR tubes, 8-tube strips, 0.2 mL	Biozym, Wien
RNase Zap wipes	Ambion, Carlsbad (USA)
Laboratory equipment	
Research Plus pipettes 100-1000 µL 20-200 µL 2-20 µL 0.5-10 µL 0.1 –2 µL	Eppendorf, Hamburg (D)
Pipetman pipettes 2 –200 µL 100-1000 µL 20-200 µL 10-100 µL 2-20 µL	Gilson, Middleton (USA)
Laminar hood (HBB 2448 Lamin Air)	Holten, Hanau (D)
Incubator Heracell 150i CO2	Thermo Scientific, Waltham (USA)
Incubator Heraeus BBD 6220	Heraeus, Hanau (D)
Centrifuge 5415 R Centrifuge 5810 R Centrifuge 5804 R	Eppendorf, Hamburg (D)
Centifuge Rotanta 460 R	Hettich, Tuttlingen(D)
Centrifuge Avanti J-20 XP	Beckman Coulter, Brea (USA)

Microscope CK2	Olympus, Shinjuku (J)
Microscope DFC 425 C	Leica, Wetzlar (D)
Biosensor tips	Forte Bio
Cell counter Vi-Cell® XR	Beckman Coulter, Brea (USA)
Rotor-Gene-Q	Qiagen, Venlo (NL)
Thermomixer comfort	Eppendorf, Hamburg (D)
PCR T3 Thermocycler	Biometra, Göttingen (D)
Spectroscope Nanodrop1000 UV/VIS	Thermo Scientific
Odyseey Infrared Imager	Li-Cor, Lincoln (USA)
Vortex Mixer (VF2)	IKA, Staufen (D)
pH meter (521)	WTW, Weilheim (D)
Electrophoresis power supply EPS600	Pharmacia, Uppsala (S)
Water bath	GFL, Bergwedel (D)
XploRA^{TM}Raman microscope	Horiba
Octet Red96e	ForteBio, Menlo Park, CA (USA)
Miscellaneous	
Ethanol (disinfection agent)	Australco, Spillern
Ethanol	Merck, Darmstadt (D)
Isopropanol	Merck, Darmstadt (D)
TriReagent®	Sigma-Aldrich, St. Louis (USA)
FCS	Sigma-Aldrich, St. Louis (USA)
Nuclease free water	Gibco, Carlsbad (USA)
PBS	Merck, Darmstadt (D)
Glycerol	Merck, Darmstadt (D)
5x Hot FirePol EvaGreen® qPCR Mix Plus	Medibena, Wien
Trypan Blue (ViCell®)	Sigma-Aldrich, St. Louis (USA)
L-Glutamine (G7513)	Sigma Aldrich, St. Louis (USA)
7X® detergent	VWR (ICNA097667093)
Glacial acetic acid	Merck, Darmstadt (D)
Chemicals& Kits*	
LYNX lyophilized HRP kit (LNK002P)	BioRad, Hercules (USA)
GOTAQ Polymerase kit	M300 Promega
Doxorubicin	Sigma Aldrich (Cat# D1515-10MG, Lot SLBH4977V)
Phosphatase inhibitor (PhosSTOP)	Sigma Aldrich
Protease inhibitor	Sigma Aldrich
Staurosporin	Sigma Aldrich
40 nm colloidal silver particles	BBI Solutions (cat. no. EM. SC40)
40 nm colloidal gold particles	BBI Solutions (cat. no. EM. GC40)

150 nm colloidal gold particles	BBI Solutions (cat.no.EM.GC150)
Pacific Blue™ Annexin V (100 tests)	Biolegend
*Main used chemicals are listed, further base chemicals were provided by AppliChem (Darmstadt, D), Carl Roth (Karlsruhe, D), Merck (Darmstadt, D) and VWR (Darmstadt, D).	

Antibodies		
Target	**Manufacturer**	**Catalogue#**
IL-8 antibody (3IL8-H10)	Thermo Fisher Scientific	M801
IL-8 monoclonal antibody, biotin (I8S2)	Thermo Fisher Scientific	M802 B
IL-8 antibody (C-11)	Santa Cruz (Szabo Scandic)	sc-376750
IL-8 antibody (B-2)	Santa Cruz (Szabo Scandic)	sc-8427
anti-human IL-8	BD Pharmingen	554716
Biotin Monoclonal Antibody (Z021), HRP	Thermo Fisher Scientific	03-3720
Propidiumiodide	Sigma-Aldrich	P1607
Anti-mouse FITC antibody	Sigma Aldrich	F8264
Anti-BrdU antibody	BD Biosciences	347580

Primers	
Target	**Sequence (forward & reverse)**
GAPDH	TGTGAGGAGGGGAGATTCAG CGACCACTTTGTCAAGCTCA
Interleukin-6	TGTTTTCTGCCAGTGCCTCT CCAGTACCCCCAGGAGAAGA
Interleukin -8	CTCTTGGCAGCCTTCCTGATTT ACAGAGCTCTCTTCCATCAGA
CXCL-1	TCAATCCTGCATCCCCCATAG CAGGAACAGCCACCAGTGAG
p21	GGCGGCAGACCAGCATGACAGATT GCAGGGGGCGGCCAGGGTAT
CCL-2	CCTTCATTCCCCAAGGGCTC GGTTTGCTTGTCCAGGTGGT
NSUN 5	CTTCCAGCCTCGATGACTTA CCCTGTCCTGCAGAATGAG
ACTB	TAGCACAGCCTGGATAGCAA ACTGGGACGACATGGAGAAA
B2M	GAGATGTCTCGCTCCGTGG TACATGTCTCGATCCCACTTAAC

NML	ATGTGGCCAAGAGCTGGCGG CGAAGAGCCTGAGTGGGCCG
Fibrillarin	ATGCTCGACACCCACACAAA CCTCCATTACGCAGGAAGGT
Buffers	
10x PBS	17.6 mM KH2PO4, 59.6 mM Na2HPO4 x2 H20, 26.8 mM KCl, 1.37 M NaCl adjusted to pH 6.5
PBS-T	0.1% (v/v) Tween 20 in PBS
Blocking solution	1% (w/v) dry milk powder in PBST
Trypsin	0.1% (v/v) Trypsin, 0.02%(w/v) EDTA
K- buffer	0.1 %BSA, 0.05% Tween, 1xPBS
2 % Agarose Gel in TAE (for 1Gels)	2.8 g Agarose, 2.8 mL TAE Buffer (50x), fill with RO-H2O to 140 mL
50x TAE Buffer	242 g Tris Base, 57.1 mL Acetic Acid, 100 mL EDTA 0.5 mM pH 8, add RO-H2O to 1000 mL

7 | REFERENCES

Abdiche, Y. N., Lindquist, K. C., Pinkerton, A., Pons, J., & Rajpal, A. (2011). Expanding the ProteOn XPR36 biosensor into a 36-ligand array expedites protein interaction analysis Ligand strips Ligand spots. *Analytical Biochemistry*, *411*(1), 139–151. https://doi.org/10.1016/j.ab.2010.12.020

Akkus, O., Polyakova-akkus, A., Adar, F., & Schaffler, M. B. (2003). Aging of Microstructural Compartments in Human Compact Bone.

Alkilany, A. M., & Murphy, C. J. (2010). Toxicity and cellular uptake of gold nanoparticles: What we have learned so far? *Journal of Nanoparticle Research*, *12*(7), 2313–2333. https://doi.org/10.1007/s11051-010-9911-8

Ametrano, F. M. (2016). About Bitcoin And Blockchain : A Cultural Paradigm Shift, *9*, 1–9. https://doi.org/10.1186/1471-2199-7-33

Arciniega, M., & Torres-larios, A. (2019). A screening platform to monitor RNA processing and protein-RNA interactions in ribonuclease P uncovers a small molecule inhibitor, 1–14. https://doi.org/10.1093/nar/gkz285

Bai, H., Li, H., Han, Z., Zhang, C., Zhao, J., Miao, C., … Han, Z. (2015). Label-free assessment of replicative senescence in mesenchymal stem cells by Raman microspectroscopy. *Biomedical Optics Express*, *6*(11), 4493. https://doi.org/10.1364/boe.6.004493

Bloch, Y., Bouchareychas, L., Merceron, R., Dullaers, M., Adamopoulos, I. E., Savvides, S. N., … Bossche, L. Van Den. (2018). Structural Activation of Pro-inflammatory Human Cytokine IL-23 by Cognate IL-23 Receptor Enables Recruitment of the Shared Receptor IL-12R b 1 Article Structural Activation of Pro-inflammatory Human Cytokine IL-23 by Cognate IL-23 Receptor Enables Recruit, 45–58. https://doi.org/10.1016/j.immuni.2017.12.008

Bohorfoush A.G. (1996). Tissue Spectrosocpy for Gastrointestinal Diseases. *Spine (Phila Pa 1976)*, *21*, 2640–2650. Retrieved from http://repository.upi.edu/1360/1/s_d5451_0604180_chapter1.pdf

Bonifacio, A., Marta, S. D., Spizzo, R., Cervo, S., Steffan, A., & Colombatti, A. (2014). Surface-enhanced Raman spectroscopy of blood plasma and serum using Ag and Au nanoparticles : a systematic study, 2355–2365. https://doi.org/10.1007/s00216-014-7622-1

Brauchle, E., Thude, S., Brucker, S. Y., & Schenke-Layland, K. (2014). Cell death stages in single apoptotic and necrotic cells monitored by Raman microspectroscopy. *Scientific Reports*, *4*(April). https://doi.org/10.1038/srep04698

Butler, H. J., Ashton, L., Bird, B., Cinque, G., Curtis, K., Dorney, J., … Martin, F. L. (2016). Using Raman spectroscopy to characterize biological materials. *Nature Protocols*, *11*(4), 664–687. https://doi.org/10.1038/nprot.2016.036

Campisi, J., & D'Adda Di Fagagna, F. (2007). Cellular senescence: When bad things happen to good

cells. *Nature Reviews Molecular Cell Biology*, *8*(9), 729–740. https://doi.org/10.1038/nrm2233

Carvalho, S. B., Moleirinho, M. G., Wheatley, D., Welsh, J., Gantier, R., Alves, P. M., … Carrondo, M. J. T. (2017). Universal label-free in-process quantification of influenza virus-like particles. https://doi.org/10.1002/biot.201700031

Carvalho, S. B., Moreira, A. S., Gomes, J., Carrondo, M. J. T., Thornton, D. J., Alves, P. M., … Peixoto, C. (2018). A detection and quantification label-free tool to speed up downstream processing of model mucins, 1–14.

Chivers, C. E., Koner, A. L., Lowe, E. D., & Howarth, M. (2011). How the biotin – streptavidin interaction was made even stronger : investigation via crystallography and a chimaeric tetramer, *63*, 55–63. https://doi.org/10.1042/BJ20101593

Collado, M., Blasco, M. A., & Serrano, M. (2007). Cellular Senescence in Cancer and Aging. *Cell*, *130*(2), 223–233. https://doi.org/10.1016/j.cell.2007.07.003

Diekmann, J., Alili, L., Scholz, O., Giesen, M., Holtkötter, O., & Brenneisen, P. (2016). A three-dimensional skin equivalent reflecting some aspects of in vivo aged skin. *Experimental Dermatology*, *25*(1), 56–61. https://doi.org/10.1111/exd.12866

Do, T., Ho, F., Heidecker, B., Witte, K., Chang, L., & Lerner, L. (2008). A rapid method for determining dynamic binding capacity of resins for the purification of proteins, *60*, 147–150. https://doi.org/10.1016/j.pep.2008.04.009

Eberhardt, K., Beleites, C., Marthandan, S., Matthäus, C., Diekmann, S., & Popp, J. (2017). Raman and Infrared Spectroscopy Distinguishing Replicative Senescent from Proliferating Primary Human Fibroblast Cells by Detecting Spectral Differences Mainly Due to Biomolecular Alterations. *Analytical Chemistry*, *89*(5), 2937–2947. https://doi.org/10.1021/acs.analchem.6b04264

Eberhardt, K., Matthäus, C., Winter, D., Wiegand, C., Hipler, U., Diekmann, S., & Popp, J. (2017). Raman and infrared spectroscopy differentiate senescent from proliferating cells in a human dermal fibroblast 3D skin model. *The Analyst*, *142*(23), 4405–4414. https://doi.org/10.1039/c7an00592j

Estep, P., Reid, F., Nauman, C., Liu, Y., Sun, T., Sun, J., & Xu, Y. (2013). High throughput solution-based measurement of antibody-antigen affinity and epitope binning, *5*(2), 270–278.

Fernandes, I., Russo, F., & Braga, P. B. (2014). Fibroblast sources : Where can we get them ? Fibroblast sources : Where can we get them ?, (July). https://doi.org/10.1007/s10616-014-9771-7

Fleischmann, M. (1974). RAMAN SPECTRA OF PYRIDZNE ADSORBED AT A SILVER ELECTRODE, *26*(2), 2–5.

Gao, S., Zheng, X., & Wu, J. (2017). Sensors and Actuators B : Chemical A biolayer interferometry-

based competitive biosensor for rapid and sensitive detection of saxitoxin. *Sensors & Actuators: B. Chemical*, *246*, 169–174. https://doi.org/10.1016/j.snb.2017.02.078

Gewirtz, D. A. (1999). COMMENTARY A Critical Evaluation of the Mechanisms of Action Proposed for the Antitumor Effects of the Anthracycline Antibiotics Adriamycin and Daunorubicin, *57*(98), 727–741.

González-Solís, J. L., Martínez-Espinosa, J. C., Torres-González, L. A., Aguilar-Lemarroy, A., Jave-Suárez, L. F., & Palomares-Anda, P. (2014). Cervical cancer detection based on serum sample Raman spectroscopy. *Lasers in Medical Science*, *29*(3), 979–985. https://doi.org/10.1007/s10103-013-1447-6

Gratton, S. E. A., Ropp, P. A., Pohlhaus, P. D., Luft, J. C., Madden, V. J., Napier, M. E., & Desimone, J. M. (2008). The effect of particle design on cellular internalization pathways, *105*(33).

Gstraunthaler Gerhard, L. T. (2013). *Zell- und Gewebekultur: Allgemeine Grundlagen und spezielle Anwendungen*. Retrieved from https://books.google.at/books?redir_esc=y&hl=de&id=yi8eBAAAQBAJ&q=objektträger#v=snippet&q=objektträger&f=false

Hager, S., Korbula, K., Bielec, B., Grusch, M., Pirker, C., Schosserer, M., … Heffeter, P. (2018). The thiosemicarbazone Me 2 NNMe 2 induces paraptosis by disrupting the ER thiol redox homeostasis based on protein disul fi de isomerase inhibition. *Cell Death and Disease*. https://doi.org/10.1038/s41419-018-1102-z

Hanlon, E. B., Manoharan, R., Koo, T., Shafer, K. E., Motz, J. T., Fitzmaurice, M., … Feld, M. S. (2000). Prospects for in vivo Raman spectroscopy, *45*.

Heffeter, P., Atil, B., Kryeziu, K., Groza, D., Koellensperger, G., Körner, W., … Berger, W. (2013). The ruthenium compound KP1339 potentiates the anticancer activity of sorafenib in vitro and in vivo. *European Journal of Cancer*, *49*(15), 3366–3375. https://doi.org/10.1016/j.ejca.2013.05.018

Henry, A. I., Sharma, B., Cardinal, M. F., Kurouski, D., & Van Duyne, R. P. (2016). Surface-enhanced Raman spectroscopy biosensing: In vivo diagnostics and multimodal imaging. *Analytical Chemistry*, *88*(13), 6638–6647. https://doi.org/10.1021/acs.analchem.6b01597

Hoffmann, E., Dittrich-breiholz, O., Holtmann, H., & Kracht, M. (2002). Multiple control of interleukin-8 gene expression, *72*(November).

Huang, J., Liu, S., Chen, Z., Chen, N., Pang, F., & Wang, T. (2016). Distinguishing Cancerous Liver Cells Using Surface-Enhanced Raman Spectroscopy, *15*(1), 36–43. https://doi.org/10.1177/1533034614561358

J. Coppé, P. Desprez, A. Krtolica, and J. C. (2014). The Senescence-Associated Secr1. Jean-Philippe Coppé, Pierre-Yves Desprez, Ana Krtolica, and J. C. The Senescence-Associated Secretory Phenotype: The Dark Side of Tumor Suppression. 99–118 (2014).

doi:10.1146/annurev-pathol-121808-102144.Theetory Phenotyp, 99–118. https://doi.org/10.1146/annurev-pathol-121808-102144.The

Jamieson, L. E., Asiala, S. M., Gracie, K., & Graham, D. (2017). *Bioanalytical Measurements Enabled by Surface- Enhanced Raman Scattering (SERS) Probes*.

Kalluri, R., & Zeisberg, M. (2006). Fibroblasts in cancer, *6*(May). https://doi.org/10.1038/nrc1877

Kenyon, C. J. (2010). The genetics of ageing. *Nature*, *464*(7288), 504–512. https://doi.org/10.1038/nature08980

Khalifian, S., Raimondi, G., & Brandacher, G. (2015). The Use of Luminex Assays to Measure Cytokines. *Journal of Investigative Dermatology*, *135*(8), 2142. https://doi.org/10.1038/jid.2015.112

Köhler, M., Machill, S., Salzer, R., & Krafft, C. (2009). Characterization of lipid extracts from brain tissue and tumors using Raman spectroscopy and mass spectrometry, 1513–1520. https://doi.org/10.1007/s00216-008-2592-9

Kopec, M., Imiela, A., & Abramczyk, H. (2019). Monitoring glycosylation metabolism in brain and breast cancer by Raman imaging. *Scientific Reports*, *9*(1), 1–13. https://doi.org/10.1038/s41598-018-36622-7

Kozhukharova, I., Zemelko, V., Kovaleva, Z., Alekseenko, L., Lyublinskaya, O., & Nikolsky, N. (2018). Therapeutic doses of doxorubicin induce premature senescence of human mesenchymal stem cells derived from menstrual blood, bone marrow and adipose tissue. *International Journal of Hematology*, *107*(3), 286–296. https://doi.org/10.1007/s12185-017-2346-6

Krafft, C., Knetschke, T., Siegner, A., Funk, R. H. W., & Salzer, R. (2003). Mapping of single cells by near infrared Raman microspectroscopy. *Vibrational Spectroscopy*, *32*(1 SPEC.), 75–83. https://doi.org/10.1016/S0924-2031(03)00049-3

Kritsilis, M., Rizou, S. V, Koutsoudaki, P. N., Evangelou, K., Gorgoulis, V. G., & Papadopoulos, D. (2018). Ageing , Cellular Senescence and Neurodegenerative Disease. https://doi.org/10.3390/ijms19102937

Krtolica, A., & Campisi, J. (2002). Cancer and aging : a model for the cancer promoting effects of the aging stroma, *34*, 1401–1414.

Li , S X, Zhang Y J, Zeng Q Y, Li L F, Guo Z Y, Liu Z M, X. H. L. and L. S. (2014). Potential of cancer screening with serum surface-enhanced Raman spectroscopy and a support vector machine. *Laser Physics Letter*, *065603*. https://doi.org/10.1088/1612-2011/11/6/065603

Liendl, L., Grillari, J., & Schosserer, M. (2019). Raman fingerprints as promising markers of cellular senescence and aging.

Lin, F., Nguyen, C. M., Wang, S., Saadi, W., Gross, S. P., & Li, N. (2004). Effective neutrophil

chemotaxis is strongly influenced by mean IL-8 concentration, *319*, 576–581. https://doi.org/10.1016/j.bbrc.2004.05.029

Liu, Y., Sanoff, H. K., Cho, H., Burd, C. E., Torrice, C., Ibrahim, J. G., … Sharpless, N. E. (2009). Expression of p16INK4a in peripheral blood T-cells is a biomarker of human agin, 439–448. https://doi.org/10.1111/j.1474-9726.2009.00489.x

Lizarbe, M. A., Barrasa, J. I., Olmo, N., Gavilanes, F., & Turnay, J. (2013). *Annexin-Phospholipid Interactions . Functional Implications*. https://doi.org/10.3390/ijms14022652

Loeser, R. F. (2009). Review Aging and osteoarthritis : the role of chondrocyte senescence and aging changes in the cartilage matrix. *Osteoarthritis and Cartilage*, *17*(8), 971–979. https://doi.org/10.1016/j.joca.2009.03.002

López-Otín, C., Blasco, M. A., Partridge, L., Serrano, M., & Kroemer, G. (2013). Review The Hallmarks of Aging, (Figure 1). https://doi.org/10.1016/j.cell.2013.05.039

Mader, A., & Kunert, R. (2010). Humanization strategies for an anti-idiotypic antibody mimicking HIV-1 gp41, *23*(12), 947–954. https://doi.org/10.1093/protein/gzq092

Maejima, Y., Adachi, S., Ito, H., Hirao, K., & Isobe, M. (2008). Induction of premature senescence in cardiomyocytes by doxorubicin as a novel mechanism of myocardial damage. *Aging Cell*, *7*(2), 125–136. https://doi.org/10.1111/j.1474-9726.2007.00358.x

Mao, F., Leung, W. Y., & Xin, X. (2007). Characterization of EvaGreen and the implication of its physicochemical properties for qPCR applications. *BMC Biotechnology*, *7*, 1–16. https://doi.org/10.1186/1472-6750-7-76

Mariani, M. M., Maccoux, L. J., Mattha, C., Diem, M., & Hengstler, J. G. (2010). Micro-Raman Detection of Nuclear Membrane Lipid Fluctuations in Senescent Epithelial Breast Cancer Cells, *82*(10), 4259–4263.

Markwalter, C. F., Jang, I. K., Burton, R. A., Domingo, G. J., & Wright, D. W. (2017). Biolayer interferometry predicts ELISA performance of monoclonal antibody pairs for Plasmodium falciparum histidine-rich protein 2. *Analytical Biochemistry*, *534*, 10–13. https://doi.org/10.1016/j.ab.2017.07.010

McDermott, G. P., Do, D., Litterst, C. M., Maar, D., Hindson, C. M., Steenblock, E. R., … Lowe, A. J. (2013). Multiplexed target detection using DNA-binding dye chemistry in droplet digital PCR. *Analytical Chemistry*, *85*(23), 11619–11627. https://doi.org/10.1021/ac403061n

Movasaghi, Z., Rehman, S., & Rehman, I. U. (2007). Raman spectroscopy of biological tissues. *Applied Spectroscopy Reviews*, *42*(5), 493–541. https://doi.org/10.1080/05704920701551530

Nishio, K., Inoue, A., Qiao, S., Kondo, H., & Mimura, A. (2001). Senescence and cytoskeleton: Overproduction of vimentin induces senescent-like morphology in human fibroblasts.

Histochemistry and Cell Biology, *116*(4), 321–327. https://doi.org/10.1007/s004180100325

Nygard, A. B., Jørgensen, C. B., Cirera, S., & Fredholm, M. (2007). Selection of reference genes for gene expression studies in pig tissues using SYBR green qPCR. *BMC Molecular Biology*, *8*, 1–6. https://doi.org/10.1186/1471-2199-8-67

Papazoglu, C., & Mills, A. A. (2007). p53 : at the crossroad between cancer and ageing, (Figure 2), 124–133. https://doi.org/10.1002/path

Petersen, R. L. (2017). Strategies using bio-layer interferometry biosensor technology for vaccine research and development. *Biosensors*, *7*(4). https://doi.org/10.3390/bios7040049

Pettinger, B., Ren, B., Picardi, G., Schuster, R., & Ertl, G. (2004). Nanoscale Probing of Adsorbed Species by Tip-Enhanced Raman Spectroscopy, (March), 8–11. https://doi.org/10.1103/PhysRevLett.92.096101

Qian, X., Peng, X., Ansari, D. O., Yin-goen, Q., Chen, G. Z., Shin, D. M., … Nie, S. (2008). In vivo tumor targeting and spectroscopic detection with surface-enhanced Raman nanoparticle tags, *26*(1), 83–90. https://doi.org/10.1038/nbt1377

RAMAN, C. V, & KRISHNAN, K. S. (1928). A New Type of Secondary Radiation. *Nature*, *121*(3048), 501–502. https://doi.org/10.1038/121501c0

Rieger, A. M., Nelson, K. L., Konowalchuk, J. D., & Barreda, D. R. (2011). Modified Annexin V / Propidium Iodide Apoptosis Assay For Accurate Assessment of Cell Death, (April), 3–6. https://doi.org/10.3791/2597

Rodier, F., & Campisi, J. (2011). Four faces of cellular senescence, *192*(4), 547–556. https://doi.org/10.1083/jcb.201009094

Roninson, I. B. (2003). Tumor Cell Senescence in Cancer Treatment 1, 2705–2715.

Roninson, I. B., Broude, E. V, Chang, B., & Cells, O. F. A. (2002). If not apoptosis, then what?Treatment-inducedsenescence and mitoticcatastrophe in tumor cells, (2001), 303–313. https://doi.org/10.1054/drup.2001.0213

Saretzki, G. (2009). Cellular Senescence in the Development and Treatment of Cancer. *Current Pharmaceutical Design*, *16*(1), 79–100. https://doi.org/10.2174/138161210789941874

Scott, G. K., Schokrpur, S., Patil, C. K., Orjalo, A. V, Lithgow, G. J., & Campisi, J. (2009). MicroRNAs miR - 146a / b negatively modulate the senescence - associated inflammatory mediators IL - 6 and IL - 8, *1*(4), 402–411.

Severino, J., Allen, R. G., Balin, S., Balin, A., & Cristofalo, V. J. (2000). Is ␣ -Galactosidase Staining a Marker of Senescence in Vitro and in Vivo ?, *171*(0014), 162–171. https://doi.org/10.1006/excr.2000.4875

Smith, J., Kendall, C., Sammon, A., Christie-Brown, J., & Stone, N. (2003). Raman spectral mapping in the assessment of axillary lymph nodes in breast cancer. *Technology in Cancer Research and Treatment*, *2*(4), 327–331. https://doi.org/10.1177/153303460300200407

Staroscik, A. (2004). Calculator for determining the number of copies of a template. Retrieved from https://cels.uri.edu/gsc/cndna.html

Stiles, P. L., Dieringer, J. A., Shah, N. C., & Duyne, R. P. Van. (2008). Surface-Enhanced Raman Spectroscopy. https://doi.org/10.1146/annurev.anchem.1.031207.112814

Stock, U. A. (2013). Raman spectroscopy in biomedicine – non-invasive in vitro analysis of cells and extracellular matrix components in tissues, *8*(March). https://doi.org/10.1002/biot.201200163

Stosch, R., Schiel, D., Gu, B., & Raman, A. (2005). Surface-Enhanced Raman Scattering Based Approach for Quantitative Determination of Creatinine in Human Serum, *77*(22), 7386–7392.

Sultana, A., & Lee, J. E. (2015). Measuring protein-protein and protein-nucleic acid interactions by biolayer interferometry. *Current Protocols in Protein Science*, *2015*, 19.25.1-19.25.26. https://doi.org/10.1002/0471140864.ps1925s79

T., K., C., M., W.J., M., & D.S., P. (2010). The essence of senescence. *Genes and Development*, *24*(22), 2463–2479. https://doi.org/10.1101/gad.1971610.by

Toussaint, O., Royer, V., Salmon, M., & Remacle, J. (2002). Stress-induced premature senescence and tissue ageing. *Biochemical Pharmacology*, *64*(5–6), 1007–1009. https://doi.org/10.1016/S0006-2952(02)01170-X

Vo-Dinh, T., Allain, L. R., & Stokes, D. L. (2002). Cancer gene detection using surface-enhanced Raman scattering (SERS). *Journal of Raman Spectroscopy*, *33*(7), 511–516. https://doi.org/10.1002/jrs.883

Wallner, J., Lhota, G., Jeschek, D., Mader, A., & Vorauer-uhl, K. (2013). Journal of Pharmaceutical and Biomedical Analysis Application of Bio-Layer Interferometry for the analysis of protein / liposome interactions. *Journal of Pharmaceutical and Biomedical Analysis*, *72*, 150–154. https://doi.org/10.1016/j.jpba.2012.10.008

Wallner, J., Lhota, G., Schosserer, M., & Vorauer-Uhl, K. (2017). An approach for liposome immobilization using sterically stabilized micelles (SSMs) as a precursor for Bio-layer Interferometry-based interaction studies. *Colloids and Surfaces B: Biointerfaces*. https://doi.org/10.1016/j.colsurfb.2017.03.015

Wartchow, C. A., Podlaski, F., Li, S., Rowan, K., Zhang, X., Mark, D., & Huang, K. Sen. (2011). Biosensor-based small molecule fragment screening with biolayer interferometry. *Journal of Computer-Aided Molecular Design*, *25*(7), 669–676. https://doi.org/10.1007/s10822-011-9439-8

Yang, C., Brooks, E., Li, Y., Denny, P., Ho, C., Qi, F., … Montemagno, C. D. (2005). Detection of

picomolar levels of interleukin-8 in human saliva by SPR, 1017–1023. https://doi.org/10.1039/b504737d

Yu, Wei W. White, I. M. (2012). A simple filter-based approach to surface enhanced Raman spectroscopy for trace chemical detectio, *137*(5), 1168–1173. https://doi.org/10.1039/c2an15947c.A

Zheng, Guangchao Polavarapu, Lakshminarayana Liz-Marzán, Luis M Pastoriza-Santos, I. P.-J. J. (2012). Gold Nanoparticle-loaded Filter paper: A Recyclable “Dip-Catalyst” for Real-Time Reaction Monitoring by Surface Enhanced Raman Scattering. https://doi.org/10.1039/x0xx00000x

Zong, C., Xu, M., Xu, L., Wei, T., Ma, X., Zheng, X., … Ren, B. (2018). Surface-Enhanced Raman Spectroscopy for Bioanalysis : Reliability and Challenges. https://doi.org/10.1021/acs.chemrev.7b00668

8 | APPPENDIX

8.1 Register of figures

8.2 Register of tables

8.3 Paper (co-authorship)

Title: The thiosemicarbazone Me2NNMe2 induces paraptosis by disrupting the ER thiol redox homeostasis based on protein disulfide isomerase inhibition

Authors: Sonja Hager**,** Katharina Korbula, Björn Bielec, Michael Grusch, Christine Pirker, Markus Schosserer , Lisa Liendl, Magdalena Lang, Johannes Grillari, Karin Nowikovsky, Veronika F.S. Pape**,** Thomas Mohr, Gergely Szakács, Bernhard K. Keppler, Walter Berger**,** Christian R. Kowol and Petra Heffeter

Hager et al. *Cell Death and Disease* (2018)9:1052
DOI 10.1038/s41419-018-1102-z

Cell Death & Disease

ARTICLE Open Access

The thiosemicarbazone Me_2NNMe_2 induces paraptosis by disrupting the ER thiol redox homeostasis based on protein disulfide isomerase inhibition

Sonja Hager[1,2], Katharina Korbula[1,2], Björn Bielec[2,3], Michael Grusch[1], Christine Pirker[1], Markus Schosserer[4], Lisa Liendl[4], Magdalena Lang[4], Johannes Grillari[4,5,6], Karin Nowikovsky[7], Veronika F. S. Pape[8,9], Thomas Mohr[1,10], Gergely Szakács[1,9], Bernhard K. Keppler[2,3], Walter Berger[1,2], Christian R. Kowol[2,3] and Petra Heffeter[1,2]

Abstract

Due to their high biological activity, thiosemicarbazones have been developed for treatment of diverse diseases, including cancer, resulting in multiple clinical trials especially of the lead compound Triapine. During the last years, a novel subclass of anticancer thiosemicarbazones has attracted substantial interest based on their enhanced cytotoxic activity. Increasing evidence suggests that the double-dimethylated Triapine derivative Me_2NNMe_2 differs from Triapine not only in its efficacy but also in its mode of action. Here we show that Me_2NNMe_2- (but not Triapine)-treated cancer cells exhibit all hallmarks of paraptotic cell death including, besides the appearance of endoplasmic reticulum (ER)-derived vesicles, also mitochondrial swelling and caspase-independent cell death via the MAPK signaling pathway. Subsequently, we uncover that the copper complex of Me_2NNMe_2 (a supposed intracellular metabolite) inhibits the ER-resident protein disulfide isomerase, resulting in a specific form of ER stress based on disruption of the Ca^{2+} and ER thiol redox homeostasis. Our findings indicate that compounds like Me_2NNMe_2 are of interest especially for the treatment of apoptosis-resistant cancer and provide new insights into mechanisms underlying drug-induced paraptosis.

Introduction

α-*N*-Heterocyclic thiosemicarbazones (TSCs) are a promising class of therapeutics, which have been extensively investigated for their anticancer activity[1,2]. The most prominent and best-studied drug candidate is 3-aminopyridine-2-carboxaldehyde TSC, also known as Triapine. Triapine displayed promising results in clinical phase I and II trials against hematological cancers[3–6] and has also been tested against diverse solid tumors[7,8]. In addition, several new TSC derivatives have been developed over the last years. Two of them, namely Coti-2 and DpC, have recently entered clinical phase I trials (www.clinicaltrials.gov). Coti-2, DpC as well as the predecessor Dp44mT showed highly improved anticancer activities compared to Triapine with IC_{50} values in the nanomolar concentration range (hence, called "nanomolar TSCs")[9,10]. Our group has recently synthesized a new nanomolar TSC derivative, Me_2NNMe_2, characterized by dimethylation of both primary amino groups of the Triapine molecule(Fig. 1)[2,11].

Based on promising clinical trials, it is of interest to better elucidate the reasons for the greatly improved anticancer activity of nanomolar TSCs. There are several indications that nanomolar TSCs differ in their mode of

Correspondence: Petra Heffeter (petra.heffeter@meduniwien.ac.at)
[1]Institute of Cancer Research and Comprehensive Cancer Center, Department of Medicine I, Medical University of Vienna, Borschkegasse 8a, A-1090 Vienna, Austria
[2]Research Cluster "Translational Cancer Therapy Research", Vienna, Austria
Full list of author information is available at the end of the article.
Edited by: P. Salomoni

© The Author(s) 2018
Open Access This article is licensed under a Creative Commons Attribution 4.0 International License, which permits use, sharing, adaptation, distribution and reproduction in any medium or format, as long as you give appropriate credit to the original author(s) and the source, provide a link to the Creative Commons license, and indicate if changes were made. The images or other third party material in this article are included in the article's Creative Commons license, unless indicated otherwise in a credit line to the material. If material is not included in the article's Creative Commons license and your intended use is not permitted by statutory regulation or exceeds the permitted use, you will need to obtain permission directly from the copyright holder. To view a copy of this license, visit http://creativecommons.org/licenses/by/4.0/.

SPRINGER NATURE CDDpress

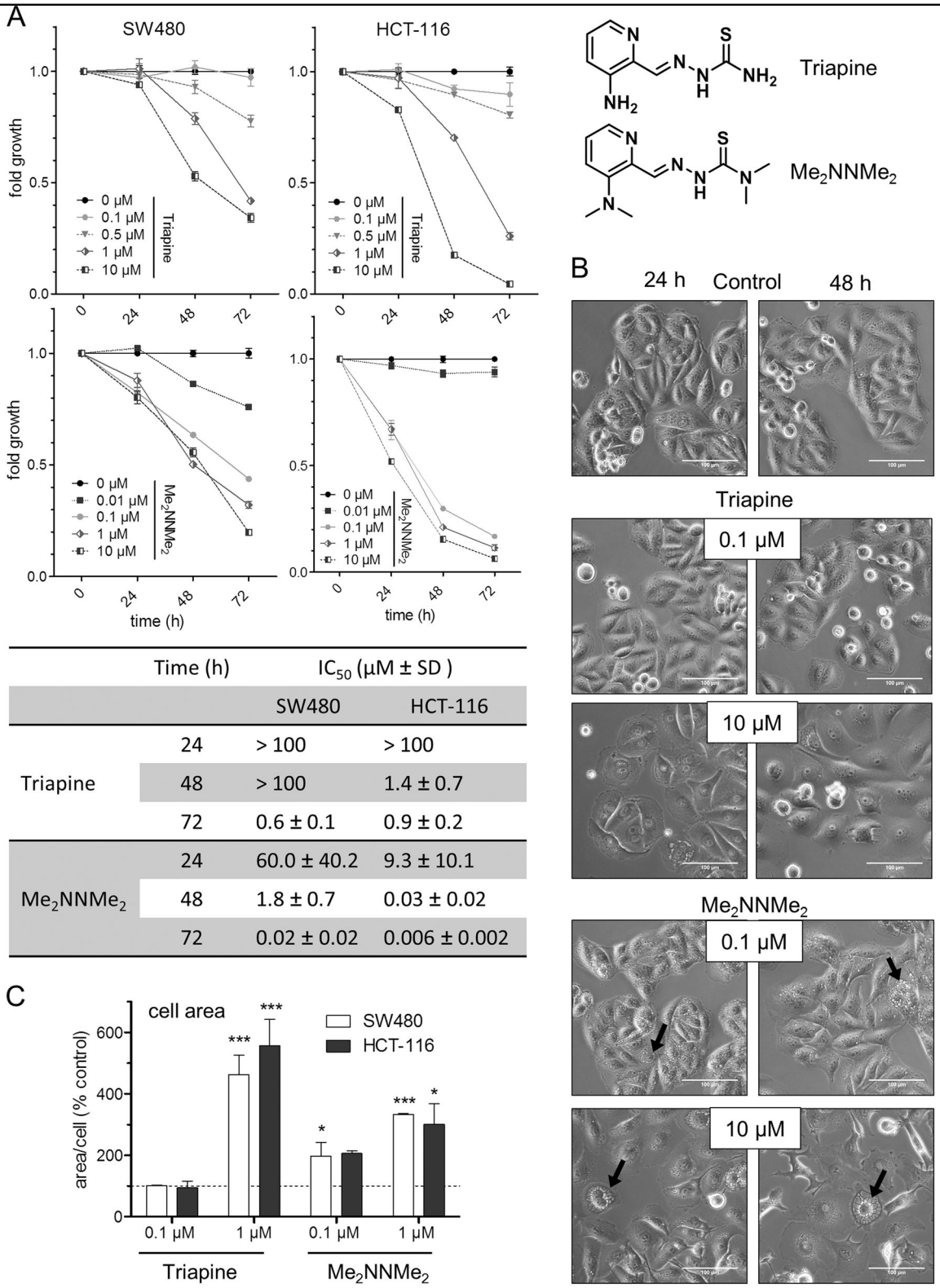

	Time (h)	IC_{50} (µM ± SD)	
		SW480	HCT-116
Triapine	24	> 100	> 100
	48	> 100	1.4 ± 0.7
	72	0.6 ± 0.1	0.9 ± 0.2
Me_2NNMe_2	24	60.0 ± 40.2	9.3 ± 10.1
	48	1.8 ± 0.7	0.03 ± 0.02
	72	0.02 ± 0.02	0.006 ± 0.002

Fig. 1 (See legend on next page.)

(see figure on previous page)
Fig. 1 Activity of Triapine and its derivative Me_2NNMe_2. a Time-dependent cell viability of SW480 and HCT-116 cells treated with either Triapine or Me_2NNMe_2, determined by MTT assay after 24, 48, and 72 h. Values given in the graph are the mean ± standard deviation of triplicates from one representative experiment out of three, normalized to the untreated control of the same time-point. IC_{50} values (μM) ± standard deviations (SD) are given in the table . **b** Morphological changes in SW480 cells induced by 24 and 48 h treatment with the indicated concentrations of Triapine or Me_2NNMe_2. Cytoplasmic vacuoles were mainly seen with Me_2NNMe_2 (arrows). Scale bar: 100 μm. **c** Increase in cell size of SW480 and HCT-116 cells treated with the indicated concentrations of Triapine and Me_2NNMe_2 for 48 h

action from Triapine[2,12,13]. In particular, their interaction with intracellular copper ions might be important, as intracellularly formed copper complexes have been suggested to be the active metabolites of nanomolar TSCs[12–14]. In this regard, during our recent studies, we have discovered that treatment with Me_2NNMe_2 as well as Dp44mT resulted in the formation of perinuclear cytoplasmic vesicles[11] that are characteristic for paraptosis, a recently described new type of programmed cell death[15,16]. Further hallmarks of paraptosis include mitochondrial swelling and damage, caspase-independent cell death and the absence of membrane blebbing/DNA condensation or fragmentation. Moreover, disruption of endoplasmic reticulum (ER) homeostasis, activation of MAPK signaling as well as protection by the thiol-containing radical scavenger *N*-acetylcysteine (NAC) and the MEK inhibitor U0126 have been reported[15,16]. However, the exact molecular mechanisms underlying paraptosis induction are widely unexplored.

So far, mainly diverse natural compounds have been identified as paraptosis inducers. Interestingly, the list also includes some copper complexes[17–19], supporting the idea that nanomolar TSCs could also induce this novel form of cell death. Therefore, in this study, we investigated the role of apoptotic and paraptotic cell death in the mode of action of Triapine and Me_2NNMe_2. Our experiments revealed that treatment with Me_2NNMe_2 induces all of the main hallmarks of paraptotic cell death. In addition, we identified the inhibition of the ER-resident protein disulfide isomerase (PDI) as a potential target of the intracellularly formed Me_2NNMe_2 copper metabolite.

Results

Anticancer activity of Triapine and Me_2NNMe_2

Cytotoxicity and morphological changes induced by Triapine and Me_2NNMe_2 were investigated in SW480 and HCT-116 cells at different time points (Fig. 1a). In general, HCT-116 cells proved to be more sensitive to TSC treatment than SW480. Moreover, in accordance with previous results[11], double-dimethylation of Triapine resulted in markedly higher activity in a time-dependent manner. The two drugs had distinct effects on cell morphology, as shown in Fig. 1b, c. Especially, Triapine-treated cells were characterized by increased cell area (up to 500%) and flattening (Fig. 1c). In contrast, treatment with Me_2NNMe_2 led to formation of cytoplasmic vesicles (see black arrows in Fig. 1b), which dose- and time-dependently increased in size and number (Fig. 1b, Suppl. Figure 1). These observations were consistent in both cell lines. Comparable vesicle formation was also observed with the other nanomolar TSCs, DpC, Dp44mT, and Coti-2 (Suppl. Figure 2).

Me_2NNMe_2 accumulation in the ER-derived vesicles

Several groups have reported that paraptosis induction is associated with the appearance of cytoplasmic vesicles originating from the ER[15,16]. To investigate whether the cytoplasmic vesicles seen in Me_2NNMe_2-treated cells also arise from the ER, transfection experiments with ER-localized YFP were performed (Fig. 2a). As visualized by live-cell microscopy, ER-derived vesicles formed around the nucleus and rapidly increased in size (by fusion) (Fig. 2b). Moreover, no overlap of these vesicles with mitochondria or lysosomes was found (Fig. 2c and Suppl. Figure 3). Consequently, we concluded that the observed cytoplasmic vesicles after Me_2NNMe_2 treatment originated solely from the ER.

Mapping cells by Raman microspectroscopy and subsequent principal component analysis (PCA) revealed a unique biochemical composition of these vesicles compared to the rest of the cell (Fig. 2d). Component spectra suggested enrichment of lipids (bands at ~1295 cm^{-1}, 1435–1480 cm^{-1}, and ~1650 cm^{-1}) in these vesicles, while bands corresponding to nucleic acids (~715 cm^{-1}, ~775 cm^{-1}, ~1090 cm^{-1}, and ~1570 cm^{-1}) were weaker compared to the rest of the cell (Suppl. Figure 4A)[20]. Furthermore, classical least squares (CLS) fitting of the spectrum of the pure substance (Suppl. Figure 4B) to the Raman map revealed that Me_2NNMe_2 appears to accumulate in these vesicles (Fig. 2d), indicating that the compound might have its intracellular target in the ER.

Impact of the TSCs on mitochondrial integrity

Paraptotic cell death is frequently associated with changes of mitochondrial morphology and functionality[21–27]. Consequently, JC-1 staining was conducted to evaluate the impact of both drugs on mitochondrial membrane potential. Upon treatment with Triapine, only slight, non-significant effects were detected in both cell lines (Fig. 3a), while Me_2NNMe_2 had a profound impact. In detail, in SW480 cells, at all investigated concentrations ~10% of the cells displayed depolarized mitochondria. In

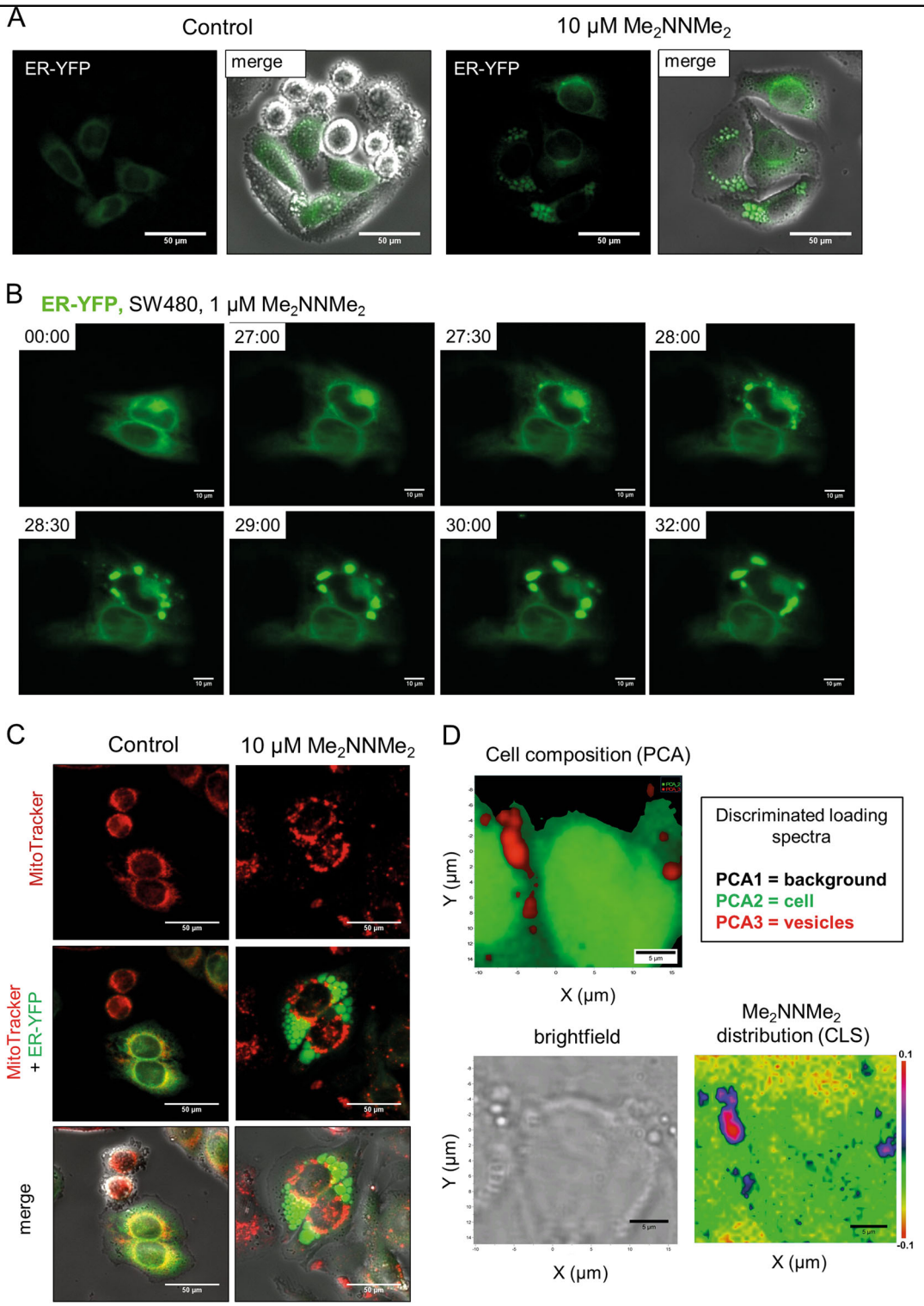

Fig. 2 Me_2NNMe_2 accumulation in the ER-derived vesicles. a Representative fluorescence microscopy images and overlaid differential interference contrast images of the ER lumen of ER-YFP-transfected SW480 cells treated with 10 µM Me_2NNMe_2 for 24 h (scale bar: 50 µm). **b** Life-cell fluorescence imaging of ER-located YFP-transfected SW480 cells treated with 1 µM Me_2NNMe_2. Time after treatment is indicated as hh:mm (scale bar: 10 µm). **c** Representative fluorescence microscopy images of mitochondria (MitoTracker) showing no overlap with vesicles in ER-YFP-transfected SW480 cells treated with 10 µM Me_2NNMe_2. (scale bar: 50 µm). **d** Raman microspectroscopy of SW480 cells treated with 10 µM Me_2NNMe_2 for 24 h. Principal component analysis (PCA) of Raman spectra can differentiate between background (black), cell (green) and vesicles (red). CLS fitting of Me_2NNMe_2 Raman spectrum to the spectral map of the cell revealed accumulation of the drug inside the vesicles

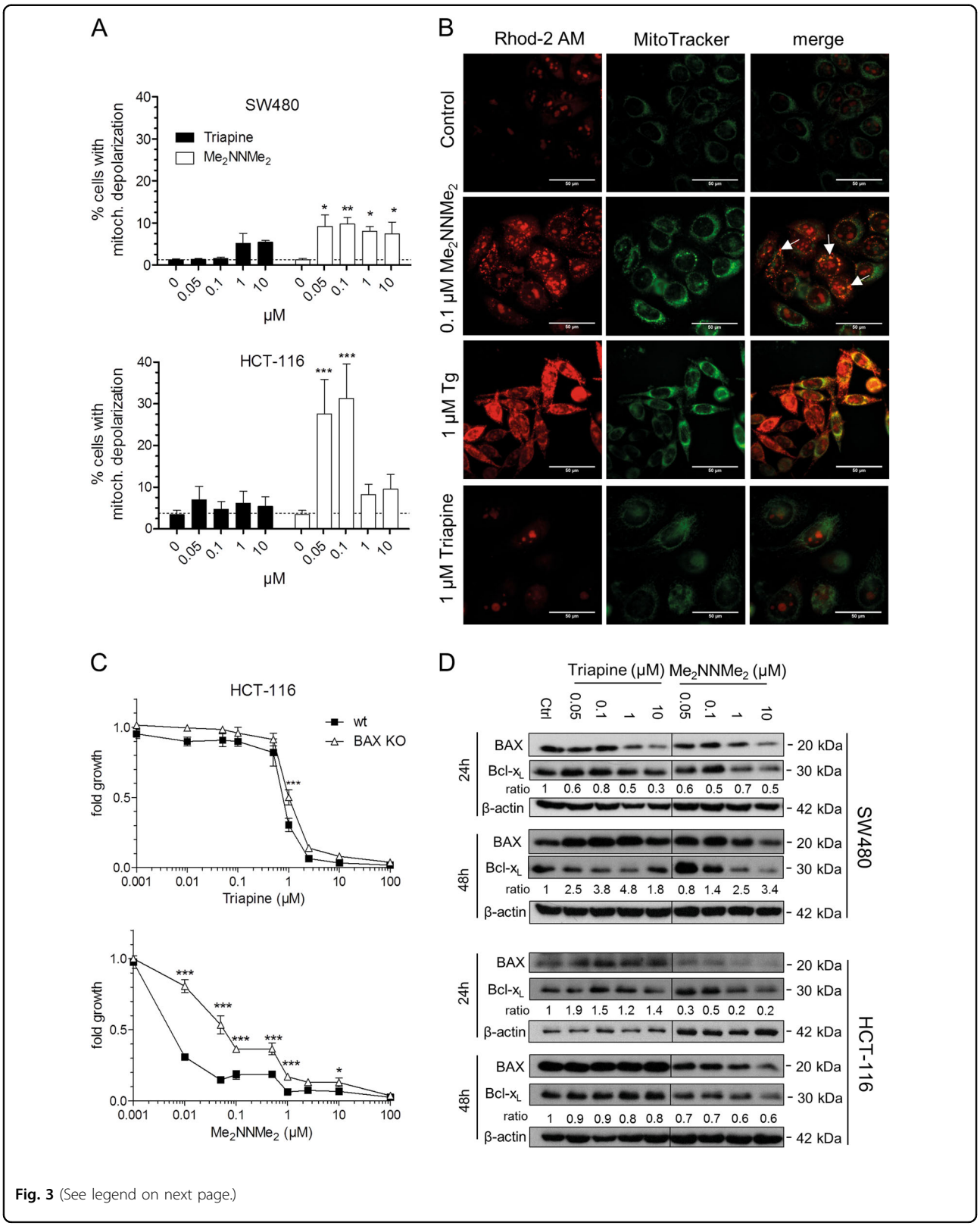

Fig. 3 (See legend on next page.)

(see figure on previous page)

Fig. 3 Mitochondrial involvement in the activity of Triapine and Me_2NNMe_2. a Mitochondrial membrane potential depolarization measured by the percentage of cells with decreased JC-1 fluorescence (red). SW480 or HCT-116 cells were treated with the indicated concentrations of Triapine or Me_2NNMe_2 for 24 h. Values given are the mean ± standard deviation of three independent experiments. **b** Fluorescence microscopy of increased calcium levels (Rhod-2 AM in red) specifically in the mitochondria (MitoTracker in green) after thapsigargin (Tg, 1 μM), Me_2NNMe_2 (0.1 μM) or Triapine (1 μM) treatment of SW480 cells for 48 h (scale bar: 50 μm). White arrows indicate co-localization. **c** Cell viability of HCT-116 wild-type (wt) and BAX knockout (KO) cells measured by MTT after 72 h treatment with indicated concentrations of Triapine or Me_2NNMe_2. Values given are the mean ± standard deviation of triplicates of one representative experiment out of three. **d** Western blot analysis of BAX and Bcl-x_L expressed by SW480 and HCT-116 cells treated with Triapine or Me_2NNMe_2 for 24 or 48 h. The ratio of BAX to Bcl-x_L is given below the respective bands. β-actin was used as a loading control. Significance was calculated to control with one-way (**a**) and to wt cells with two-way (**c**) ANOVA and Bonferroni's multiple comparison test (***$p < 0.001$, **$p \leq 0.01$, *$p \leq 0.05$)

contrast, 30% of HCT-116 cells showed mitochondrial depolarization at 0.05 and 0.1 μM Me_2NNMe_2, which decreased to about 10% at higher concentrations. In parallel to mitochondrial depolarization, Me_2NNMe_2, but not Triapine, induced mitochondrial fragmentation or swelling (a main hallmark of paraptosis) already at 0.1 μM (Suppl. Figure 5). In order to investigate whether this observed swelling is accompanied by increased intra-mitochondrial Ca^{2+} levels, Rhod-2 AM stains were performed. Indeed, distinct accumulation of mitochondrial Ca^{2+} together with organelle swelling was observed in Me_2NNMe_2-exposed cells (Fig. 3b). In contrast, thapsigargin, a well-known SERCA (ER-localized Ca^{2+} ATPase) inhibitor and ER stress inducer, initiated mitochondrial Ca^{2+} accumulation but no organelle swelling. Together with the lack of organelle swelling, Triapine had also no impact on mitochondrial Ca^{2+} levels (Fig. 3b).

In agreement with the suggested contribution of mitochondria to Me_2NNMe_2 activity, HCT-116 cells with a BAX knockout[18] were (in contrast to Triapine) significantly less sensitive to the methylated derivative (Fig. 3c). Interestingly, Me_2NNMe_2 activity was accompanied by a decrease of both pro-apoptotic BAX as well as anti-apoptotic Bcl-x_L protein levels in BAX wild-type cells, which argues against induction of apoptosis via the intrinsic (mitochondrial) pathway (Fig. 3d). Taken together, this indicates that Me_2NNMe_2 distinctly impacts on mitochondrial integrity already at very low drug concentrations and disruption of mitochondrial Ca^{2+} homeostasis is a key event in Me_2NNMe_2-induced paraptosis.

Caspase independence of Me_2NNMe_2 anticancer activity

As paraptosis is often described as a caspase-independent process[15,16], as a next step the impact of the pan-caspase inhibitor z-VAD-FMK on the activity of the two TSCs was investigated. As shown in Fig. 4a, there was no relevant effect of z-VAD-FMK on the anticancer activity of the tested TSCs, in contrast to TRAIL, which was used as a positive control (Suppl. Figure 6). In addition, treatment with the pan-caspase inhibitor did not prevent the formation of cytoplasmic vesicles induced by Me_2NNMe_2 (Fig. 4b). To confirm the caspase independence of Me_2NNMe_2-induced cell death, annexin V (AV) stains were performed in the presence and absence of the pan-caspase inhibitor (Fig. 4c). Caspase inhibition had no significant impact (calculated to control by one-way ANOVA and Bonferroni's multiple comparison test) on the AV^+ cell fractions after Me_2NNMe_2 treatment in both cell lines. In contrast, Triapine-induced cell death in HCT-116 was strongly diminished upon addition of z-VAD-FMK, suggesting cell line-dependent apoptosis induction by this compound.

The role of MAPKs in Me_2NNMe_2-induced paraptosis

There are indications that MAPK signaling plays an important role in the execution of paraptotic cell death[16,28]. However, whether and how Me_2NNMe_2 activity impacts on this pathway is so far unknown. Consequently, as a first step, we compared gene signatures of whole-genome gene expression arrays performed with 0.1 μM and 1 μM Me_2NNMe_2 treatment or untreated cells. Gene set enrichment analysis (GSEA) of these data showed significant upregulation of MAPK signaling pathway genes in treated as compared to untreated cells at both concentrations (Fig. 5a). A more detailed illustration of the genes up- (red) or down- (blue) regulated in this KEGG pathway is shown in Fig. 5b. When comparing these mRNA data with Western blot analysis of MEK and ERK, interestingly, both Triapine and Me_2NNMe_2 treatment had a tendency to stimulate the MAPK signaling at higher drug concentrations (Fig. 5c). However, at lower doses strongly reduced phosphorylation (especially of MEK1/2) was observed, indicating that stimulation of the MAPK pathway could be due to a compensatory feedback loop.

To gain more insight into the role of the MAPK pathway in the activity of our TSCs, several MEK inhibitors (U0126, PD98058, trametinib, and selumetinib) with different affinities for MEK1 and MEK2 were used. As seen in Fig. 6a and Suppl. Table 1, all inhibitors were able to protect cells against Me_2NNMe_2-induced cytotoxicity. However, only U0126 distinctly reduced vesicle formation in Me_2NNMe_2 (Fig. 6b, c). The effects of U0126 were also confirmed in HCT-116 cells (data not shown). In contrast to Me_2NNMe_2, Triapine activity was largely unaffected by the MEK inhibitors. As U0126 is the only inhibitor that

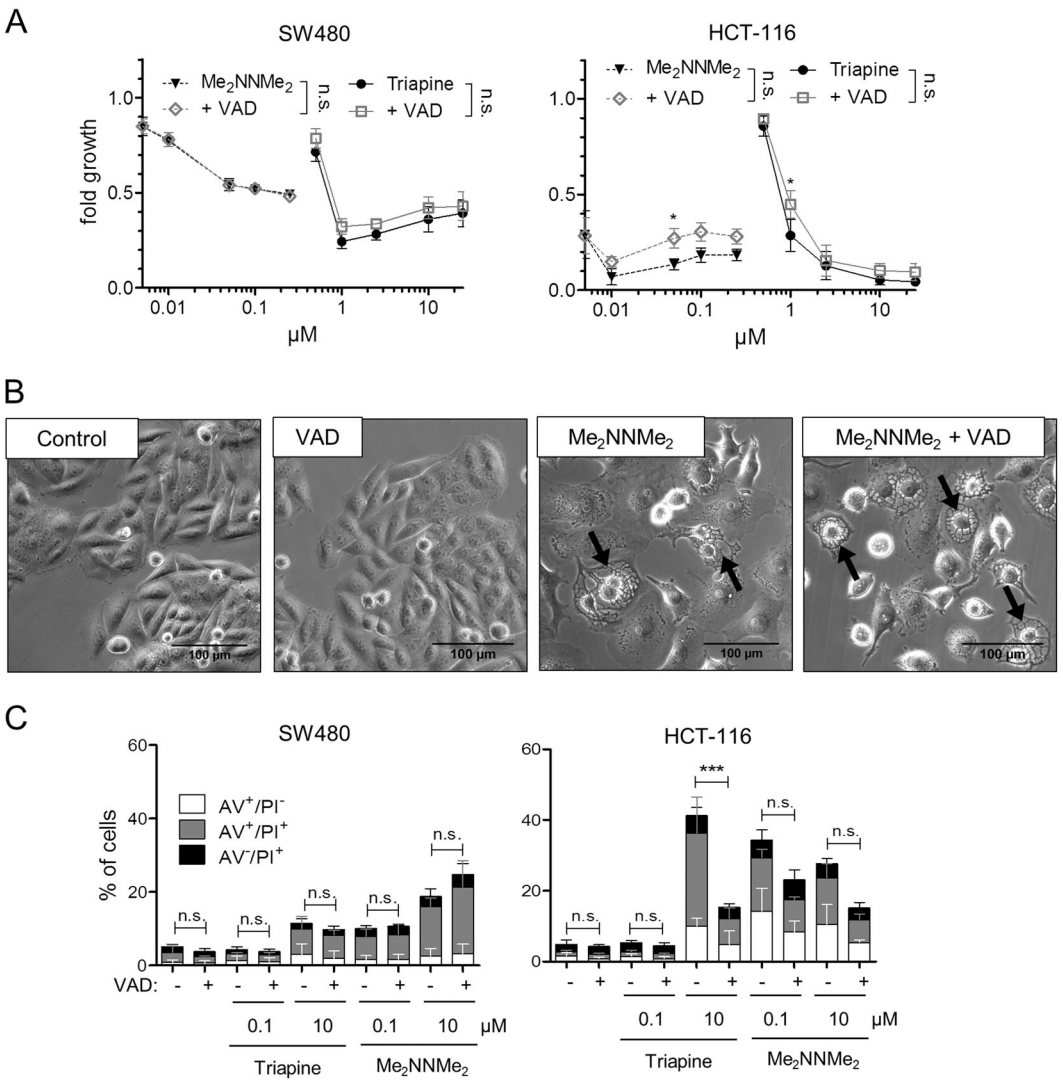

Fig. 4 Induction of different cell death characteristics by Triapine and Me_2NNMe_2. a Cell viability measured by MTT assay of SW480 and HCT-116 cells after 72 h treatment with the indicated concentrations of Triapine (full lines) or Me_2NNMe_2 (dotted lines) alone or in combination with 10 μM z-VAD-FMK (VAD, gray lines). Values given are the mean ± standard deviation of triplicates from one representative experiment out of three. **b** Phase-contrast microscopy images of SW480 cells treated with 10 μM Me_2NNMe_2 or 25 μM z-VAD-FMK as well as the combination (scale bar: 100 μm). **c** Percentage of annexin V-positive (AV^+) and/or PI^+ SW480 or HCT-116 cells detected by flow cytometry after 48 h of Triapine or Me_2NNMe_2 treatment in combination with 10 μM z-VAD-FMK (VAD). Values given are the mean ± standard deviation of three independent experiments. For calculation of significance AV^+ cell fractions (AV^+/PI^-, AV^+/PI^+) were added. Significance to control was calculated by two-way (**a**) or one-way (**c**) ANOVA and Bonferroni's multiple comparison test using GraphPad Prism software (***$p < 0.001$, **$p \leq 0.01$, *$p \leq 0.05$)

inhibits MEK1 and 2 to a similar extent (while the others have a stronger preference for MEK1), we hypothesized that MEK2 could have a special role in Me_2NNMe_2 activity. To further evaluate this hypothesis, knockdown experiments using siRNA against MEK2 were performed (Fig. 6d). Indeed, further analysis revealed that Me_2NNMe_2-induced vacuolization decreased upon MEK2 knockdown (Fig. 6e, f) confirming the importance of this protein in the formation of paraptotic vesicles by Me_2NNMe_2. Noteworthy, also induction of vesicles and anticancer activity of other nanomolar TSC (DpC, Dp44mT, and Coti-2) could be inhibited by U0126 (Suppl. Figure 7), indicating induction of paraptotic cell death also with these TSCs.

Me_2NNMe_2-induced ER stress based on disturbed ER thiol redox homeostasis

So far, there are only a few hypotheses on the exact mechanisms underlying paraptosis induction. In case of natural products, especially proteasome inhibition

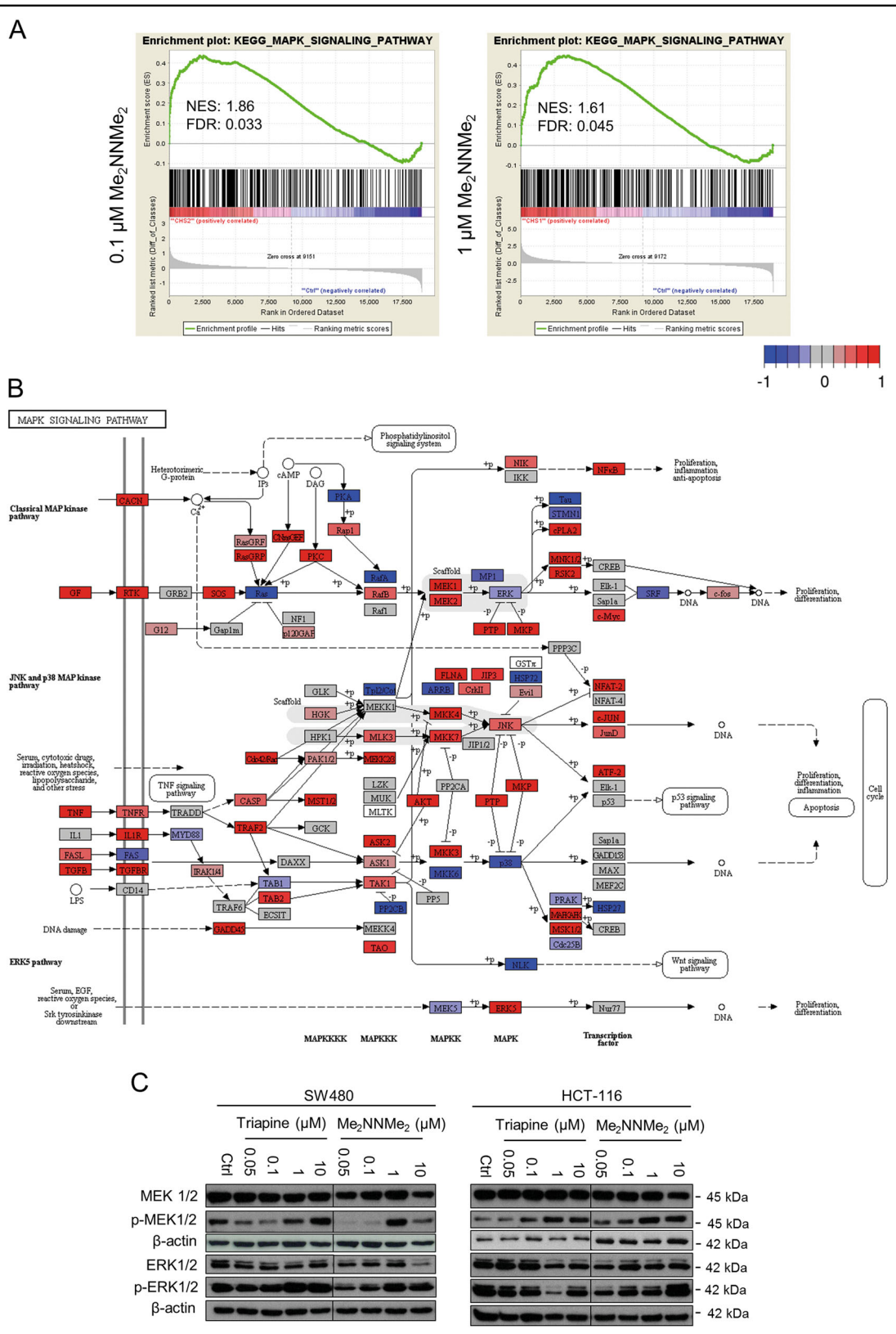

Fig. 5 (See legend on next page.)

(see figure on previous page)
Fig. 5 Role of the MAPK pathway in the activity of Triapine and Me_2NNMe_2. a GSEA from whole-genome gene expression data revealed significant enrichment of genes in the "MAPK signaling pathway" gene set in SW480 cells treated with 0.1 or 1 μM Me_2NNMe_2 compared to untreated cells. Normalized enrichment score (NES) and false discovery rate (FDR) are given. **b** Illustration of genes up- (red) or down-regulated (blue) in the KEGG-derived "MAPK signaling pathway" of Me_2NNMe_2 (1 μM)-treated compared to untreated SW480 cells using whole-genome gene expression data. **c** Western blot analysis of MEK1/2 and ERK1/2 as well as their phosphorylated protein levels in SW480 and HCT-116 cells treated with indicated concentrations of Triapine and Me_2NNMe_2 for 24 h. β-actin was used as a loading control

resulting in (unfolded) protein stress has been suggested[16,29]. Consequently, paraptosis induction by such drugs is often dependent on active protein synthesis. However, inhibition of protein synthesis (by cycloheximide) had no impact on the activity of Me_2NNMe_2 and no difference was observed in the impact on protein ubiquitination levels between Triapine and Me_2NNMe_2 (data not shown), suggesting another mode of action. Based on ER localization of Me_2NNMe_2 in the Raman microscopy studies together with the profound ER blebbing, we hypothesized that Me_2NNMe_2 might have a target in this organelle. In line with this hypothesis, subsequent experiments confirmed a specific form of ER stress especially in Me_2NNMe_2-treated cells. In more detail, Me_2NNMe_2 (but not Triapine) treatment resulted in enhanced nuclear localization of CHOP, an ER stress-induced transcription factor, (Fig. 7a and Suppl Figure 8) together with increased phosphorylation of its upstream activator PERK (Fig. 7b). In contrast, no changes in other ER stress markers, such as BiP, IRE1α, calnexin, or changes in the phosphorylation of eIF2-α were detected. Remarkably, in contrast to thapsigargin, CHOP-regulated ero1L-α (an ER-specific thiol oxidase) as well as the ER-localized chaperone, isomerase and thiol oxidoreductase PDI were upregulated by both Triapine and Me_2NNMe_2 (Fig. 7b). Moreover, our array data showed that the expression of these proteins was also increased on mRNA level upon Me_2NNMe_2 treatment (Fig. 7c), indicating increased gene transcription of these CHOP-target genes.

Interestingly, there are reports that PDI is able to bind and reduce copper (although the impact of copper binding on the enzymatic activity is not fully characterized)[30]. As Me_2NNMe_2 has strong copper-binding properties and our previous studies already indicated that addition of copper strongly increases the activity of Me_2NNMe_2[11], we hypothesized that our drug or its copper metabolite interferes with the functionality of PDI. Subsequently performed enzyme inhibition assays revealed that, indeed, the copper complex of Me_2NNMe_2 (but not of Triapine) had strong PDI-inhibitory potential (Fig. 7d). Noteworthy, the metal-free drugs did not inhibit the enzyme, even at high concentrations, suggesting that prior (intracellular) copper chelation is necessary for PDI inhibition. Similar activity was also detected with the copper complexes of DpC and Dp44mT (Suppl. Figure 9).

PDI plays a key role in the ER thiol redox homeostasis by forming and rearranging disulfide bonds during protein folding. In this process, PDI oxidizes unfolded target proteins with the help of oxidized thiol-containing molecules, such as GSSG or ero1L-α, thereby resulting in the reduction of these molecules[31]. To gain more insight into the role of the ER thiol redox homeostasis in the mode of action of Me_2NNMe_2, co-incubation experiments with the thiol-containing antioxidants NAC and 1-thioglycerol were performed. Indeed, both compounds protected the cells from Me_2NNMe_2 (but not Triapine)-induced cytotoxicity (Fig. 7e and Suppl. Figure 10). In addition, NAC also reduced anticancer activity induced by DpC, Dp44mT and Coti-2 (Suppl. Figure 7C). Noteworthy, these Me_2NNMe_2-induced effects were not based on enhanced global superoxide (Fig. 7f) or ROS[11] levels but coincided with increased glutathione and especially GSSG levels (Fig. 7g). This suggests that nanomolar TSCs induce either a very local, organelle specific form of ROS or ROS generation does not play a major role in their anticancer activity.

Taken together, these results indicate that Me_2NNMe_2 might form an intracellular copper metabolite with PDI-inhibitory properties, which then results in disturbed ER thiol redox balance and paraptosis induction. The proposed mode of action is shown in Fig. 8.

Discussion

In anticancer therapy, resistance of cancer cells to apoptosis is a major obstacle to successful treatment and the cause of many cancer-associated deaths[32]. Targeting cancer cells by the induction of paraptosis, a recently discovered alternative caspase-independent cell death pathway[15,16], offers the opportunity to overcome apoptosis resistance. However, the mechanisms of paraptosis are still not fully understood (and sometimes even contradictory observations have been published[16,33]), making the in-depth investigation of the underlying signaling pathways of high importance. In general, there are several main hallmarks of paraptosis that are widely accepted. Among these, cytoplasmic (ER-derived) vacuolization, mitochondrial swelling/damage, caspase independence together with absence of membrane blebbing as well as DNA condensation/fragmentation, disruption of ER homeostasis, activation of MAPK signaling, protection by

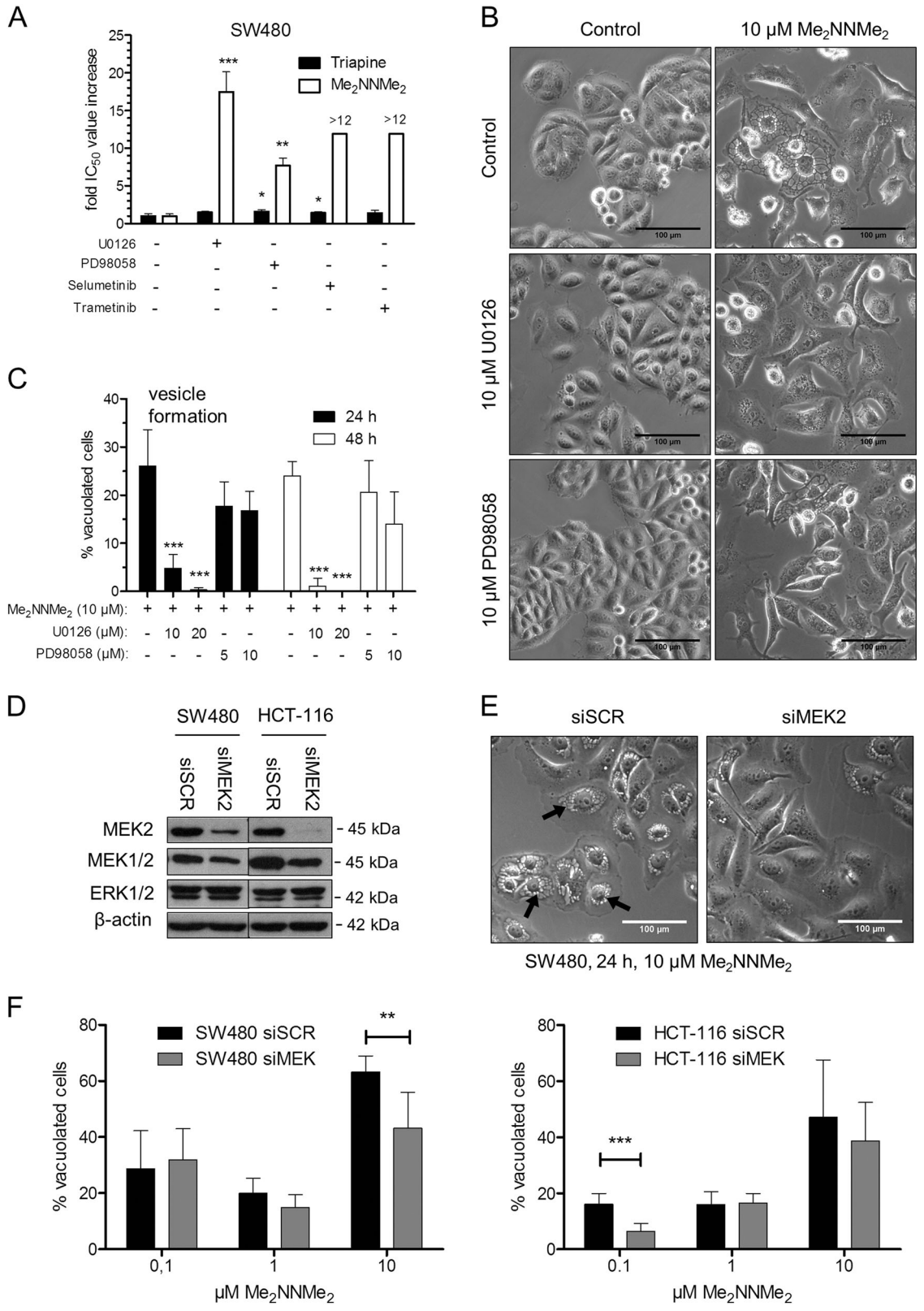

Fig. 6 (See legend on next page.)

(see figure on previous page)
Fig. 6 MEK1/2 inhibition affects Me_2NNMe_2-induced cell death. a Impact of MEK1/2 inhibitors U0126 (5 μM), PD98058 (5 μM), selumetinib (50 nM) or trametinib (100 nM) on viability of Triapine- or Me_2NNMe_2-treated SW480. Change in viability is given as mean fold IC_{50} value increase ± standard deviation compared to Triapine or Me_2NNMe_2 treatment alone, measured by three independent MTT viability experiments. **b** Representative phase-contrast microscopy images of SW480 cells treated with Me_2NNMe_2 (10 μM) and U0126 (20 μM) or PD98058 (10 μM) as well as the combinations for 48 h (scale bar: 100 μm). **c** Percentage of vacuolated cells counted from phase-contrast microscopy images seen in **b**. Values given are the mean ± standard deviation of three images with at least 30 cells in total. Significance to single treatment was calculated by one-way ANOVA and Bonferroni's multiple comparison test (***$p < 0.001$, **$0.001 \geq p \leq 0.01$, *$0.01 \geq p \leq 0.05$). **d** Protein expression detected by Western blot of MEK2, MEK1/2, and ERK1/2 in SW480 and HCT-116 cells after 48 h gene silencing with scrambled (siSCR) or MEK2 (siMEK2) siRNA. β-actin was used as a loading control. **e** Representative images of SW480 cells transfected with siSCR or siMEK2 and treated with 10 μM Me_2NNMe_2 for 24 h (scale bar: 100 μm). **f** Percentage of cell vacuolization of SW480 or HCT-116 cells transfected with siSCR or siMEK2 and treated with the indicated concentrations of Me_2NNMe_2 for 24 h. Values given are the mean ± standard deviation of several regions of two experiments. Significance to siSCR was calculated by Student's *T*-test (***$p < 0.001$, **$p \leq 0.01$)

NAC and U0126 as well as protein synthesis dependence are most prominent[15,16].

So far, mainly natural compounds, such as celastrol, curcumin or cyclosporine A, were found to induce paraptosis[16]. In addition, a few synthetic drugs, including some copper complexes[17,19], have been studied. Here, for the first time, we report about paraptosis induction by TSCs. Initiated by the discovery that treatment with nanomolar TSCs, such as Me_2NNMe_2 and Dp44mT, resulted in formation of prominent cytoplasmic vesicles[11], our aim in the here presented study was to investigate whether treatment with Me_2NNMe_2 results in paraptosis or a paraptosis-like cell death. Therefore, we have investigated different pathways and organelles involved in (apoptotic) cell death and paraptosis. Through this approach, we found that indeed Me_2NNMe_2 induced paraptotic cell death fulfilling several main hallmarks such as swelling of ER and mitochondria, caspase independence and MAPK activation (probably via MEK2 signaling).

Interestingly, Raman microscopy experiments revealed an accumulation of Me_2NNMe_2 in the ER-derived vesicles, suggesting that this compound might directly interfere with ER-resident proteins. Subsequent investigations revealed that Me_2NNMe_2 treatment indeed induced a specific form of ER stress. In detail, enhanced nuclear localization of CHOP and PERK phosphorylation were detected. Beside these typical ER stress markers, we additionally observed an upregulation of ero1L-α and PDI, which are both involved in the ER thiol redox homeostasis[34]. Here, especially PDI attracted our attention, as it has been recently described as a copper-binding and -reducing protein[30]. This is of relevance as Me_2NNMe_2 (and other nanomolar TCSs like DpC and Dp44mT) have been well characterized for their metal-chelating properties and especially formation of an intracellular copper metabolite has been suggested to be crucial for their anticancer activity[2,11,12,35,36]. Thus, the PDI-inhibitory potential of Triapine, Me_2NNMe_2 as well as their copper complexes was investigated. Indeed, the copper complexes of Me_2NNMe_2 as well as those of DpC and Dp44mT were able to potently inhibit the enzyme, while the Triapine copper complex as well as the ligands alone were inactive in this assay. Further evidence connecting TSCs to PDI as a potential target can be seen in the overexpression of the PDI family member CaBP1 in a L1210 cell subline selected for resistance to 4-methyl-5-amino-1-formylisoquinoline TSC (MAIQ)[37]. Although this suggests an important role of this protein class in the mode of action of at least some TSCs, no further studies on this topic have been performed so far. Consequently, the exact evaluation of the mechanisms resulting in the PDI inhibition by some copper TSCs is matter of currently ongoing investigations.

In agreement with the PDI inhibition, subsequent analysis showed that Me_2NNMe_2 treatment led to an increase of total glutathione levels, especially of its oxidized form (GSSG) and co-incubation with thiol-containing antioxidants such as NAC or 1-thioglyerol had protective effects. A disrupted thiol redox homeostasis would also explain the enhanced levels of PERK phosphorylation and subsequent CHOP translocation into the nucleus, as seen upon Me_2NNMe_2 treatment[38,39]. CHOP in turn is a transcription factor, which can initiate the observed increased expression of (among others) PDI and ero1L-α[40–42]. In general, disruption of the ER thiol redox homeostasis has already been discussed as the cause of ER stress and dilation for other paraptotic inducers[16,28,43]. To the best of our knowledge, this is the first report connecting the induction of paraptosis to the inhibition of ER-resident proteins. Thus, the role of ER enzyme inhibition definitely needs to be addressed in detail in further studies.

With regard to the paraptotic signaling process, the observed thiol-based ER stress is in good agreement with the mitochondrial changes observed after Me_2NNMe_2 treatment, as it has already been shown that an altered thiol balance leads to Ca^{2+} release from the ER and its uptake by the mitochondria[44,45]. Thus, mitochondria are proposed to function as a buffer system by absorbing released Ca^{2+}[46]. However, prolonged occurrence of

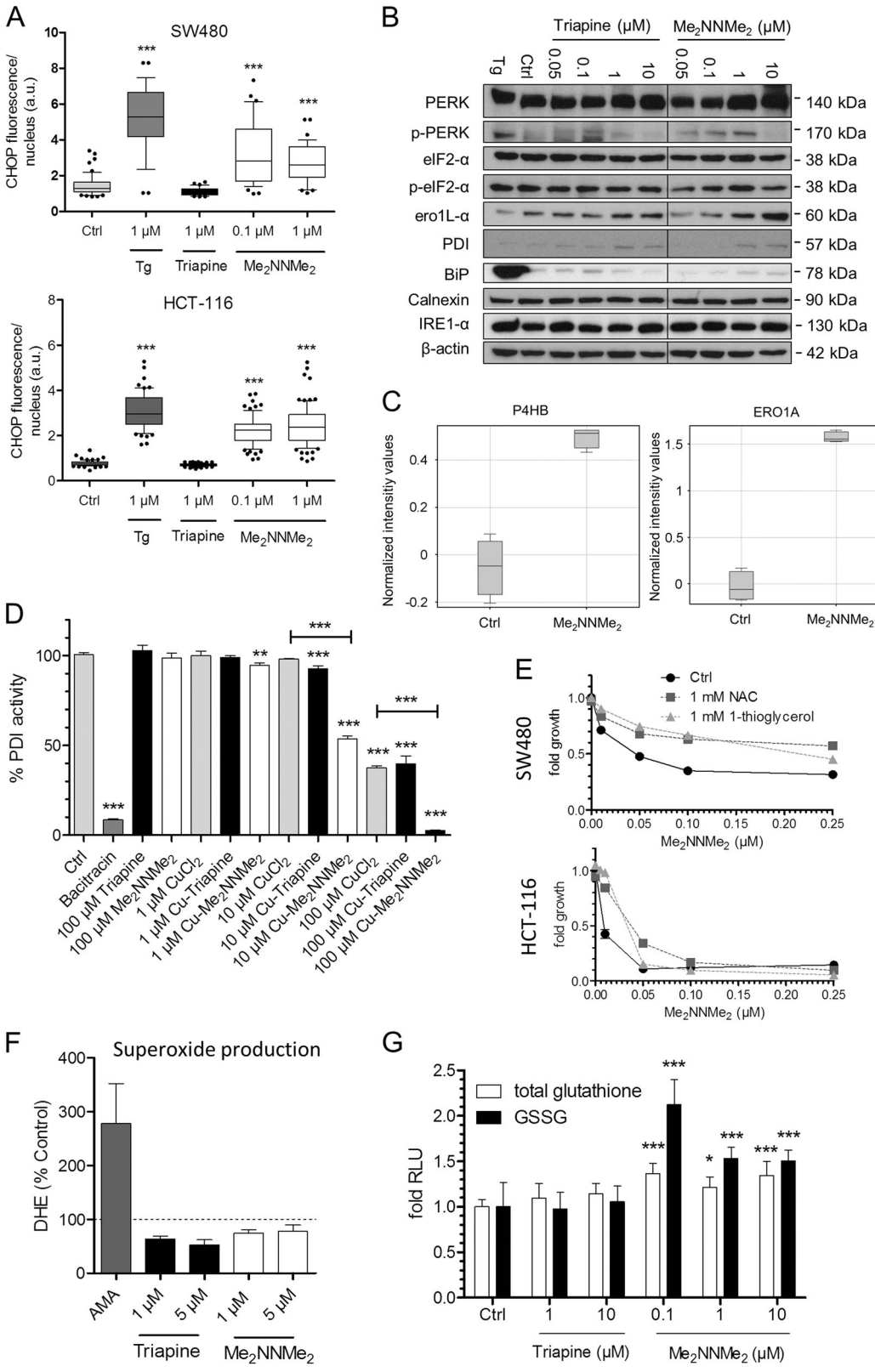

Fig. 7 (See legend on next page.)

(see figure on previous page)

Fig. 7 ER stress and disruption of thiol redox homeostasis by Me_2NNMe_2 treatment. a Quantification of immunofluorescence intensities in the nucleus of the ER stress marker CHOP in SW480 and HCT-116 cells treated with 1 μM thapsigargin (Tg), 1 μM Triapine or 0.1 and 1 μM Me_2NNMe_2 for 24 h. Values given are the mean intensities ± the interquartile range and 10 and 90 percentile whiskers of one representative experiment out of three. **b** Western blot analysis of various ER stress proteins expressed by SW480 cells treated with indicated concentrations of Triapine and Me_2NNMe_2 for 24 h. β-actin was used as a loading control and Tg (1 μM) as positive control for ER stress. **c** mRNA expression levels for PDI (P4HB) and ero1L-α (ERO1A) in treated (1 μM Me_2NNMe_2) or untreated SW480 cells were assessed by whole-genome gene expression microarrays. Two independent P4HB oligonucleotides were spotted on the array and gave comparable results. Data for oligonucleotide A_23_P107412 is shown. Normalized values of four replicates indicate upregulation of PDI and ero1L-α mRNA in treated compared to untreated cells. **d** PDI reduction activity in the presence of Triapine, Me_2NNMe_2 as well as their copper complexes was measured by PROTEOSTAT PDI assay kit. Bacitracin (1 mM) was used as a positive PDI inhibition control. Values given are the mean ± standard deviation of triplicates of one representative experiment out of two. **e** Cell viability measured by MTT assay of SW480 or HCT-116 cells after 72 h treatment of indicated concentrations of Me_2NNMe_2 alone as well as in combination with *N*-acetylcysteine (NAC) or 1-thioglycerol. Values given are the mean ± standard deviation of triplicates of one representative experiment out of three. **f** Superoxide production measured by flow cytometry of DHE fluorescence in HL-60 cells treated with indicated concentrations of Triapine and Me_2NNMe_2 for 45 min. Antimycin A (AMA) was used as positive control. **g** Detection of total and oxidized glutathione (GSSG) by fold increase to control of luminescence in SW480 cells treated with indicated concentrations of Triapine and Me_2NNMe_2 for 24 h. Significance to control (or $CuCl_2$) was calculated with one-way ANOVA and Dunnett's multiple comparison test (***$p < 0.001$, **$p \leq 0.01$, *$p \leq 0.05$)

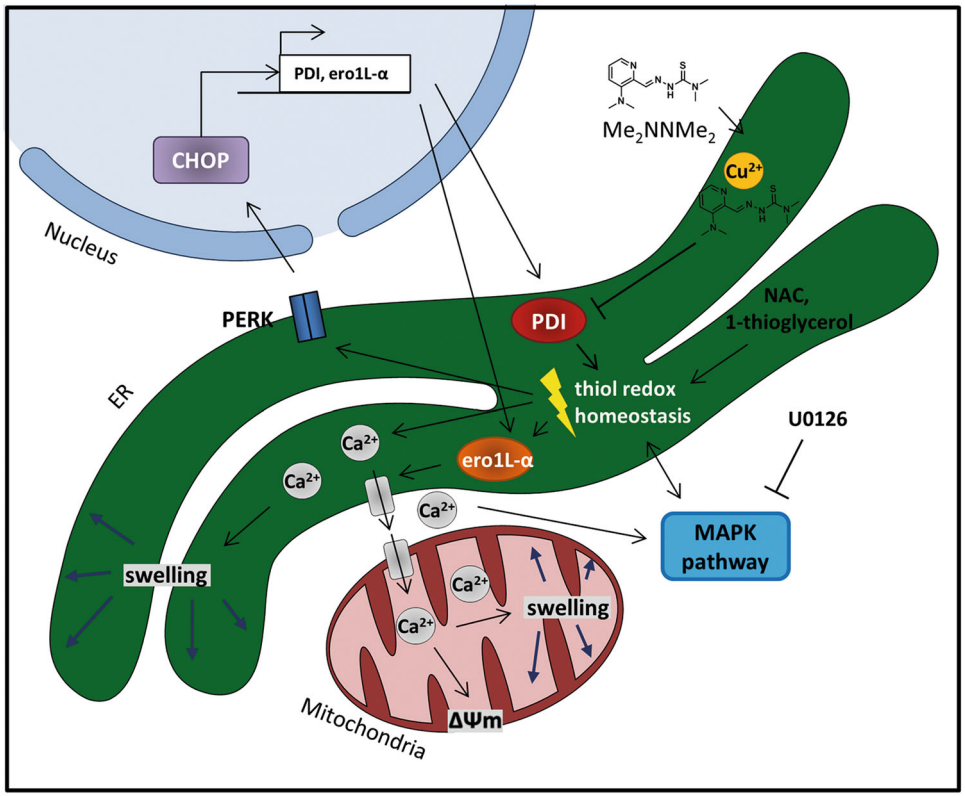

Fig. 8 Proposed mechanism of Me_2NNMe_2-induced paraptosis. Me_2NNMe_2 accumulates in the ER, where it inhibits the reductive potential of PDI. This leads to the disruption of the ER thiol redox homeostasis, which in turn activates PERK signaling and release of Ca^{2+} ions from the ER. While PERK activation is followed by CHOP translocation into the nucleus and increased transcription of PDI and ero1L-α, released Ca^{2+} ions are taken up by mitochondria. Prolonged Ca^{2+} imbalance initiates organelle swelling and mitochondrial membrane depolarization. NAC and 1-thioglycerol can ameliorate thiol redox imbalances. MAPKs further regulate Ca^{2+} and thiol redox homeostasis, which can be inhibited by U0126

enhanced mitochondrial Ca^{2+} levels ultimately results in organelle swelling and damage, which explains the excessive depolarization of mitochondria induced by Me_2NNMe_2 and many other paraptosis inducers[25,27]. Noteworthy, we found that BAX knockout resulted in reduced sensitivity to Me_2NNMe_2. This could be explained by previously observed lowered ER Ca^{2+} stores in BAX-deficient cells, which led to reduced Ca^{2+} uptake

by mitochondria after release from the ER[47]. In addition, also a link between PDI and BAX/BAK signaling has already been reported[48]. Nevertheless, why this mitochondrial damage in the course of paraptosis does not activate the intrinsic (mitochondrial) pathway of apoptosis is still a matter of discussion and warrants further investigations.

Taken together, in the here presented study, we identified paraptosis induction via disruption of the ER thiol redox homeostasis as a new mode of action in the activity of the highly active nanomolar TSC Me_2NNMe_2 and possibly also for other nanomolar TSCs such as DpC, Dp44mT, and Coti-2. Moreover, we suggest the ER-resident PDI as possible new target for members of this compound class, which could make them interesting candidates for the treatment of cancers with deficiencies in apoptosis induction.

Materials and methods

Reagents

Triapine and Me_2NNMe_2 were synthesized as previously described[11,49]. U0126 was purchased from Calbiochem, z-VAD-FMK from Enzo Life Sciences (New York, USA), 1-thioglycerol, thapsigargin, antimycin A, NAC, PD98059, trametinib and selumetinib from Selleck Chemicals (TX, USA). All other chemicals were from Sigma-Aldrich.

Cell culture

The following human cell models were used in this study: the colon carcinoma cell lines SW480 (obtained from the American Tissue Culture Collection) as well as HCT-116 and its respective subline with BAX knockout (obtained from B. Vogelstein, John Hopkins University, Baltimore[18]). SW480 cells were cultured in MEME and HCT-116 cell lines in McCoy's 5a Medium (from Sigma-Aldrich, MO, USA). The cells were cultivated in medium containing 10% fetal calf serum (FCS, PAA, Linz, Austria).

Transfection

SW480 cells were plated (3×10^5 cells/well) in 6-well plates and allowed to recover for 24 h. Transfection of pEYFP-ER expression plasmid (#632355, Clontech laboratories, USA) encoding a YFP fused to the ER-targeting sequence of calreticulin at the 5′-end and the ER retention sequence KDEL at the 3′-end or with a control plasmid was performed using Lipofectamine 2000 reagent (Invitrogen, CA, USA) according to the manufacturers' instructions. Medium was changed after 5 h and selection medium containing 1.2 mg/ml G418 was added 24 h after transfection. Expression of YFP in the ER was investigated 48 h later.

Cell viability assay

The cells were plated (2×10^3 cells/well) in 96-well plates and allowed to recover for 24 h. Then, cells were treated with Triapine or Me_2NNMe_2. In combination treatments, the modulator was always added 1 h in advance. Cell viability was measured by the 3-(4,5-dimethylthiazol-2-yl)-2,5-diphenyltetrazolium bromide (MTT)-based vitality assay (EZ4U; Biomedica, Vienna, Austria) as published[50]. GraphPad Prism software was used to calculate cell viability expressed as IC_{50} values calculated from full dose-response curves.

Fluorescence staining and microscopy

Cells were seeded into 8-well µ-slides (ibidi GmbH, Germany) with 2×10^4 cells/well and left to recover for 24 h. For organelle tracking, the medium was replaced with serum- and phenol red-free medium with 50 nM MitoTracker Red CMXRos, MitoTracker Green FM or LysoTracker Red (Life technologies, Vienna, Austria). For calcium imaging, cells were incubated with 0.5 µM Rhod-2 AM (Abcam, Cambridge, UK) in serum- and phenol red-free medium for 30 min at 4 °C. After 1 h, cells were washed and imaged with the Nikon Eclipse Ti-e fluorescence microscope with differential interference contrast and RFP or GFP filter settings and a sCMOS pco.edge camera. Life-cell imaging was performed in an environmental chamber pre-heated to 37 °C with 5% CO_2. For non-fluorescence imaging, phase-contrast pictures were taken with the Nikon Eclipse Ti inverted microscope with a Nikon DS-Fi1c camera. Contrast and brightness were adjusted with ImageJ. Cell area was calculated as mean occupied area per cell from at least two different sections in one well at the end of life-cell imaging (48 h) using ImageJ and then normalized to control.

CHOP immunofluorescence

Cells (2×10^4/well) were seeded in 8-well chamber slides (ibidi GmbH). After 24 h recovery, cells were treated with indicated drug concentrations and fixed with 4% paraformaldehyde for 15 min at room temperature and (after washing with PBS) blocked and permeabilized with 5% FCS, 0.3% Triton X-100 in PBS for 1 h. The primary antibody CHOP (Cell Signaling Technology) was added 1:3200 in 1% BSA and 0.3% Triton X-100 in PBS overnight at 4 °C. After washing with PBS, the cells were incubated with anti-mouse secondary antibody conjugated to AlexaFluor488 (Thermo Fisher, 1:500 in 1% BSA and 0.3% Triton X-100 in PBS) for 1 h. Cells were again washed and counterstained with 4′,6-diamidine-2′-phenylindole dihydrochloride (DAPI; 1 µg/ml) and wheat germ agglutinin (WGA, 10 µg/ml, Vector Laboratories,

CA, USA) in PBS for 10 min. The dyes were removed, and the cells mounted in Vectashield mounting medium (Vector Laboratories, CA, USA) with a coverslip. Images were taken with a Zeiss LSM 700 Olympus (Carl Zeiss AG, Oberkochen, Germany) confocal microscope and CHOP fluorescence intensities per nucleus were measured using ImageJ.

Annexin V/PI stain and detection of mitochondrial membrane potential

Briefly, 2×10^5 cells/well were seeded in 6-well plates. After 24 h recovery, cells were treated for another 24 h with the indicated drug concentrations. Then, cells were either stained with annexin V-APC (AV) and propidium iodide (PI) or with 10 µg/ml JC-1 as previously described[51,52].

Protein expression

After drug treatment, total protein lysates were prepared, separated by SDS-PAGE and transferred onto a polyvinylidene difluoride membrane for Western blotting as described previously[50]. The following antibodies were used: Cell Signaling Technology (MA, USA): BAX (#5023), Bcl-x_L (#2764), PERK (#5683), phospho-PERK (Thr980, #3179), Calnexin (#2679), eIF2-α (#5324), phospho-eIF2-α (Ser51, #3398), PDI (#3501), ero1L-α (#3264), BiP (#3177), IRE1α (#3294), MEK1/2 (#9126), phospho-MEK1/2 (Ser217/221, #9154), MEK2 (#9125) ERK1/2 (#4695), phospho-ERK1/2 (Thr202/Tyr204, #4370). Sigma-Aldrich: β-actin (AC-15; #A1978). Primary antibodies were used 1:1000. Secondary, anti-mouse (#7076) and anti-rabbit (#7074) horseradish peroxidase-labeled antibodies from Cell Signaling Technologies were used in working dilutions of 1:10,000.

Gene knockdown by siRNA

Cells were transfected with Xfect™ RNA Transfection Reagent (Clontech Laboratories, CA, USA) using siRNA against MEK2 (Dharmacon, #M-003573-03-0005) or non-targeting siRNA (Dharmacon, #D-001206-13-05) following the manufacturer's recommendations. Briefly, 3×10^5 SW480 cells/well or 4×10^5 HCT-116 cells/well were seeded in 6-well plates. After 24 h cells were incubated with the siRNAs and transfection polymer in serum-free medium for 4 h. Then, the medium was exchanged and after another 24 or 48 h cells were collected for experiments. Efficacy and specificity of gene silencing was verified at the protein level by Western blot following 48 h siRNA transfection.

Total-RNA isolation and whole-genome gene expression array

Total RNA from SW480 cells (either untreated or treated for 15 h) was isolated using RNeasy Mini kit (Quiagen) following the manufacturer's instruction. Transcriptional profiles of cells were determined performing a 4 × 44 K whole-genome oligonucleotide gene expression array (Agilent) as described previously[53]. Normalization was performed in R using the Bioconductor (version 3.7) package "limma"[54]. Whole-genome gene expression array and gene set enrichment analysis (GSEA) were performed as previously described[51]. Visualization of differentially expressed genes in the KEGG database-derived "MAPK signaling pathway" was conducted using the Bioconductor package "pathview"[55].

Raman microspectroscopy

Cells (2×10^4 /well) were seeded into 8-well µ-slides with glass-bottom (ibidi GmbH, Germany) and left to recover for 24 h followed by 24 h drug treatment. Subsequently, samples were fixed with 2% formaldehyde in PBS for 5 min. Cells were mapped in PBS using an XploRA INV Raman microscope (Horiba Jobin Yvon, Bensheim, Germany) equipped with a 532 nm solid state laser at 100 mW, 1800 gr/mm grating and CFI Plan APO ×100 NA 1.4 Oil objective (Nikon). Two spectra per pixel were acquired with an integration time of two seconds in steps of 0.5 µm in X and Y. Cosmic rays were removed automatically. The spectral fingerprint region of 600–1800 cm^{-1} was extracted from raw spectra, the 1st derivative (size = 5, degree = 1) was calculated and unit vector normalization was performed. Principal component analysis (PCA) with three components was computed and displayed as a spectral map. Component spectra were shifted on the intensity scale for better visualization. The spectrum of Me_2NNMe_2 powder was acquired using the 532 nm laser at 100 mW, 2400 gr/mm grating, CFI Apo Lambda S ×40 NA 1.15 Water objective (Nikon) with 4 × 5 s integration and processed as described above. The processed spectrum of Me_2NNMe_2 was fitted to the spectral map of the cells by using the CLS function. All calculation and visualization steps were performed in LabSpec 6 (Horiba, Jobin Yvon, Bensheim, Germany).

PDI reduction activity measurement

PDI reduction activity was measured using PROTEOSTAT PDI assay kit (#ENZ-51024, Enzo Life Sciences, Lausen, Switzerland). Experiments were performed according to the manufacturer's instructions. Briefly, drugs alone or preincubated with $CuCl_2$ (1:1) were added to a prepared insulin PDI solution. Then, DTT was added to start PDI reduction activity. After 30 min the reaction was stopped by the Stop reagent and the insulin precipitate was fluorescently labeled with Proteostat PDI detection reagent for 15 min. Fluorescence intensity was measured at 500 nm excitation and 603 nm emission

using the spectrophotometer Tecan infinite 200Pro (Tecan Group, Männedorf, Switzerland).

Glutathione measurement

Cells were plated (4×10^3 cells/well) in 96-well plates and allowed to recover for 24 h. Then, cells were treated in sextuplicates with Triapine or Me_2NNMe_2 for another 24 h. Cells were lysed and levels of total and oxidized glutathione were measured in triplicates with GSH/GSSG-Glo™ Assay (#V6611, Promega, Madison, USA) according to the manufacturer's instructions. Fold increase in relative luminescence units (RLU) was calculated compared to untreated control after subtraction of cell-free blank.

Detection of intracellular superoxide

Dihydroethidium (DHE, #D7008, Sigma-Aldrich, MO, USA) was used to detect the production of intracellular superoxide. Briefly, 5×10^5 HL-60 cells per sample in 500 µl of PBS (78.1 mM $Na_2PO_4 \times 2\ H_2O$, 14.7 mM KH_2PO_4, 26.8 mM KCl, 1.37 M NaCl) were incubated with indicated concentrations of Triapine and Me_2NNMe_2 for 45 min. Subsequently, DHE (10 µM) was added 15 min after the compounds. After incubation, the mean fluorescence intensity was measured by flow cytometry using a FACSCalibur instrument (Becton Dickinson, Palo Alto, CA, USA). Antimycin A (AMA, 10 µM) was used as positive control.

Acknowledgements

This work was performed within the Research Cluster "Translational Cancer Therapy Research" Vienna. This work was in part funded by the Austrian Science Fund (FWF) grant number P22072 (to Walter Berger), number P31923 (to Christian R. Kowol) and number P26603 (to Petra Heffeter). The funding sources had no involvement in collection, analysis and interpretation of data as well as in the decision to submit the article for publication. S.H. is a recipient of a DOC Fellowship of the Austrian Academy of Sciences. We are indebted to Sushilla van Schoonhoven and Mirjana Stojanovic for competent technical assistance. Furthermore, we are grateful to Irene Herbacek for fluorescence-activated cell sorting analysis and Gerald Timelthaler for the assistance in confocal microscopy. We thank the BOKU-VIBT Imaging Center for technical support with Raman microspectroscopy.

Author details

[1]Institute of Cancer Research and Comprehensive Cancer Center, Department of Medicine I, Medical University of Vienna, Borschkegasse 8a, A-1090 Vienna, Austria. [2]Research Cluster "Translational Cancer Therapy Research", Vienna, Austria. [3]Institute of Inorganic Chemistry, Faculty of Chemistry, University of Vienna, Waehringer Str. 42, A-1090 Vienna, Austria. [4]Department of Biotechnology, BOKU-University of Natural Resources and Life Sciences, ViennaMuthgasse 18, A-1190 Vienna, Austria. [5]Christian Doppler Laboratory on Biotechnology of Skin Aging, Muthgasse 18, A-1190 Vienna, Austria. [6]Evercyte GmbH, Muthgasse 18, A-1190 Vienna, Austria. [7]Department of Internal Medicine I and Comprehensive Cancer Center, Medical University of Vienna, Lazarettgasse 14, A-1090 Vienna, Austria. [8]Department of Physiology, Faculty of Medicine, Semmelweis University, Tűzoltó utca 37-47, H-1094 Budapest, Hungary. [9]Institute of Enzymology, Research Centre for Natural Sciences, Hungarian Academy of Sciences, Magyar Tudósok körútja 2, H-1117 Budapest, Hungary. [10]Science Consult DI Thomas Mohr KG, Enzianweg 10a, A-2353 Guntramsdorf, Austria

Conflict of interest

The authors declare that they have no conflict of interest.

Publisher's note

Springer Nature remains neutral with regard to jurisdictional claims in published maps and institutional affiliations.

Supplementary Information accompanies this paper at (https://doi.org/10.1038/s41419-018-1102-z).

Received: 13 August 2018 Revised: 4 September 2018 Accepted: 21 September 2018
Published online: 15 October 2018

References

1. Kalinowski, D. S., Quach, P. & Richardson, D. R. Thiosemicarbazones: the new wave in cancer treatment. *Future Med. Chem.* **1**, 1143–1151 (2009).
2. Heffeter, P. et al. Anticancer thiosemicarbazones: chemical properties, interaction with iron metabolism, and resistance development. *Antioxid. Redox Signal.* https://doi.org/10.1089/ars.2017.7487 (2018).
3. Giles, F. J. et al. Phase I and pharmacodynamic study of Triapine, a novel ribonucleotide reductase inhibitor, in patients with advanced leukemia. *Leuk. Res.* **27**, 1077–1083 (2003).
4. Karp, J. E. et al. A phase I study of the novel ribonucleotide reductase inhibitor 3-aminopyridine-2-carboxaldehyde thiosemicarbazone (3-AP, Triapine) in combination with the nucleoside analog fludarabine for patients with refractory acute leukemias and aggressive myeloproliferative disorders. *Leuk. Res.* **32**, 71–77 (2008).
5. Yee, K. W. et al. Triapine and cytarabine is an active combination in patients with acute leukemia or myelodysplastic syndrome. *Leuk. Res.* **30**, 813–822 (2006).
6. Zeidner, J. F. et al. A phase II trial of sequential ribonucleotide reductase inhibition in aggressive myeloproliferative neoplasms. *Haematologica* **99**, 672–678 (2014).
7. Attia, S. et al. A phase 2 consortium (P2C) trial of 3-aminopyridine-2-carboxaldehyde thiosemicarbazone (3-AP) for advanced adenocarcinoma of the pancreas. *Invest. New Drugs* **26**, 369–379 (2008).
8. Knox, J. J. et al. Phase II study of Triapine in patients with metastatic renal cell carcinoma: a trial of the National Cancer Institute of Canada Clinical Trials Group (NCIC IND.161). *Invest. New Drugs* **25**, 471–477 (2007).
9. Jansson, P. J., Sharpe, P. C., Bernhardt, P. V. & Richardson, D. R. Novel thiosemicarbazones of the ApT and DpT series and their copper complexes: identification of pronounced redox activity and characterization of their antitumor activity. *J. Med. Chem.* **53**, 5759–5769 (2010).
10. Maleki Vareki, S., Salim, K. Y., Danter, W. R. & Koropatnick, J. Novel anti-cancer drug COTI-2 synergizes with therapeutic agents and does not induce resistance or exhibit cross-resistance in human cancer cell lines. *PLoS ONE* **13**, e0191766 (2018).
11. Kowol, C. R. et al. Impact of stepwise NH2-methylation of triapine on the physicochemical properties, anticancer activity, and resistance circumvention. *J. Med. Chem.* **59**, 6739–6752 (2016).
12. Ishiguro, K. et al. Distinct mechanisms of cell-kill by triapine and its terminally dimethylated derivative Dp44mT due to a loss or gain of activity of their copper(II) complexes. *Biochem. Pharmacol.* **91**, 312–322 (2014).
13. Lovejoy, D. B. et al. Antitumor activity of metal-chelating compound Dp44mT is mediated by formation of a redox-active copper complex that accumulates in lysosomes. *Cancer Res.* **71**, 5871–5880 (2011).
14. Seebacher, N. A., Richardson, D. R. & Jansson, P. J. A mechanism for overcoming P-glycoprotein-mediated drug resistance: novel combination therapy that releases stored doxorubicin from lysosomes via lysosomal permeabilization using Dp44mT or DpC. *Cell Death Dis.* **7**, e2510 (2016).
15. Sperandio, S., de Belle, I. & Bredesen, D. E. An alternative, nonapoptotic form of programmed cell death. *Proc. Natl Acad. Sci. USA* **97**, 14376–14381 (2000).
16. Lee, D., Kim, I. Y., Saha, S. & Choi, K. S. Paraptosis in the anti-cancer arsenal of natural products. *Pharmacol. Ther.* **162**, 120–133 (2016).

17. Gandin, V. et al. Therapeutic potential of the phosphino Cu(I) complex (HydroCuP) in the treatment of solid tumors. *Sci. Rep.* **7**, 13936 (2017).
18. Chen, X. et al. Hinokitiol copper complex inhibits proteasomal deubiquitination and induces paraptosis-like cell death in human cancer cells. *Eur. J. Pharmacol.* **815**, 147–155 (2017).
19. Tardito, S. et al. The thioxotriazole copper(II) complex A0 induces endoplasmic reticulum stress and paraptotic death in human cancer cells. *J. Biol. Chem.* **284**, 24306–24319 (2009).
20. Movasaghi, Z., Rehman, S. & Rehman, I. U. Raman spectroscopy of biological tissues. *Appl. Spectrosc. Rev.* **42**, 493–541 (2007).
21. Xue, J. et al. Morusin induces paraptosis-like cell death through mitochondrial calcium overload and dysfunction in epithelial ovarian cancer. *Chem. Biol. Interact.* **283**, 59–74 (2018).
22. Yoon, M. J. et al. Release of Ca2+ from the endoplasmic reticulum and its subsequent influx into mitochondria trigger celastrol-induced paraptosis in cancer cells. *Oncotarget* **5**, 6816–6831 (2014).
23. Bury, M. et al. Ophiobolin A induces paraptosis-like cell death in human glioblastoma cells by decreasing BKCa channel activity. *Cell Death Dis.* **4**, e561 (2013).
24. Heath-Engel, H. M., Wang, B. & Shore, G. C. Bcl2 at the endoplasmic reticulum protects against a Bax/Bak-independent paraptosis-like cell death pathway initiated via p20Bap31. *Biochim. Biophys. Acta* **1823**, 335–347 (2012).
25. Yoon, M. J. et al. Stronger proteasomal inhibition and higher CHOP induction are responsible for more effective induction of paraptosis by dimethoxycurcumin than curcumin. *Cell Death Dis.* **5**, e1112 (2014).
26. He, L. et al. Cyclometalated iridium(iii) complexes induce mitochondria-derived paraptotic cell death and inhibit tumor growth in vivo. *Dalton Trans.* https://doi.org/10.1039/c8dt00783g (2018).
27. Garrido-Armas, M. et al. Paraptosis in human glioblastoma cell line induced by curcumin. *Toxicol. In Vitro* https://doi.org/10.1016/j.tiv.2018.04.014 (2018).
28. Kim, I. Y. et al. Ophiobolin A kills human glioblastoma cells by inducing endoplasmic reticulum stress via disruption of thiol proteostasis. *Oncotarget* **8**, 106740–106752 (2017).
29. Nedungadi, D. et al. 6-Shogaol induces caspase-independent paraptosis in cancer cells via proteasomal inhibition. *Exp. Cell Res.* **364**, 243–251 (2018).
30. Narindrasorasak, S., Yao, P. & Sarkar, B. Protein disulfide isomerase, a multifunctional protein chaperone, shows copper-binding activity. *Biochem. Biophys. Res. Commun.* **311**, 405–414 (2003).
31. Laurindo, F. R., Pescatore, L. A. & Fernandes Dde, C. Protein disulfide isomerase in redox cell signaling and homeostasis. *Free Radic. Biol. Med.* **52**, 1954–1969 (2012).
32. Housman, G. et al. Drug resistance in cancer: an overview. *Cancers* **6**, 1769–1792 (2014).
33. Wang, L., Gundelach, J. H. & Bram, R. J. Cycloheximide promotes paraptosis induced by inhibition of cyclophilins in glioblastoma multiforme. *Cell Death Dis.* **8**, e2807 (2017).
34. Li, G. et al. Role of ERO1-alpha-mediated stimulation of inositol 1,4,5-triphosphate receptor activity in endoplasmic reticulum stress-induced apoptosis. *J. Cell Biol.* **186**, 783–792 (2009).
35. Kalinowski, D. S. et al. Redox cycling metals: pedaling their roles in metabolism and their use in the development of novel therapeutics. *Biochim. Biophys. Acta* **1863**, 727–748 (2016).
36. Lane, D. J. et al. Expanding horizons in iron chelation and the treatment of cancer: role of iron in the regulation of ER stress and the epithelial-mesenchymal transition. *Biochim. Biophys. Acta* **1845**, 166–181 (2014).
37. Crenshaw, T. R. & Cory, J. G. Overexpression of protein disulfide isomerase-like protein in a mouse leukemia L1210 cell line selected for resistance to 4-methyl-5-amino-1-formylisoquinoline thiosemicarbazone, a ribonucleotide reductase inhibitor. *Adv. Enzym. Regul.* **42**, 143–157 (2002).
38. Kranz, P. et al. PDI is an essential redox-sensitive activator of PERK during the unfolded protein response (UPR). *Cell Death Dis.* **8**, e2986 (2017).
39. Darling, N. J. & Cook, S. J. The role of MAPK signalling pathways in the response to endoplasmic reticulum stress. *Biochim. Biophys. Acta* **1843**, 2150–2163 (2014).
40. Li, Y., Guo, Y., Tang, J., Jiang, J. & Chen, Z. New insights into the roles of CHOP-induced apoptosis in ERstress. *Acta Biochim. Biophys. Sin.* **46**, 629–640 (2014).
41. Marciniak, S. J. et al. CHOP induces death by promoting protein synthesis and oxidation in the stressed endoplasmic reticulum. *Genes Dev.* **18**, 3066–3077 (2004).
42. Ubeda, M. & Habener, J. F. CHOP gene expression in response to endoplasmic-reticular stress requires NFY interaction with different domains of a conserved DNA-binding element. *Nucleic Acids Res.* **28**, 4987–4997 (2000).
43. Singha, P. K., Pandeswara, S., Venkatachalam, M. A. & Saikumar, P. Manumycin A inhibits triple-negative breast cancer growth through LC3-mediated cytoplasmic vacuolation death. *Cell Death Dis.* **4**, e457 (2013).
44. Tadic, V., Prell, T., Lautenschlaeger, J. & Grosskreutz, J. The ER mitochondria calcium cycle and ER stress response as therapeutic targets in amyotrophic lateral sclerosis. *Front. Cell. Neurosci.* **8**, 147 (2014).
45. Bhandary, B., Marahatta, A., Kim, H. R. & Chae, H. J. An involvement of oxidative stress in endoplasmic reticulum stress and its associated diseases. *Int. J. Mol. Sci.* **14**, 434–456 (2012).
46. Hacker, K. & Medler, K. F. Mitochondrial calcium buffering contributes to the maintenance of Basal calcium levels in mouse taste cells. *J. Neurophysiol.* **100**, 2177–2191 (2008).
47. Scorrano, L. et al. BAX and BAK regulation of endoplasmic reticulum Ca2+: a control point for apoptosis. *Science* **300**, 135–139 (2003).
48. Hoffstrom, B. G. et al. Inhibitors of protein disulfide isomerase suppress apoptosis induced by misfolded proteins. *Nat. Chem. Biol.* **6**, 900–906 (2010).
49. Kowol, C. R. et al. Impact of metal coordination on cytotoxicity of 3-aminopyridine-2-carboxaldehyde thiosemicarbazone (triapine) and novel insights into terminal dimethylation. *J. Med. Chem.* **52**, 5032–5043 (2009).
50. Heffeter, P. et al. Intrinsic and acquired forms of resistance against the anticancer ruthenium compound KP1019 [indazolium trans-[tetrachlorobis(1H-indazole)ruthenate (III)] (FFC14A). *J. Pharmacol. Exp. Ther.* **312**, 281–289 (2005).
51. Englinger, B. et al. Loss of CUL4A expression is underlying cisplatin hypersensitivity in colorectal carcinoma cells with acquired trabectedin resistance. *Br. J. Cancer* **116**, 489–500 (2017).
52. Trondl, R. et al. Triapine and a more potent dimethyl derivative induce endoplasmic reticulum stress in cancer cells. *Mol. Pharmacol.* **85**, 451–459 (2014).
53. Laszlo, V. et al. Epigenetic down-regulation of integrin alpha7 increases migratory potential and confers poor prognosis in malignant pleural mesothelioma. *J. Pathol.* **237**, 203–214 (2015).
54. Ritchie, M. E. et al. limma powers differential expression analyses for RNA-sequencing and microarray studies. *Nucleic Acids Res.* **43**, e47 (2015).
55. Luo, W. & Brouwer, C. Pathview: an R/Bioconductor package for pathway-based data integration and visualization. *Bioinformatics* **29**, 1830–1831 (2013).